CRANFIELD UNIVERSITY

Filomeno Martina

Investigation of methods to manipulate geometry, microstructure and mechanical properties in titanium large scale Wire+Arc Additive Manufacturing

School of Aerospace, Transport and Manufacturing

PhD Thesis
Academic year 2013–2014

Supervisors
Prof. Stewart Williams
Dr. Paul Colegrove

CRANFIELD UNIVERSITY

School of Aerospace, Transport and Manufacturing
PhD Thesis
Academic year 2013–2014

Filomeno Martina

Investigation of methods to manipulate geometry, microstructure and mechanical properties in titanium large scale Wire+Arc Additive Manufacturing

Supervisors
Prof. Stewart Williams
Dr. Paul Colegrove

This thesis is submitted in partial fulfilment of the requirements for the degree of Doctor of Philosophy.

Abstract

Wire+arc additive manufacturing is a technique suitable for the deposition of large components; a variety of materials can be processed, including titanium.

For the alloy Ti–6Al–4V, an experimental model based on design of experiment and linear regression was developed to control layer geometry during deposition. The modelled variables were wall width and layer height; the former was dependent on the heat input, and the latter on the heat input as well as on the wire feed speed to travel speed ratio. Equations enabled the automatic selection of process parameters based on geometric requirements specific to the part being built. This could ensure minimisation of production time and material waste.

Additively manufactured parts are affected by distortion and residual stress; the effect of high pressure rolling on these two, as well as on geometry, microstructure and mechanical properties was studied. Due to plastic deformation, rolled linear deposits were characterised by a larger width and smaller height. The variability of the layer height was reduced, a beneficial effect from a production implementation viewpoint.

Distortion was less than half in rolled components, a change associated with the reduction in residual stress which were still tensile in the bottom of the parts and compressive in their top; however their overall magnitude was smaller than in the unrolled samples. The contour method showed relatively good agreement with the neutron diffraction measurements, and although destructive it proved to be a fast way to characterise residual stress in additively manufactured components.

Microstructurally, the columnar prior β grains configuration observed in all unrolled deposits, also affected by a strong texture developed in the building direction, was changed to equiaxed grains due to the recrystallisation triggered by both the strain introduced by rolling and the repeated thermal cycles induced by each layer deposition. The microstructure was overall considerably finer and the texture randomised. A fundamental study was performed to discern the extent of the deformed zone from the one affected thermally. While the deformed zone could not be identified precisely, the thermally influenced zone showed a relationship between rolling load and depth of the recrystallised volume.

Finally, testing of hardness and tensile strength showed superior properties of rolled specimens than in the unrolled specimens. The mechanical performance of rolled samples was fully isotropic too.

This project was entirely sponsored by Airbus Group Innovations (formerly EADS Innovation Works).

Acknowledgments

"The first responsibility of a leader is to define reality. The last is to say thank you. In between, the leader is a servant."
Max de Pree

First and foremost I would like to express my enormous gratitude to my wonderful family. Without your support I would be nowhere near to where I am now, from both the professional and the personal point of view. Your constant and unconditional presence hasn't been important just for the mere financial aspect, which is fundamental nonetheless, but especially for all your life examples, on a daily basis. My dad is the bestest dad and my biggest hero, and my mum the ideal woman. I would be honoured to be even half as great parents as you have been. I should have thanked you much more than I ever have. Your long-term view has proven to be crucial. It must have been hard to accept the idea I was going to leave home, when everything suggested I was going to spend the rest of my life around there. Nevertheless you were happier and more proud than I have ever been, and I live every day of my life trying to make you even happier and prouder, to pay back you for all you have given me. My little (not so little anymore) sister, you are a star and I wish you all the best for your life.

Prof Stewart Williams and Dr Paul Colegrove have been the best supervisors I could have wished for. Stewart, you have been great in setting the broad aims and objectives for my research, and I've received much inspiration and advice from the heights of your immense experience, and from you leading by example. Paul, your contribution on a daily basis has been priceless and I sometimes wonder how you did not get annoyed with me and with all the little informal meetings I have put you through, as well as the thousands lines of text you have had to review throughout this project!

Everyone at the Welding Engineering and Laser Processing Centre has been equally important for the positive outcome of this research work. I have on so many occasions praised the perfect working environment we are lucky to have, something rather rare, which everyone appreciates and cherishes. It has been the best place to work, and my friends Sonia, Jialuo, Supriyo, Wojciech, Usani, Goncalo, Wasiu, Anthony, Jibrin, Sergio, Yash, Gu, Adrian, Daniel, Harry, Fude, Pedro, Wang, Craig, Stephen, Ibrahim, Eurico, Matthew, Tamas and Matyas you are those who have made it possible.

The support of Brian Brooks and Flemming Nielsen has been just unbelievable. As much as I deeply respect your jobs, I would never dream of being in your shoes, having to keep up with the pressing requests of us research students with only four hands and a very limited amount of time. Without your presence, no one of us would have been able to be where we are now. We all owe you. The help of Andrew Dyer and Xianwei Liu is also acknowledged.

My sponsor Airbus Group Innovations (formerly EADS Innovation Works), and specifically Dr Jonathan Meyer and Andrew Henstridge, made my research possible thanks to their financial support, they are true believers in the future and potential of additive manufacturing and they invested in my project when other companies

hadn't even heard about this technology at all.

Special thanks to Laetitia, who, amongst many other great and indescribable qualities, had the burden of being next to me during the challenging, hard, long months of the preparation towards my first IronMan. No words can describe what it meant to me. I owe you more apologies than acknowledgements.

A big thank to all the friends I have and I've made here in the UK: Luca, Carmine, Francesco, Wev (and his parents Jan and Barry), Peršo, Mo, Ali, Satnam, Gaz, Liam, Dan, Vas $\times$ 2, Shane and all the rest of the Kempston lot. I came knowing literally no one, and you all made me feel like at home! All the endless nights we have spent cooking, talking, clubbing or chilling have been the perfect mean to release the pressure of my daily activities.

I cannot forget the distant but fundamental support of all my life-long friends back in Italy. It is amazing how you don't need to be necessarily in touch with your real friends, to feel connected to them. Every time I speak or write to one of you, it is just like the last time we spoke to each one other was the day before.

Simon, you have been the ideal partner to throw all my moaning upon, during our long rides. Thanks for keeping up with me. I thought your turn to moan would have come, but the truth is you never do! Wait until your kid becomes a teenager.

Bruno, my remote coach, has had the duty not only to train a stubborn, enquiring engineer that is constantly questioning every single piece of information he receives, but also to withstand my moaning and barking, which were frequently unrelated to the most urgent topic of our conversation, the sport. I often wonder what you really think of me.

Moreover, I would like to thank Steven Wilson, Gavin Harrison, Richard Barbieri, Colin Edwin, John Wesley, Danny Carey, Adam Jones, Maynard James Keenan and Justin Chancellor. Your support and company have covered so many different moments of my day, whether it was work, or training, or resting, or thinking. Your talents and achievements are a true inspiration.

Finally, thanks to everyone who will read this piece of work. I hope you enjoy it and find it useful.

Declaration

A large part of the work described in this thesis is based on articles which have been, or are intended to be, published elsewhere. For each of them, the candidate (F. Martina) contributed principally to all aspects of the work described therein:

Martina, F., Menhen, J., Williams, S.W., Colegrove, P.A., Wang, F. 2012. Investigation of the benefits of plasma deposition for the additive layer manufacture of Ti–6Al–4V. Journal of Materials Processing Tech. 212, 1377–1386.

Martina, F., Williams, S., Colegrove, P.A., 2013. Design of an empirical process model and algorithm for the tungsten inert gas wire+arc additive manufacture of Ti–6Al–4V components, in: 24th International Solid Freeform Fabrication Symposium, Austin, Texas, USA. pp. 697–707.

Martina, F., Williams, S., Colegrove, P.A., 2013. Improved microstructure and increased mechanical properties of additive manufacture produced Ti–6Al–4V by interpass cold rolling, in: 24th International Solid Freeform Fabrication Symposium, Austin, Texas, USA. pp. 490–496.

Martina, F., Roy, M.J., Colegrove, P.A., Williams, S.W., 2014. Residual stress reduction in high pressure interpass rolled Wire+Arc Additive Manufacture Ti-6Al-4V components, in: 25th International Solid Freeform Fabrication Symposium, Austin, Texas, USA. pp. 89–94.

Martina, F., 2013. Additive manufacturing: current status and future developments. Submitted to Royal Aeronautical Society. Available on line.

Martina, F., Colegrove, P.A., Williams, S.W., Meyer, J., 2014a. Microstructure of interpass rolled Wire + Arc Additive Manufacturing Ti–6Al–4V components. Journal of Materials Processing Tech. (submitted).

Martina, F., Colegrove, P.A., Williams, S.W., Meyer, J., 2014b. Tensile strength, elongation and microhardness of as-deposited and interpass rolled Wire + Arc Additive Manufacturing Ti–6Al–4V components. Journal of Materials Processing Tech. (submitted).

Martina, F., Roy, M.J., Colegrove, P.A., Williams, S.W., Withers, P.J., Meyer, J., 2014c. Residual stress of as-deposited and interpass rolled Wire + Arc Additive

Manufacturing Ti–6Al–4V components. Journal of Materials Processing Tech. (submitted).

Furthermore, while the work described in chapters 3, 4, and 5 is the candidate's own, some of the results presented in these chapters have also been included in the following articles:

Colegrove, P.A., Coules, H.E., Fairman, J., Martina, F., Kashoob, T., Mamash, H., Cozzolino, L.D., 2013. Microstructure and residual stress improvement in wire and arc additively manufactured parts through high-pressure rolling. Journal of Materials Processing Tech. 213, 1782–1791.

Colegrove, P.A., Martina, F., Roy, M.J., Szost, B., Terzi, S., Williams, S.W., Withers, P.J., Jarvis, D., 2014. High pressure interpass rolling of Wire + Arc Additively Manufactured titanium components. Advanced Materials Research 996, 694–700.

Antonysamy, A., Martina, F., Colegrove, P.A., Williams, S., Prangnell, P., 2013. The effect of integrating rolling deformation with wire arc additive manufacture of Ti–6Al–4V on grain size and texture refinement. Metallurgical and Materials Transactions A (submitted).

Ding, J., Colegrove, P.A., Martina, F., Williams, S.W., Wiktorowicz, R., Palt, M., 2014. Development of a laminar flow local shielding device for Wire + Arc Additive Manufacture. Journal of Materials Processing Tech. (submitted).

This thesis is submitted on the conditions contained in the Regulations, and has not been submitted for any other academic or professional award. All of the work described was carried out as part of the course of study at Cranfield University and not previously or subsequently.

Candidate (F. Martina)	Date:
Supervisor (P. Colegrove)	Date:
Supervisor (S. Williams)	Date:

Contents

List of Figures

List of Tables

Glossary

α_{GB} Grain boundary α.

α_M α massive.

α_W Widmanstätten.

I_b Base current.

I_p Peak current.

LH_1 Layer height of first layer.

LH_2 Layer height of second layer.

LH_3 Layer height of third layer.

LH_4 Layer height of fourth layer.

WW_1 Wall width of first layer.

WW_2 Wall width of second layer.

WW_3 Wall width of third layer.

WW_4 Wall width of fourth layer.

Acronyms

AM Additive Manufacturing.

ANOVA ANalysis Of VAriance.

BCC Body Centred Cubic.

BTF Buy To Fly.

CAD Computer-Aided Design.

CAM Computer-Aided Manufacturing.

CFRP Carbon-Fibre Reinforced Polymer.

CM Contour Method.

CMT Cold Metal Transfer.

DE Deposition Efficiency.

DLF Direct Laser Fabrication.

DOE Design Of Experiment.

EBM Electron Beam Melting.

EBSD Electron Backscatter Diffraction.

EBW Electron Beam Welding.

EDM Electrical Discharge Machining.

EWW Effective Wall Width.

FCGR Fatigue Crack Growth Rate.

FEA Finite Element Analysis.

GMT Global Mechanical Tensioning.

HCF High Cycle Fatigue.

HCP Hexagonal Close Packed.

HIP Hot Isostatic Pressing.

LCF Low Cycle Fatigue.

LH Layer Height.

LSP Laser Shock Peening.

LW Laser Welding.

MIG Metal Inert Gas.

ND Neutron Diffraction.

PAW Plasma Arc Welding.

PWD Plasma Wire Deposition.

SEM Scanning Electron Microscope.

SLM Selective Laser Melting.

TIG Tungsten Inert Gas.

TS Travel Speed.

TWW Total Wall Width.

UIT Ultrasonic Impact Treatment.

UTS Ultimate Tensile Strength.

WAAM Wire+Arc Additive Manufacturing.

WFS Wire Feed Speed.

WW Wall Width.

Chapter 1

Literature review

1.1 Introduction

In this literature review all the areas involved in the research project will be thoroughly analysed and the "state of the art" of each of them will be presented. A brief historical description of titanium will introduce a presentation of the main application of this element (and its alloys) in industry; material properties will be given; the various microstructures, as well as the processing routes to achieve them, will be discussed, with the mechanical properties and some of the typical issues affecting Ti–6Al–4V such as oxidation and porosity. Additive manufacturing will be reviewed in terms of available technologies, compared in general and for Ti–6Al–4V in particular. Finally, residual stresses will be investigated with specific attention to the additive manufacturing aspect.

1.2 Titanium and its alloys

Titanium is abundant in the Earth's crust, representing about 0.6% of it, fourth in abundance amongst the structural metals (Lütjering and Williams, 2007, p. 2). Towards the end of the 18th century, an English Reverend named William Gregor found in the area of Menakine, Cornwall, dark sands containing the $FeTiO_3$ oxide

(ilmenite) (Morri, 2008). Just few years after, Martin Heinrich Klaproth, a German chemist, isolated and identified TiO_2, and gave the newly formed element the name titanium (Lütjering and Williams, 2007, p. 2).

Before World War II it was impossible to produce titanium that had acceptable quality in terms of mechanical properties, mainly because of its reactivity with oxygen and nitrogen. In 1940, Kroll managed to extract high purity titanium by reducing $TiCl_4$ with magnesium, producing a "sponge" that could eventually be molten and cast into ingots (Morri, 2008). After 70 years, Kroll's process is still the most widely used one (Lütjering and Williams, 2007, p. 2). However, researchers have tried to explore different processing routes to reduce the cost of titanium production. Chen et al. (2000) attempted to reduce pure titanium from TiO_2 by using molten calcium chloride; Shin et al. (2012) used lithium chloride instead. Unfortunately up until now these solutions have failed to meet expectations due to low throughput and O_2 levels above 2000 ppm.

Research into titanium alloying and manufacturing processing began in the early 1950s, leading to the development of the three classes of titanium alloys: α, β and $\alpha + \beta$, to which Ti–6Al–4V belongs, representing the most widely used alloy in today's market. In fact, Ti–6Al–4V accounts for 56% of the USA titanium market (Figure 1.1 from Lütjering and Williams, 2007, p. 7).

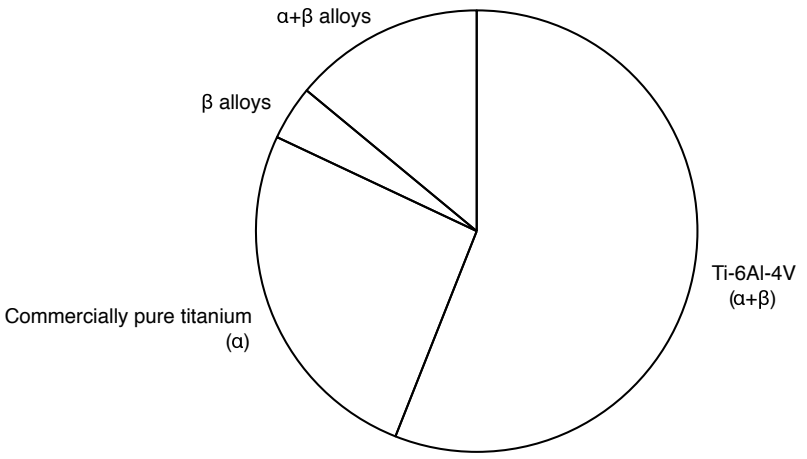

Figure 1.1: USA titanium market in 1998 (Lütjering and Williams, 2007, p. 7).

1.2.1 Applications

Titanium and its alloys are characterised by many features that make them attractive for the aerospace, biomedical, and processing industries. High strength and low density give an excellent strength-to-weight ratio. In addition, good creep resistance and great corrosion resistance make it a suitable material for jet engines and airframes. In the former, titanium is used for frames, fan disks, tail plugs, manifolds, compressor spools, booster spools. In the latter, examples are windows frame forgings, exhaust ducts, fin decks, fuselage, empennage, wings, nacelles (Boyer, 1996). Springs are also an excellent application: titanium density and elasticity modulus are about 60% and 50% of those of steel, respectively, allowing up to 70% weight savings (Boyer, 1996).

Titanium is the preferred material also for landing gear support structures. According to Boyer (1996) Boeing 747's and 757's landing gear beams would have initially been made of an aluminium alloy (e.g. 7075). However, to meet the load requirements the component would have been too large to fit in its envelope in the airframe, forcing the designers to adopt titanium. Moreover, due to the corrosive environment of the wheel compartment, low alloy steel cannot be used. This component weighs more than 800 kg and still represents one of the largest titanium forgings (Boyer, 1996). An exceptional example of massive titanium employment is the Lockheed SR-71 Blackbird reconnaissance airplane (Figure 1.2), in which 95% of the structural weight is titanium (Boyer, 1996).

The growing utilisation of Carbon-Fibre Reinforced Polymers (CFRPs) within the aerospace sector has accelerated the use of titanium, because of the corrosion issues associated with using aluminium and CFRPs together (Boyer, 1996). Carbon fibres are electrically conductive, and electrochemically noble. Consequently aluminium and carbon form a galvanic cell, which enhances the corrosion of the metal components (Liu et al., 2014). The galvanic compatibility of titanium and carbon is about one tenth of that of aluminium and carbon, hence titanium is gradually

Figure 1.2: Lockheed SR-71 Blackbird (Concordebattery.com, 2014).

replacing aluminium components in newly designed aircrafts.

Unsurprisingly titanium production is highly dependent on the aerospace industry (see also p. 22); in fact, a production minimum over the last fifty years was achieved in 1994 and corresponded to a drastic reduction in aircraft orders. To reduce reliance of the aerospace industry and free titanium producers from the cyclical behaviour of this industry, titanium producers have attempted to diversify their business and enter other markets, such as the automotive sector (Lütjering and Williams, 2007, p. 14). Other recent uses of titanium are related to consumer goods: digital camera frames, golf clubs (Lütjering and Williams, 2007, p. 9), high performance and luxury watches, in which titanium nitride, with its golden appearance and extreme hardness, is used to coat gold parts (Skagen, 2012). Titanium is also used in high end racing bicycles as an alternative to CFRPs (Lütjering and Williams, 2007, p. 9; Van-Nicholas, 2012).

Although the attractiveness of titanium alloys given by the possibility of achieving large economies of scale, the shift has presented new challenges related to cost.

When the applications are related to expensive, high performance racing cars, cost may not be a crucial variable; but if the target market is the one of small, every-day cars, then a drastic reduction in costs of either the raw material extraction and/or part manufacturing is definitely necessary (Lütjering and Williams, 2007, p. 359). In fact, titanium costs approximately ten times more than steel or aluminium to produce, and is also extremely costly to machine (Boyer, 1996).

1.2.2 Material properties and classification

Relevant properties for Ti–6Al–4V alloy are presented in Table 1.1. Notable are the high elastic modulus and the low density, which give the highest strength-to-weight ratio of any metal.

Table 1.1: Ti–6Al–4V relevant properties (Lütjering and Williams, 2007, p. 15).

Melting temperature (°C)	1670
Elastic modulus (GPa)	115
Yield Stress Level (MPa)	1000
Density (g/cm^3)	4.42

Three different categories of titanium alloys exist, and are distinguished on the basis of the phases that are observed at room temperature: α, $\alpha + \beta$, and β. Morri (2008) classified titanium alloys as:

- α alloys, if the percentage of β phase is less than five;
- $\alpha + \beta$ alloys, or near α alloys, if the percentage of β phase is between 10 and 20;
- β alloys, or near β alloys, if the percentage of β phase is larger than 20.

In optical micrography images, normally the α phase appears white, surrounded by a black matrix, the β phase. From a crystallographic point of view, each of the two phases is characterised by a different structure: α phase has a Hexagonal Close Packed (HCP) structure (Figure 1.3a), while the β phase has a Body Centred Cubic (BCC) one (Figure 1.3b).

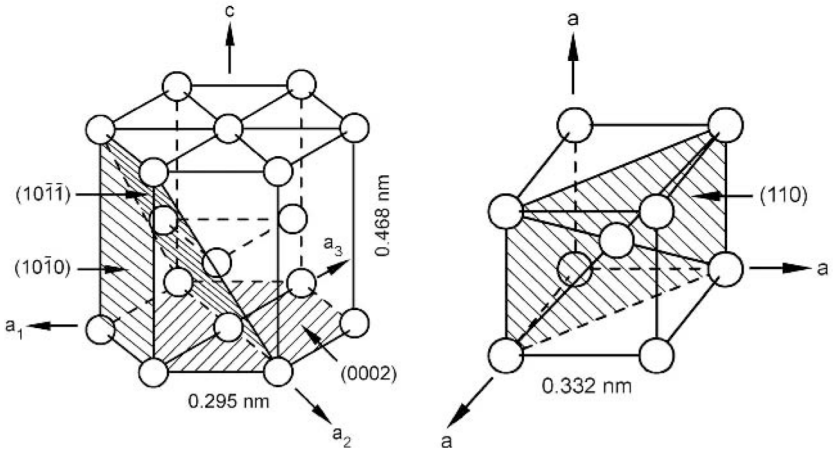

(a) Unit cell of α phase (b) Unit cell of β phase

Figure 1.3: Crystal configurations found in titanium (Lütjering and Williams, 2007, p.16).

For commercial pure titanium, the β-transus temperature, at which the β to α[1] allotropic phase transformation is completed, is 882 °C. The β-transus temperature varies with the quantity and the species of alloying and interstitial elements. If an alloying element increases the β-transus temperature, it is defined α-stabiliser, while if it has the opposite effect it is then considered β-stabiliser (Lütjering and Williams, 2007, pp. 34–37). As will be shown later, the ratio between the quantities of the different phases, and the texture of the α phase, are two of the factors that influence the mechanical properties. With regards to the elastic properties, an important factor is the orientation of the HCP crystals of the α phase. Lütjering and Williams (2007, pp. 16–17) showed that the elastic modulus can vary between 100 GPa to 145 GPa if the stress is perpendicular or parallel to the crystal c-axis, respectively. Also the shear modulus varies between 34 GPa to 46 GPa for stress in the (0002) and {1010} planes, or <1120> direction, respectively. With regards to polycrystalline materials, these properties have a strong dependence on the type and intensity of the texture.

[1]Upon cooling

1.2.3 Ti–6Al–4V microstructure

Ti–6Al–4V is the alloy used for the present investigation, and consequently its microstructure will be presented in depth. Moreover, many authors in the literature use different nomenclatures; therefore this review will present the one used for the rest of the work.

Ti–6Al–4V β-transus temperature is around 1000 °C and varies slightly according to the small variations in the quantities of interstitial elements. The cooling rate from the β-transus to the room temperature greatly affects the final microstructure. β phase can transform into α phase in two ways: by a diffusion process, consisting of nucleation and growth of α phase nuclei in the prior β grains, or by a diffusionless transformation (Gil et al., 2001).

In the case of Additive Manufacturing (AM) applications, it is usual to manufacture components characterised by different local microstructural features (Baufeld et al., 2011), due to the complexity and inconsistency of the heat treatments induced in the part by the deposition of each layer. Consequently, the classification of a specimen into a specific category is inconvenient in reality, for the final structure is quite varied. Nevertheless, understanding the mechanism of microstructure formation is useful to infer the thermal history of the component from the observation of the final structure, and to predict some of the mechanical properties.

1.2.3.1 Microstructures obtained by diffusional processes

Different microstructures can be achieved, depending on the heat treatments (and eventual mechanical processing) the alloy undergoes: fully lamellar, bi-modal and fully equiaxed (Lütjering and Williams, 2007). However, many steps — both thermal and mechanical — are necessary in order to get a consistent type of microstructure. These are: homogenisation, deformation, recrystallisation, and a final annealing step.

Fully lamellar Homogenisation, deformation and recrystallisation steps must be above the β-transus temperature (Figure 1.4a) to achieve a fully lamellar structure. At cooling rates below 410°C/s, α phase starts forming along grain boundaries (α_{GB}) and grows perpendicularly in the β phase matrix in the form of needles or platelets (Figure 1.5a); it is called Widmanstätten or basketweave structure (Figure 1.5b), and is denoted with α_W (Gil et al., 2001). The cooling rate of the homogenisation step influences the length and width of the α lamellae: the higher the rate, the smaller the lamellae (Figure 1.4, images (b) to (d)) (Lütjering, 1998).

For very low cooling rates (less than $1\,^{\circ}\mathrm{C\,s^{-1}}$) the α phase in between grain boundaries appears smaller, and α massive (α_M) (Gil et al., 2001) nucleates in the matrix as well (Figure 1.5d). Because of the low cooling rate, the alloying elements

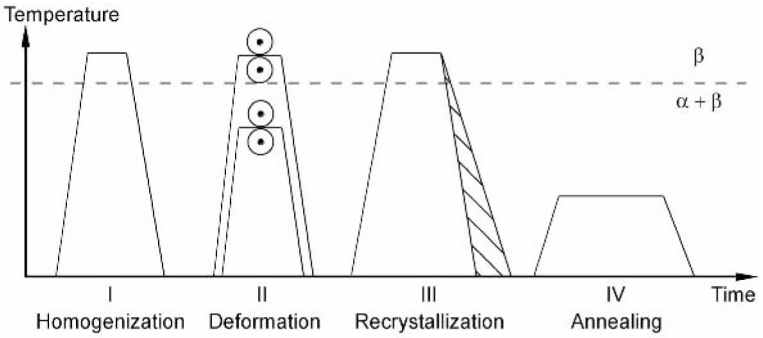

(a)

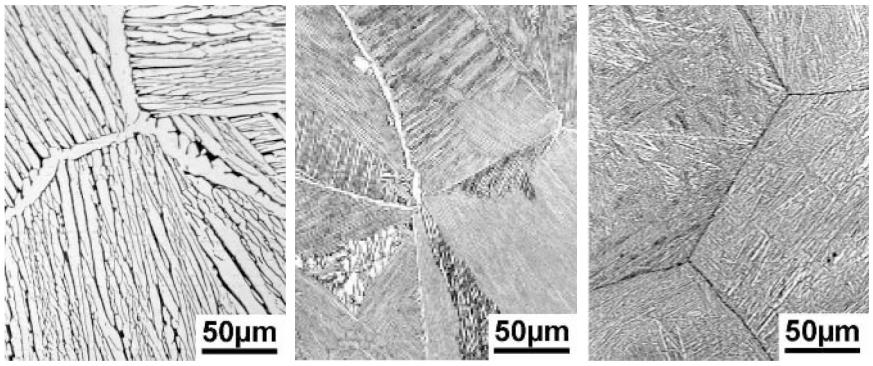

(b) $0.02\,^{\circ}\mathrm{C\,s^{-1}}$ (c) $1.67\,^{\circ}\mathrm{C\,s^{-1}}$ (d) $133\,^{\circ}\mathrm{C\,s^{-1}}$

Figure 1.4: (a) Processing steps to achieve fully lamellar microstructure; and (b), (c), (d) effect of cooling rates on lamellar microstructure of Ti–6242, (Lütjering and Williams, 2007, pp. 204–205). Please note the circles in the deformation step indicate hot deformation; the dashed slope means different cooling rates can be chosen according to the desired final microstructure.

can diffuse towards the matrix and aid the nucleation. In general, the lower the cooling rate, the higher the $^{\alpha_M}/_{\alpha_W}$ ratio; for extremely low cooling rates ($0.81\,^{\circ}\mathrm{C\,s^{-1}}$) it is possible to see a great amount of α_M and a reduced amount of α_W (Gil et al., 2001).

Both α_M and α_W are generally defined as primary α, which is distinguished from secondary α (Figure 1.5c), that finely precipitates in the β phase matrix during ageing (Sauer and Lütjering, 2001).

Widmanstätten (or basketweave) (Figure 1.5b) is a particular type of lamellar structure. When cooling rate increases or when newly nucleated lamellae collide with each other and cannot grow further, nucleation starts not only on boundaries of β grains, but also on boundaries of already developed α colonies/lamellae. The preferential growth direction is perpendicular to the existing α colony growth direction, because it minimises the overall elastic strains (Lütjering and Williams, 2007).

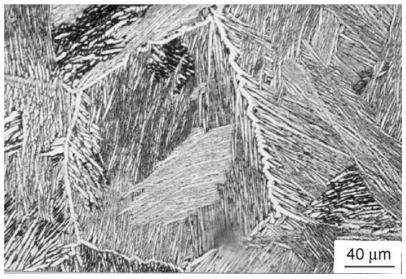

(a) Micrography of α_{GB} (Filip et al., 2003)

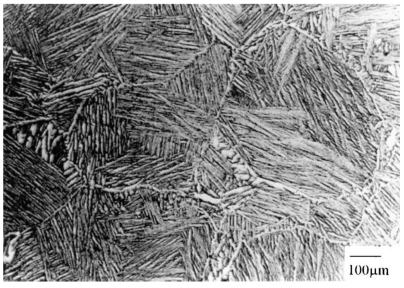

(b) Widmanstätten microstructure cooled at $3.40\,^{\circ}\mathrm{C\,s^{-1}}$ (Gil et al., 2001)

(c) Secondary α (Sauer and Lütjering, 2001)

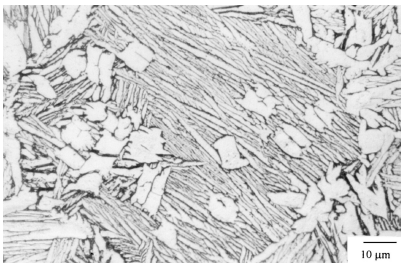

(d) α_M (Gil et al., 2001)

Figure 1.5: α phase morphologies.

Bi-modal The necessary steps to achieve the bi-modal microstructure are: homogenisation, deformation, recrystallisation and annealing. However, unlike the processing conditions for the fully lamellar microstructure, the only step performed above the β-transus temperature is homogenisation (Figure 1.6a). This microstructure consists of a matrix of $\alpha+\beta$ lamellae in which there is primary α (Figure 1.6b).

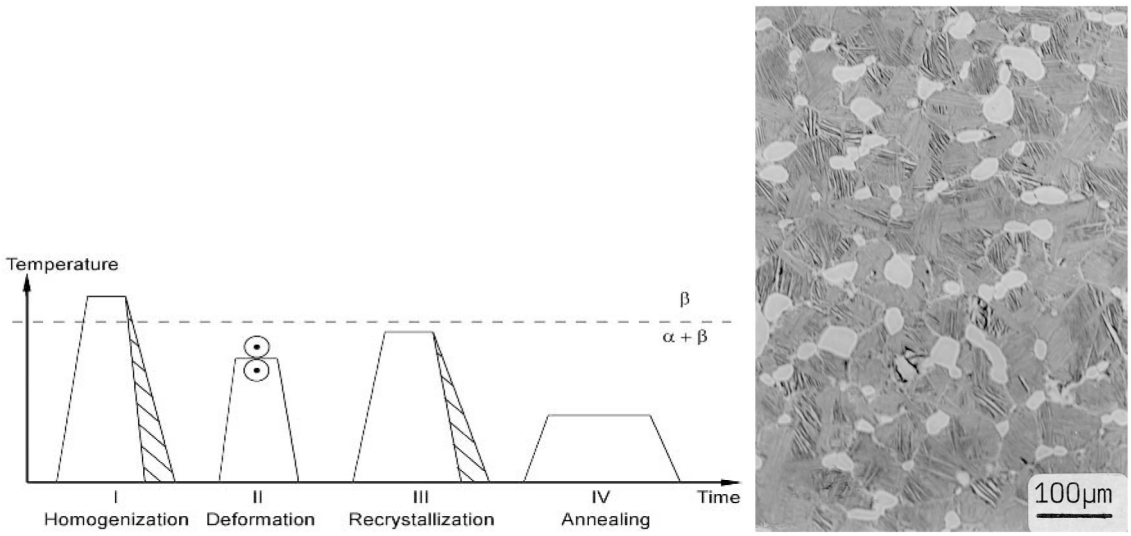

(a) (b)

Figure 1.6: Bi-modal microstructure: (a) processing conditions, (Lütjering and Williams, 2007, p. 208), and (b) micrography (Lütjering, 1998). Please note the circles in the deformation step indicate hot deformation; the dashed slopes mean different cooling rates can be chosen according to the desired final microstructure.

Fully equiaxed The processing conditions to achieve the fully equiaxed structure coincide with those of the bi-modal structure, except for the cooling rates of the homogenisation and recrystallisation steps which are lower (Figure 1.7a). This is necessary in order to allow the growth of primary α phase grains only, rather than the formation of a lamellar structure within the α grains themselves.

However, another way of obtaining the same structure consists in recrystallising at lower temperatures (Figure 1.7b), at which the α phase equilibrium volume fraction is large enough to stimulate the growth of the α phase grains from the lamellae deformed during the deformation step. This method has the advantage

of producing finer α phase grains (about 2 µm) (Lütjering and Williams, 2007). In this microstructure, the β phase is located at the triple points of α phase grains (Figure 1.7c).

The fully lamellar, bimodal and fully equiaxed types of microstructures are summarised in Figure 1.8.

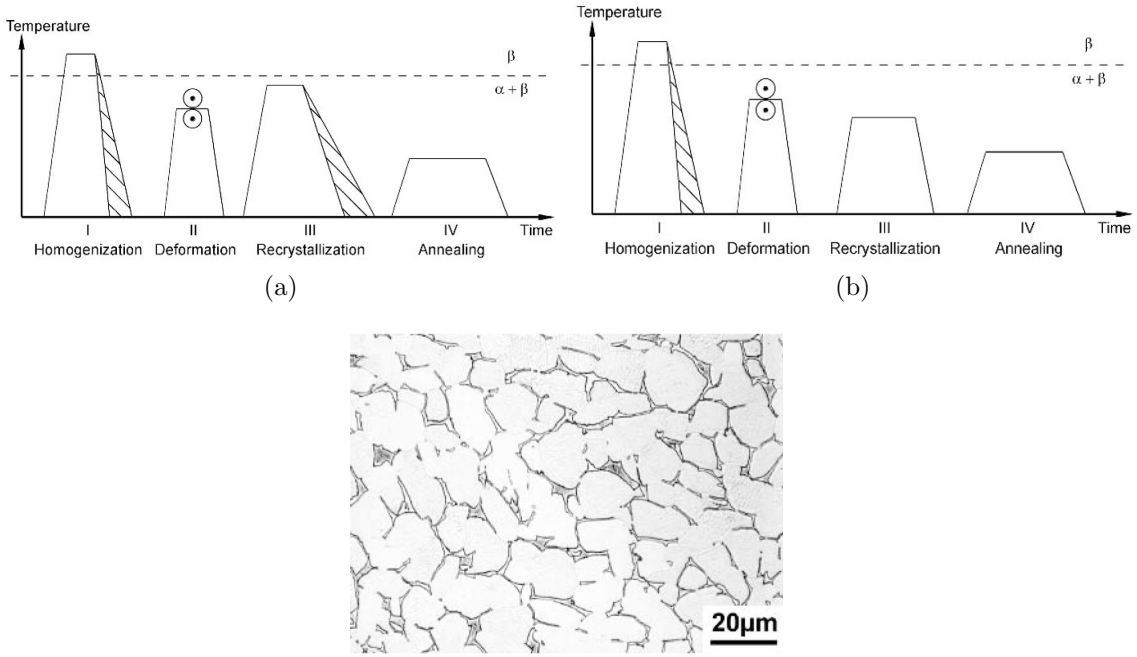

Figure 1.7: Fully equiaxed microstructure: (a) processing conditions, (b) alternative with lower recrystallisation temperature and (c) micrography (Lütjering and Williams, 2007, pp. 212–213). Please note the circles in the deformation step indicate hot deformation; the dashed slopes mean different cooling rates can be chosen according to the desired final microstructure.

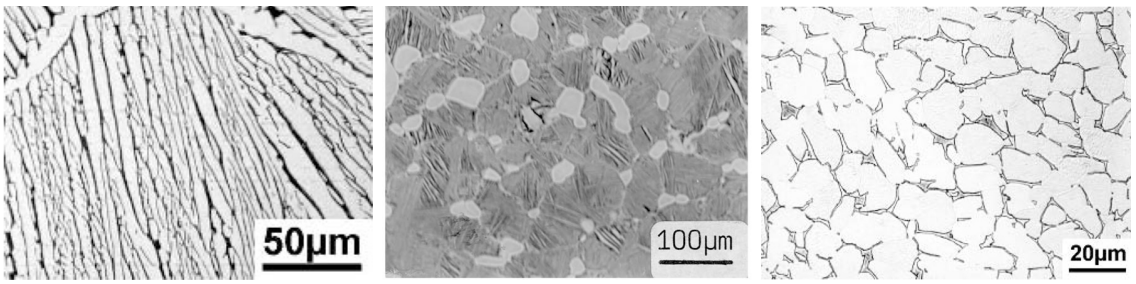

(a) Fully lamellar (b) Bi-modal (c) Fully equiaxed

Figure 1.8: Summary of typical microstructures (Ti–6242).

1.2.3.2 Microstructures obtained by diffusionless processes

For the transformation to be completely diffusionless, cooling must happen at extremely high rates, of the order of $410\,^{\circ}\mathrm{C\,s^{-1}}$ or more (Ahmed and Rack, 1998, see Figure 1.9). At this rate, a shear type transformation occurs, the outcome being a non-equilibrium phase with a distorted structure.

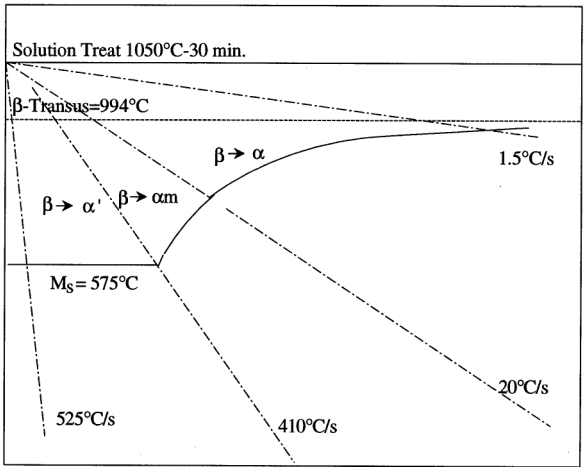

Figure 1.9: Schematic continuous cooling diagram for Ti–6A4–4V solution treated at 1050 °C for 30 min (Ahmed and Rack, 1998). M_S indicates the martensite start temperature and is from Majdic and Ziegler (1973).

Martensite Martensite is a designated as α' and it usually has the same crystallographic structure as the general α phase (HCP). For this reason it is difficult to identify its presence with X–Ray diffraction. Some authors including Ahmed and Rack (1998), Lee (2004), Qazi et al. (2003) suggested that α' can be differentiated from its needle-like appearance (Figure 1.10) and its characteristic arrangement in a grid of perpendicular, fine lamellae. Lütjering (1998) agrees and describes martensite as a microstructure in which "slip length and colony size are equal to the width of individual α plates", which is 0.2 µm on average.

However, another martensite type exists, denoted α", characterised by an orthorhombic structure; it is also a non-equilibrium phase, and can be found in Ti–6Al–4V as well as in alloys richer in tantalum, niobium or molybdenum (Filip et al., 2003). According to Lütjering and Williams (2007, p. 30), when annealing in the $\alpha + \beta$

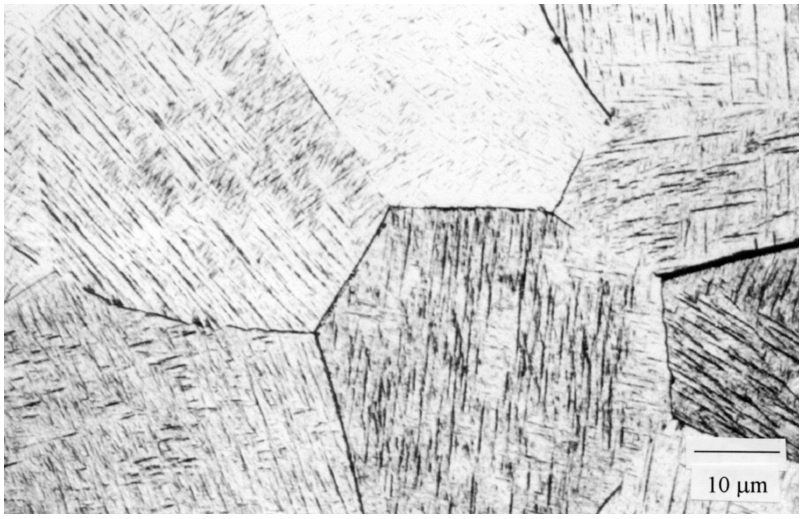

Figure 1.10: Micrography of α' martensite (Gil et al., 2001).

field, the orthorhombic martensite seems to decompose spinodally in solute lean α" and solute rich α", prior to the final β phase precipitation ($\alpha"_{lean} + \alpha"_{rich} \rightarrow \alpha + \beta$).

According to Gil et al. (2001), Lütjering and Williams (2007), having martensite even in specimens cooled at the rate of $1.6\,^{\circ}\mathrm{C\,s^{-1}}$ is still possible; at this cooling rate, the size of α colonies starts reducing significantly. For a cooling rate of $130\,^{\circ}\mathrm{C\,s^{-1}}$, the size of α colonies reduces to the size of individual plates.

1.2.4 Microstructure and mechanical properties

There is a close correlation between microstructural features and mechanical properties, and consequently between cooling rates/mechanical processing and mechanical properties. In the present section, this relationship will be reviewed only in regards to the fully lamellar microstructure, which exists in parts built by AM (Baufeld et al., 2011, Martina, 2010, Wang et al., 2011).

1.2.4.1 Tensile properties

According to Lütjering (1998), in the case of a fully lamellar microstructure, mechanical properties depend on the the size of α colonies (Figure 1.11) and prior β grains; the former depends especially on cooling rates during the end of the process-

ing steps.

It is reported that the yield strength is constant for cooling rates below $1.6\,^{\circ}\mathrm{C\,s^{-1}}$ (900 MPa); then it increases slowly until $15\,^{\circ}\mathrm{C\,s^{-1}}$ (around 920 MPa) and reaches its maximum just below $166\,^{\circ}\mathrm{C\,s^{-1}}$ (1100 MPa). Lütjering (1998) attributes the increase in the yield strength to the martensitic structure of the specimens cooled at high rates.

Lütjering (1998) demonstrated that elongation increases with increasing cooling rates, reaching its maximum at 8% for any cooling rate between $1.5\,^{\circ}\mathrm{C\,s^{-1}}$ to $15\,^{\circ}\mathrm{C\,s^{-1}}$, and then decreases dramatically for higher cooling rates. In the same work, Lütjering (1998) explained the decrease in ductility with the change in the fracture mode, which goes from being ductile transcrystalline to ductile intercrystalline. Filip et al. (2003) presented slightly different results, asserting that the maximum elongation (9%) corresponded to $7\,^{\circ}\mathrm{C\,s^{-1}}$. It must be noted that the elongation values reported by both Filip et al. (2003), Lütjering (1998) are relatively lower than those reported by Baufeld et al. (2009), Wang et al. (2013) for a very similar microstructure.

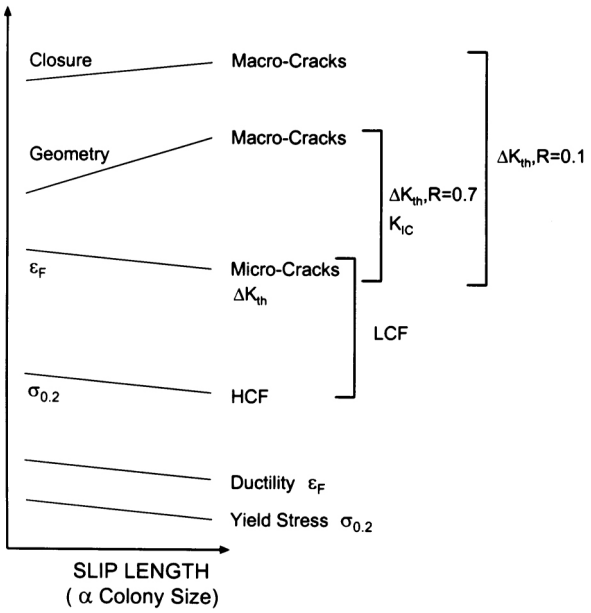

Figure 1.11: Effect of slip length (α colony size) on Ti–6Al–4V mechanical properties (Lütjering, 1998).

According to Gil et al. (2001), Morri (2008), if the Ultimate Tensile Strength (UTS) of the lamellae is comparable to or smaller than that of the α phase at the grain boundary (α_{GB}), deformation happens in both lamellae and α_{GB}. In the case of very fine lamellae, such as in the martensite or in some Widmanstätten, the UTS of the lamellae is higher than that of the α_{GB}. Therefore, deformation happens exclusively in the α_{GB} leading eventually to crack nucleation and intercrystalline fracture.

In $\alpha + \beta$ alloys, continuous α phase precipitations can be found at the prior β grain boundaries, where the growth of the α phase starts in most cases. The difference in strength between the α phase located at grain boundaries, and matrix regions affects the fracture behaviour, especially in the case of large prior β grains, due to the increased slip length (Lütjering et al., 2007, Morri, 2008, Sauer and Lütjering, 2001).

Please note that both the dimensions of α colonies and prior β grains determine the effective slip length. Consequently, if deformation occurs in the α_{GB} (when the UTS of the lamellae is higher than that of the α_{GB}), the effective slip length depends on the size of the prior β grains because α_{GB} is as long as the grain boundary. If deformation happens within the α colonies then the slip length is given by the size of the lamellae (Morri, 2008).

According to Dehghan-Manshadi et al. (2010), α_{GB} is also affected by cooling rate, its thickness varying from more than 10 µm to 1 µm for cooling rates from 0.5 °C s^{-1} to 10 °C s^{-1}, respectively.

1.2.4.2 Damage tolerance properties

Lütjering (1998) stated that High Cycle Fatigue (HCF) strength has similar behaviour to the yield strength, increasing with the cooling rate. Low Cycle Fatigue (LCF) strength depends on both resistance to crack nucleation and propagation of microcracks (small cracks on the surface), the latter depending also on slip length.

In fact, microcrack propagation decreases when the cooling rate rises, since α colony boundaries and martensitic regions act as obstacles (Lütjering, 1998). Therefore, in terms of LCF strength, the higher the cooling rate, the better.

In terms of Fatigue Crack Growth Rate (FCGR), two factors must be considered: ductility and crack front geometry. As for the latter, an increase in α colony size causes an increase in crack front roughness, which hinders crack propagation and increases ΔK_{th}. Ductility however shows an opposite response, reducing with α colony size as shown in Figure 1.11. Depending on the gradients from Figure 1.11, FCGR could either increase or decrease as the α colony size increases (which affects the slip length), therefore it cannot be stated beforehand whether the combined effect of ductility and crack front geometry will aid or hinder large crack propagation. According to Lütjering (1998), at high R ratios[2] usually in $\alpha + \beta$ alloys an increase in α colonies size corresponds to a decrease in FCGR; consequently, crack front geometry is the predominant contribution. However, Lütjering (1998) assumes ductility behaviour is linear, in contrast with what he stated previously about elongation. In his considerations, the author is probably excluding the area in which ductility is badly affected by cooling rates, because of the difficulty in achieving them in practice, given their high magnitude.

Crack closure is another factor to be considered in the case of low R ratios; it follows the behaviour of crack front geometry, increasing with crack surface roughness and shear displacement at the crack tip. Therefore, at low R ratios an increase in α colony size has a beneficial impact on crack propagation, as shown in Figure 1.12 from Lütjering (1998). The fracture toughness of Ti–6Al–4V is similar to that of the FCGR: the larger the size of α colonies, the better the fracture toughness, due to the predominance of crack front geometry over ductility (Lütjering, 1998).

In conclusion, for $\alpha + \beta$ alloys, α colony size appears to be the most critical parameter in terms of mechanical properties: smaller colonies result in an increase

[2] $R = {}^{Min.\ stress}/_{Max.\ stress}$

in all mechanical properties, except for FCGR (for both high and low R ratios) and fracture toughness.

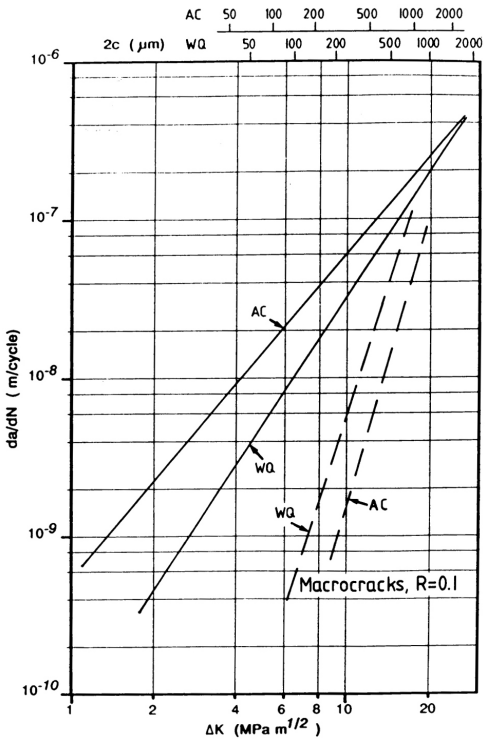

Figure 1.12: Effect of cooling rate on crack propagation for fully lamellar microstructure of Ti–6242 (Lütjering, 1998).

1.2.5 Welding of Ti–6Al–4V

The most common methods for joining Ti–6Al–4V are fusion and friction stir welding (Lütjering and Williams, 2007, p. 104). In general, as the strength of the alloy increases, it becomes more difficult to weld, due to the presence of eutectoid alloying elements (e.g. iron or chromium) which cause cracking (Lütjering and Williams, 2007, p. 104). Although the fusion and heat affected zones can be identified, they are more difficult to distinguish than most alloys (Lütjering and Williams, 2007, p. 105). In the case of $\alpha + \beta$ alloys, due to the different temperatures and cooling rate experienced during the welding process, it is common to see diverse microstructures which result in a local variation of the mechanical properties (Lütjering and Williams, 2007, p. 106). However, in practice this variation is much smaller than

most alloys.

Within the fusion welding techniques, the adopted ones are Metal Inert Gas (MIG) (Patnaik et al., 2011), Tungsten Inert Gas (TIG) (Ellis and Gittos, 1995), Plasma Arc Welding (PAW) (Roggensack et al., 1993), Electron Beam Welding (EBW) (Mohandas et al., 1999) and Laser Welding (LW) (Akman et al., 2009, Casalino et al., 2005, Roggensack et al., 1993, Zhang and Zhang, 2011). A hybridisation of MIG and LW was attempted successfully (Denney et al., 2005, Li et al., 2009) to enable welding at high processing speeds with low heat input. The most common technique is TIG, which is extremely suitable for large components with thin sections (Lütjering and Williams, 2007, p. 108). Given the chemical reactivity of titanium, local shielding is necessary around the welding torch, to prevent contamination with oxygen, nitrogen and hydrogen. Oxygen contamination becomes severe for temperatures above 550 °C; below this temperature the diffusion rates are low and there is not significant formation of α casing (Lütjering and Williams, 2007, p. 51). Often additional protection is provided by using a trailing shield. In addition a backing (or underbead) shielding device is sometimes provided to protect the rear surface of the part (Lütjering and Williams, 2007, p. 108.). Therefore, for standard and repetitive welding it is sometime more convenient to adopt a chamber which is filled with an inert gas (Lütjering and Williams, 2007, p. 108).

Porosity and oxidation are two defects that can occur when the components are contaminated or shielding is not appropriate; their effect on the mechanical properties will be discussed in the following sections.

1.2.5.1 Influence of porosity

Without any doubt, porosity affects mechanical properties, and all welding processes are affected by this problem to some extent. Reported causes, in general, are non-optimal gap distance (Akman et al., 2009), welding speed (Mohandas et al., 1999), cleanliness of the joint (in terms of oxide layer and grease), black dust generated by

laser welding, and weld width (Mueller et al., 2006)

According to Akman et al. (2009), in laser welding of Ti–6Al–4V the best result was obtained with a gap distance of 0.1 mm, and the edges of the plates must be carefully milled to made them as smooth as possible. The authors suggest that porosity is caused by the entrapment of gases during the solidification of the molten metal, and they demonstrate how porosity increases with the average power, which results in a reduction in UTS. A porosity ratio[3] of ca. 0.75% corresponds to 500 MPa, and a ratio of 2% to 200 MPa. Unfortunately the authors do not provide any information on the pore size; porosity seems concentrated in the weld metal.

Cao and Jahazi (2009) studied the effect of welding speed on butt joint quality, and report that in the specimen with the lowest strength, cracks initiate at a micropore. They conclude that the loss in elongation in their joints was caused by micropores (and aluminium oxides).

Tsay et al. (2006) stated that porosity might not increase fatigue crack growth. In their study, when cracks avoid porosity FCGR is comparable to that of defect free specimens. They added that porosity actually reduces FCGR, possibly because of the increase in the radius of the crack tip due to the penetration of crack front into the pore which results in a blunt crack notch, and the local rupture plasticity. Moreover, fractography showed no change in crack morphology when comparing porous welds to defect free ones, except for a larger fracture surface around porosity.

Mohandas et al. (1999) studied the effect of welding speed in EBW, and concluded that all porosity parameters (maximum pore size, total number of pores, number of pores per unit area, average area of pores, and porosity ratio) are maximised at intermediate speeds (ca. $0.025\,\mathrm{m\,s^{-1}}$), except for the number of pores per mm^2. Gas bubbles life cycle consists of formation, growth and escape. The authors conclude that at low welding speeds (around $0.02\,\mathrm{m\,s^{-1}}$) bubbles have time to form, grow and escape, due to the high heat input which causes a long lasting molten pool.

[3] Area of pores divided by area examined

At high welding speeds (from $0.03\,\mathrm{m\,s^{-1}}$ to $0.04\,\mathrm{m\,s^{-1}}$), bubbles do not have the time to form, as the molten pool solidifies rapidly. At intermediate speeds, bubbles do have the time to form and grow but not to escape, therefore porosity is significant. The authors did not test any mechanical properties. Anyway, EBW is naturally prone to porosity due elements evaporation (Huang, 2011).

1.2.5.2 Influence of oxygen

Oxygen is one of the alloying elements in Ti–6Al–4V, and it is required for strengthening. It acts as α phase stabiliser, and it has been demonstrated that an increase from 0.09 wt.% to 1.0 wt.% corresponds to an increase in β-transus temperature from 965 °C to 1180 °C (Kahveci and Welsch, 1986). This dependency is characterised by the following equation:

$$\beta_{transus}(^{\circ}C) = 937 + 242.7 \times O(wt.\%) \tag{1.1}$$

Kahveci and Welsch (1986) show how, at a given temperature, higher concentrations of oxygen resulted in an increase of α phase volume fraction. Consequently, oxygen increases both the strength and elastic modulus. However, concentrations above 2% lead to embrittlement and should therefore be avoided. In fact, a ductile to brittle transition occurs for concentrations between 0.26 wt.% to 0.56 wt.% (Kahveci and Welsch, 1991).

According to the same authors (Kahveci and Welsch, 1986), oxygen also affects hardness. Hardness curves are characterised by a minimum value which depends on the quench start temperature; when oxygen content increases, so does the quench start temperature. For quenching temperature values below minimum hardness, the hardness is always constant, because the phase change from α to β does not occur.

In both Kahveci and Welsch (1986, 1991) the authors demonstrate a parabolic correlation between oxygen content and hardness, which does not depend upon heat

treatments conditions. On the contrary, the relationship between hardness and both yield strength and UTS is affected by strain hardening, which depends on heat treatments. The relationships between hardness and oxygen content, yield strength, and UTS are described by the following equations (Kahveci and Welsch, 1991):

$$H_v = H_0 + b \times O^{\frac{1}{2}} \tag{1.2a}$$

$$H_v = A \times \sigma_{0.2} \tag{1.2b}$$

$$H_v = B \times UTS \tag{1.2c}$$

where H_v is the Vickers Hardness; H_0 is the hardness of a Ti–6Al–4V alloy without any oxygen, b is a constant, $\sigma_{0.2}$ is the yield strength. A and B are two constants that vary between 3.4 to 4.07 (depending on the heat treatment) and from 3.1 to 3.2, respectively. Knowing the hardness, these equations can be used to determine fairly accurate estimations of yield strength and UTS.

Figure 1.13 shows the effect of oxygen on elongation (Figure 1.13a, from Miura et al., 2010), and yield strength, UTS and elongation (Figure 1.13b, from Ebel et al., 2012). The plots suggest that above a critical oxygen content of 0.33 % in weight there is a substantial drop in ductility. On the contrary, yield strength and UTS increase due to a larger martensite fraction.

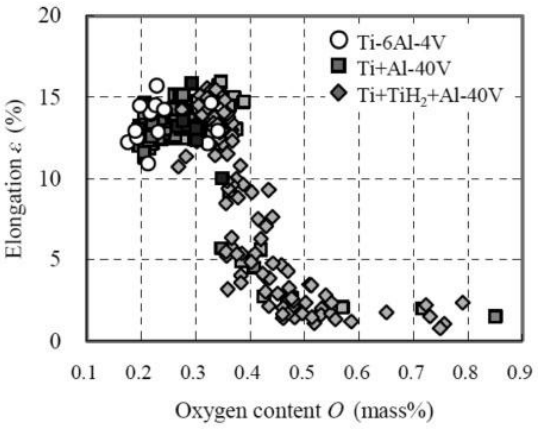

(a) From Miura et al. (2010)

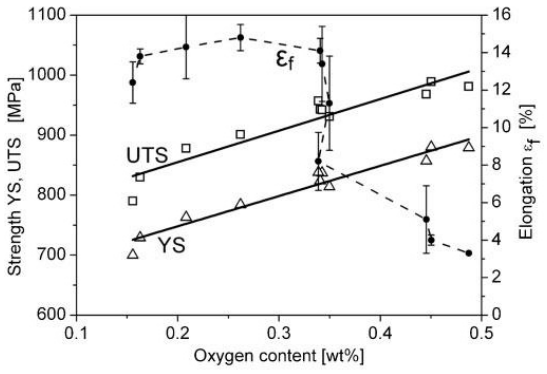

(b) From Ebel et al. (2012)

Figure 1.13: Tensile strength and elongation of as sintered titanium alloys vs. oxygen content. Samples were manufactured by metal injection moulding.

1.3 Additive manufacturing

As opposed to the subtractive approach, Additive Manufacturing (AM) consists of building a component by laying firstly a layer on top of a base plate (the substrate) and then adding subsequent layers to produce the final part (Martina, 2010). AM is a technology which promises to reduce part cost by reducing time to market and material wastage (Coykendall et al., 2014). One industry which is investing heavily in AM is the aerospace sector.

The Buy To Fly (BTF) is the ratio of the mass of the initial workpiece to the one of the finished product; the current method of manufacturing large structures such as cruciforms, stiffened panels, wing ribs, etc., which are machined from billets or large forgings, delivers unsustainable BTFs of 10 or even 20 (Allen, 2006). Furthemore, AM can also enable an increase in design freedom, which potentially results in weight saving as well as facilitating the manufacture of complex assemblies formerly made of many subcomponents (Cotteleer and Joyce, 2014).

According to Airbus (2008), passengers miles are predicted to grow by 2.75 times (5% per year) in the next 20 years. This equates to orders worth over £1.2 T for freight aircrafts. At the current BTF ratios, this will require an estimated 20 million tonnes of billet stock, 80% of which will be machined away. Considering that titanium is extremely expensive in terms of purchase cost ($>$£70 kg^{-1}), energy consumption ($>$500 $\mathrm{MJ\,kg}^{-1}$) and CO_2 emissions ($>$40 $\mathrm{kg\,kg}^{-1}$), in the aerospace industry there is a pressing need for the development of a process which could replace the current manufacturing method.

From an analysis of the literature, three constituents are essential for AM:

- heat source;
- raw material;
- manipulator.

Different heat sources and raw material forms exist. Their combination leads to the

creation of a wide spectrum of different AM techniques, each of them characterised by distinctive features, with benefits and drawbacks, which make them suitable for specific applications, as will be discussed in section 1.3.2 on page 31.

Heat sources are borrowed from the welding world; therefore, they can be either welding torches or laser and electron beams, or even combinations of both. Raw material is fed in various forms (currently powder or wire) into the system; heat is necessary to raise the temperature, which is brought above the material's melting point. The manipulator traces the tool path defined for each layer.

1.3.1 Deposition techniques

In the following sections an overview of the current AM techniques will be presented, based upon whether the adopted heat source is beam or arc-based.

1.3.1.1 Beam-based AM

Beam-based AM techniques are those which use laser or electron beams as the heat source. If laser-based techniques are considered, a further differentiation is the way in which the material is supplied.

Direct laser fabrication In Direct Laser Fabrication (DLF) (Wang et al., 2008), direct laser deposition (Baufeld et al., 2009), lasforming (Arcella and Froes, 2002), or laser engineering net shaping (Rangaswamy et al., 2005), the material is in the form of powder and is blown directly into the molten pool created by the laser beam (Figure 1.14a). Powder feed rate is controlled and the laser beam follows the path which corresponds to the specific direction determined by the Computer-Aided Design (CAD) file. By mixing two or more powders, the alloy composition of the deposited component can be continuously varied. Wang et al. (2007a,b) successfully combined wire and powder feeding to manufacture compositionally graded parts, by feeding TiC powder and Ti–6Al–4V wire. According to Arcella and Froes (2002),

deposition rates range from 0.9 to 4.5 kg h^{-1}. AeroMet Inc., USA had a machine developed for large rib-on-plate components equipped with an 18 kW CO_2 laser. Unfortunately the division was closed due to financial issues. Parts built by DLF are shown in Figure 1.14b.

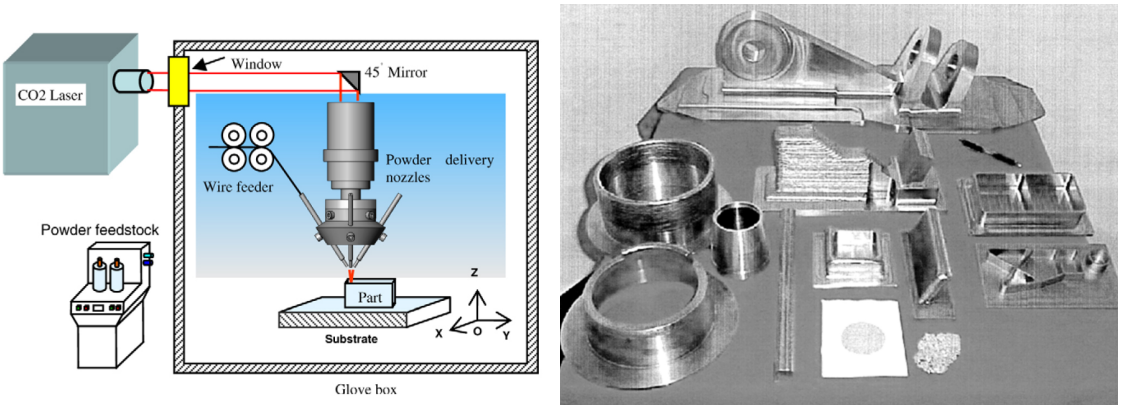

(a) (b)

Figure 1.14: Direct laser fabrication (a) setup (Wang et al., 2007b) and (b) manufactured parts (Arcella and Froes, 2002).

Selective Laser Melting Selective Laser Melting (SLM) (Abe et al., 2001) consists of placing a powder layer with a thickness between 20 µm and 50 µm on a substrate, which is then scanned by a laser beam (similarly to DLF) as shown in Figure 1.15a. After the laser has finished scanning the cross sectional path, a new powder layer is laid and next layer's path is scanned.

A controlled atmosphere is compulsory and to avoid contamination parts bigger than 350×300×200 mm^3 cannot be built given the current technology, because of the cost requirement of a large controlled-atmosphere chamber. (Buijs, 2011). Abe et al. (2001), Tolochko et al. (2004) reported that balling is another limitation affecting SLM: the laser spot only partially melts the area around its focal spot, leaving metal balls due to surface tension in the liquid state. These solid droplets characteristically have an oxide film, which prevents the creation of bonds between the previous and the new layers. Moreover, as balls are contaminated with oxide, recycling them is expensive and not worthwhile. Heat input concentration and temperature gradient

mechanisms also generate residual stress and distortion (Zäh and Branner, 2010); heat treatments are often necessary before parts can be used. SLM applications include biomedical implants, moulds, aerospace and automotive parts (Figure 1.15b from Zäh and Branner, 2010).

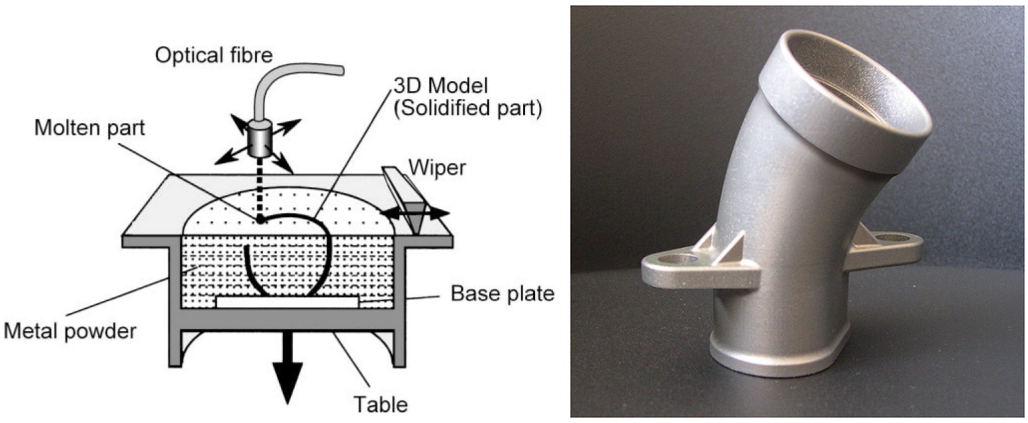

(a) (b)

Figure 1.15: Selective laser melting (a) setup (Abe et al., 2001) and (b) manufactured part (CRP-Technology, 2011).

Electron beam melting In Electron Beam Melting (EBM) (Murr et al., 2009, 2010a,b) an electron beam scans a powder bed, creating layers of ca. 20 µm to 100 µm (Zäh and Lutzmann, 2010), as shown in Figure 1.16a from Murr et al. (2010a).

Zäh and Lutzmann (2010) claim EBM has high penetration depths and scanning speed to enable higher deposition rates in EBM than SLM. Currently the process is completely automated, and the layers are extracted from a scanned model or a 3D CAD drawing. EBM is affected by balling as well, because the wetting ability of the previous layer is lower than the surface tension of the molten material (Zäh and Lutzmann, 2010). Moreover delamination, the detachment or incomplete bonding of a new layer on the previous one, occasionally leads to abortion of the build process. Shielding is not required as the parts are built under vacuum, which is also responsible for volatilisation of light elements. Finally, according to Arcam AB® (2014) which currently are the only EBM machine supplier, residual stress

and distortion are minimal due to powder bed preheating. The preferred field of application is the manufacture of biomedical components and prototypes, mainly using Ti–6Al–4V. A sample produced by EBM is shown in Figure 1.16b.

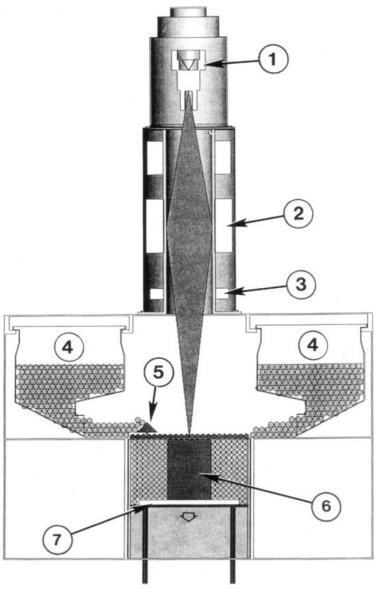

(a) (1) electron gun (2) lens system (3) powder layer (4) powder cassettes (5) rack (6) component (7) table

(b)

Figure 1.16: Electron beam melting (a) setup (Murr et al., 2010a) and (b) manufactured part (CRP Technology, 2011).

Sciaky The combination of electron beam and wire feeding, under vacuum, has been investigated in the USA by a company named Sciaky (2014a). A typical machine is shown in Figure 1.17a; a part in as-deposited and machined conditions is shown in Figure 1.17b and Figure 1.17c. This process aims at overcoming the low deposition rate of EBM and is targeting the manufacture of large scale components. However the requirement for vacuum places the cost of the equipment in the range of $2 M to $3 M which hinders the adoption of this process, especially in the current early stages of AM.

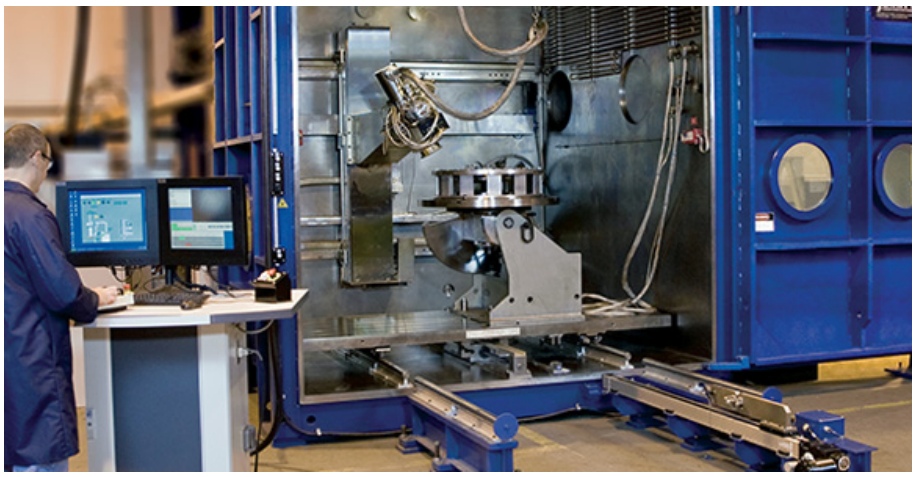

(a)

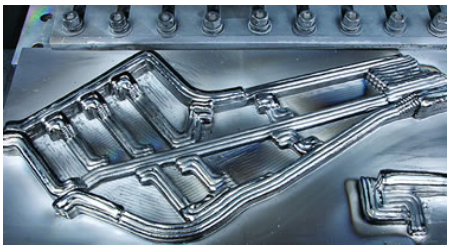

(b)

(c)

Figure 1.17: Sciaky (a) deposition chamber (Sciaky, 2014c), (b) as-deposited part (Additivemanufacturing.com, 2014) and (c) finished part (3Dprint.com, 2014).

1.3.1.2 Arc-based AM

Arc-based AM techniques are those who use arc-based welding processes to supply heat. They have been named either Wire+Arc Additive Manufacturing (WAAM) (Almeida and Williams, 2010) or shaped metal deposition (Acheson, 1990). When a MIG process is not used, this approach consists of a combination of an arc welding torch and an external wire feeding unit, mounted either on a robot or a CNC manipulator (Figure 1.18a). A honeycomb structure build by WAAM is shown in Figure 1.18b.

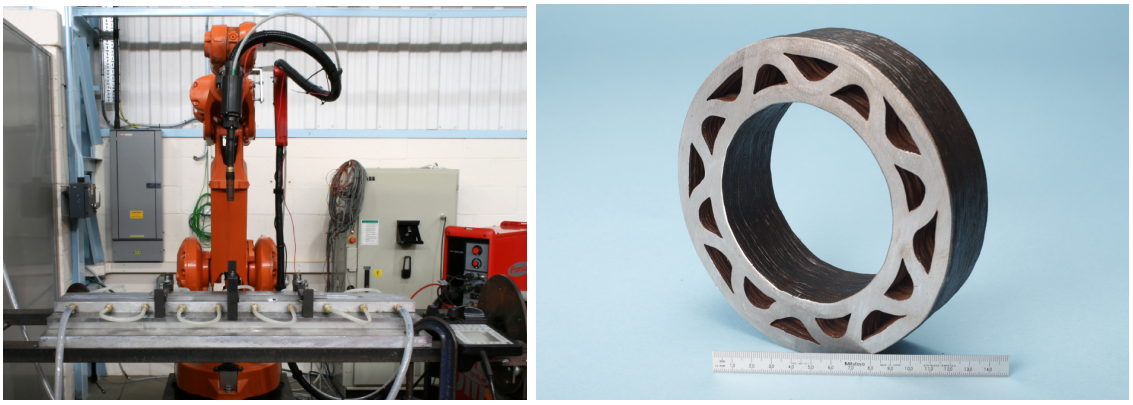

(a) (b)

Figure 1.18: Wire+arc additive manufacturing (a) setup and (b) manufactured part (from an internal report from Cranfield University).

Forward feed mode, in which the wire is fed always ahead of the arc, is necessary to guarantee consistency of bead geometry (Martina, 2010). When depositing multi-dimensional parts, this requires further automation in order to rotate the wire feeder according to the direction of deposition. Furthermore, in-house research showed the occurrence of humping at the beginning, and sloping at the end of the deposition, which are related to heat extraction dynamics. The problem may be overcome by alternating deposition direction, i.e. by starting a new layer where the previous ended.

Recently investigated in the Welding Engineering and Laser Processing Centre, Cranfield University, Plasma Wire Deposition (PWD) (Martina, 2010), based on

PAW, is another version of WAAM: the power source and welding torch are dedicated to the PAW process, while the rest of the setup is identical (Figure 1.19a). An aerospace component manufactured by PWD is shown in Figure 1.19b.

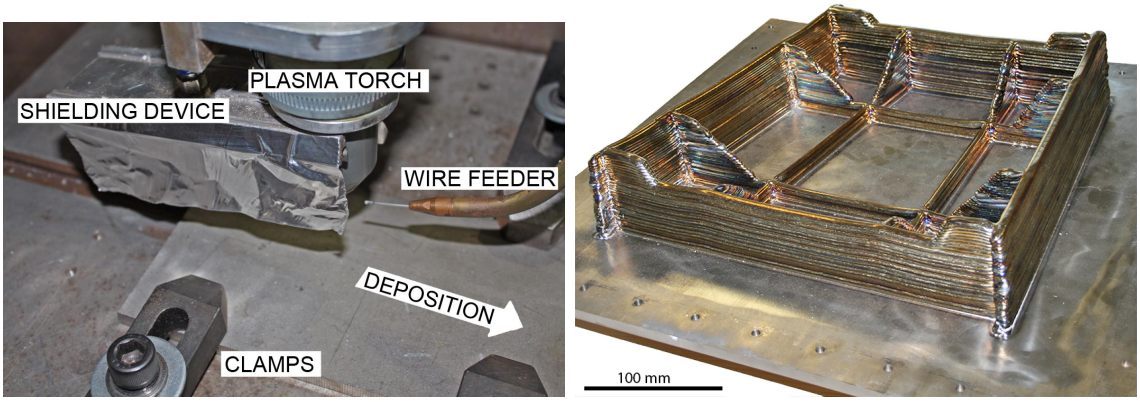

(a) (b)

Figure 1.19: PWD (a) setup (Martina, 2010) and (b) manufactured parts (courtesy Cranfield University).

Unfortunately, in terms of material characteristics the advantages of PWD have not been proved. The Cranfield research has found that AM repeated heat treatments prevent microstructure from being fine grained, and appears similar to that with TIG. Higher power related to constricted arc might be expected to enable much higher deposition rates; however in practice higher heat inputs create molten pool instability and distortion. Furthermore, orifice geometry affects plasma gas flow, and bead geometry; therefore, PWD is thought unlikely to be easily transferred from one platform to another, and the deposit geometry may depend on the design of the torch. Finally, the plasma flow rate could have an effect on bead geometry, adding an undesirable element of complexity to process understanding and development. However, PWD has elements of robustness which should make it the process of choice, as it differs from TIG in that the electrode is not exposed, consequently electrode contamination is not so severe; the torch-to-workpiece distance is also much higher (8 mm for PWD, 3.5 mm for TIG[4]) which should make the process less

[4]Data from an internal report from Cranfield University

sensitive to distance variation.

MIG, particularly in its Cold Metal Transfer (CMT) variant is gaining popularity for WAAM. According to Almeida and Williams (2010) this process is based on controlled dip transfer mode. From a practical point of view, its main advantage is that the wire is the consumable electrode, therefore an external wire feeding system is not required and the setup is generally more compact. This results in easier programming because there is no need to rotate the torch. While traditional MIG is affected by spatter and unstable process behaviour, CMT is characterised by improved quality, lower heat input and negligible spatter (Almeida and Williams, 2010). Like other MIG processes, wire feeding is electronically controlled, and wire feed speed is coupled with current, which simplifies process control. Finally, metal deposition on the substrate/previous layer occurs by surface tension, delivering a smooth profile and little spatter. Although CMT is one of the newest processes, as shown in Figure 1.20 complex features such as horizontal (Figure 1.20a) and inclined walls (Figure 1.20b) can be made. Disadvantages of the technique include arc wandering (Shinn et al., 2005) which reduce the deposition efficiency. Nevertheless, for deposition of steel and aluminium, CMT based WAAM seems the process of choice.

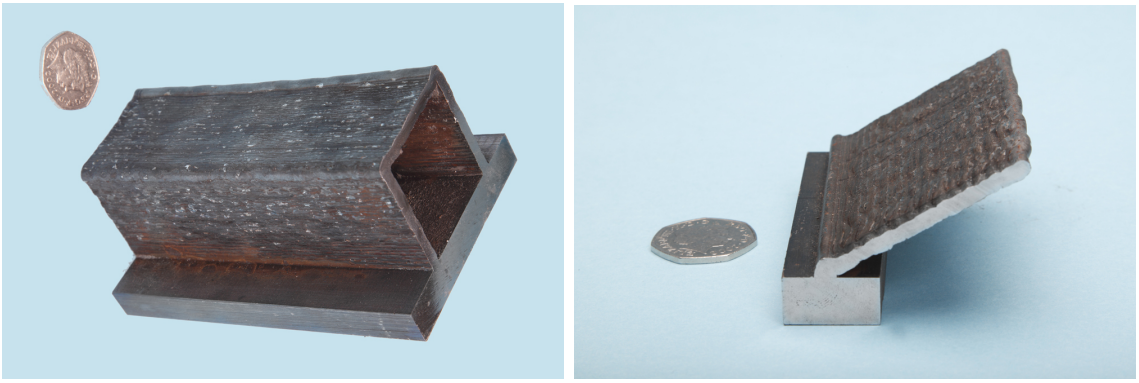

(a) Horizontal wall (b) Inclined wall

Figure 1.20: Example of current geometric capabilities of CMT deposition.

1.3.2 Comparison of techniques

All metal AM processes are summarised in Figure 1.21.

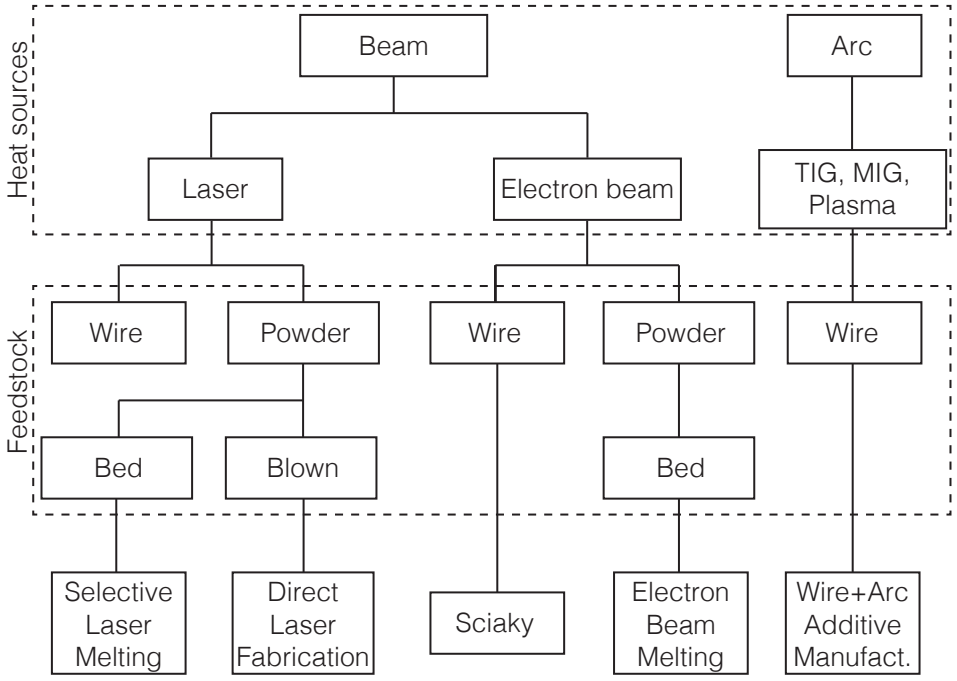

Figure 1.21: Summary of metal AM processes.

As input provided by power sources, and features of fed material limit their capabilities, each of the previously described processes is most suitable to particular applications. As shown in Figure 1.22, arc-based techniques are the ideal complement to beam-based systems, as the former are incapable of manufacturing small size features, a task in which on the contrary the latter perform the best. On the other hand, it is currently impossible to build large components by SLM, as a controlled atmosphere is required in order to prevent oxidation and powder contamination. The present technology is capable of building parts up to $350\times300\times200\text{mm}^3$ (Buijs, 2011). By using DLF it is ideally possible to build large components; however, as the inert atmosphere is generated into a bag or rigid chamber, in reality part size is limited and building large parts is unpractical.

In arc-based techniques, local shielding devices can be used; consequently there is theoretically no limitation on the size of manufactured parts, as a controlled,

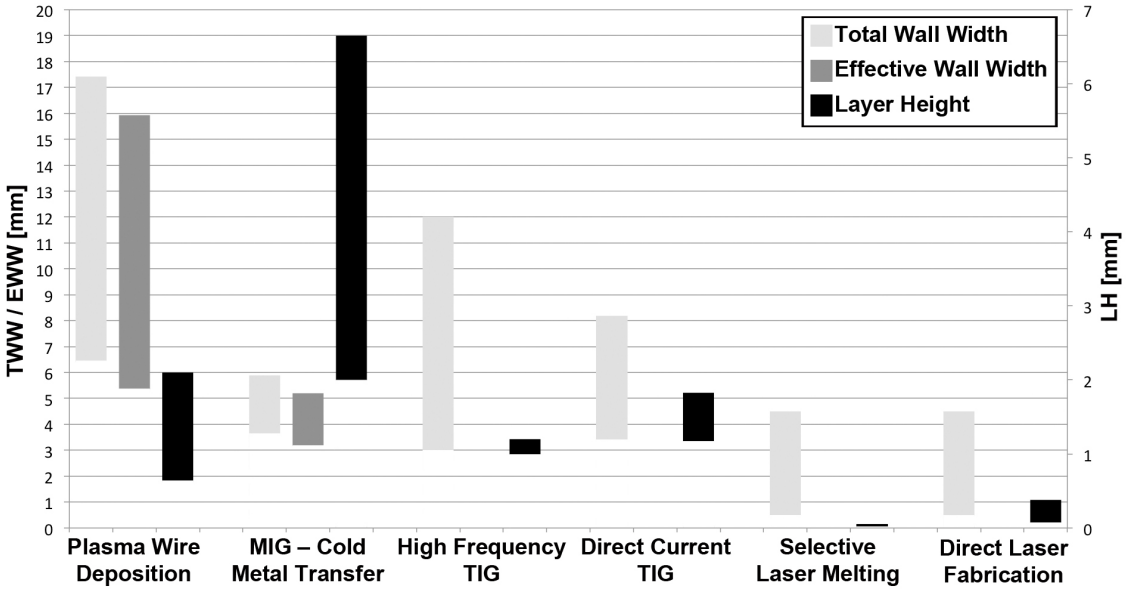

Figure 1.22: Comparison of AM techniques capabilities. Total wall widths (the width of the as-deposited material) of selective laser melting and direct laser fabrication are assumed equal to the laser spot size. Consequently, data on the effective wall width (the width which is effectively usable) is not available for these two processes.

sealed environment is no longer necessary. In fact, in the Welding Engineering and Laser Processing Centre, Cranfield University, a Ti–6Al–4V metre long, 200 mm high wall (Figure 1.23) has been built successfully (Almeida and Williams, 2010) in open atmosphere using local shielding. A part built in an argon-filled tent is shown in Figure 1.24 (baesystems.com, 2014).

High heat input of WAAM compared to SLM, DLF, EBM enables higher deposition rates, up to more than $2.5\,\mathrm{kg\,h^{-1}}$. Table 1.2 gives a summary of reported deposition rates for a variety of techniques. For instance, a $80\times45\times70$ mm^3 insert requires 25 h to be manufactured by SLM[5] (Buijs, 2011), while the same component, if made by CMT, could take less than 1 h. According to Sciaky (2014b), their system is capable of depositing up to $10\,\mathrm{kg\,h^{-1}}$, but a BTF ratio of more than 10 makes their process less attractive from an economical point of view. Furthermore Sciaky (2014b) requirement for a soft vacuum results in expensive equipment and reduces

[5]Plus 8 hours for finishing and polishing. Deposition time exclusively is considered in this comparison.

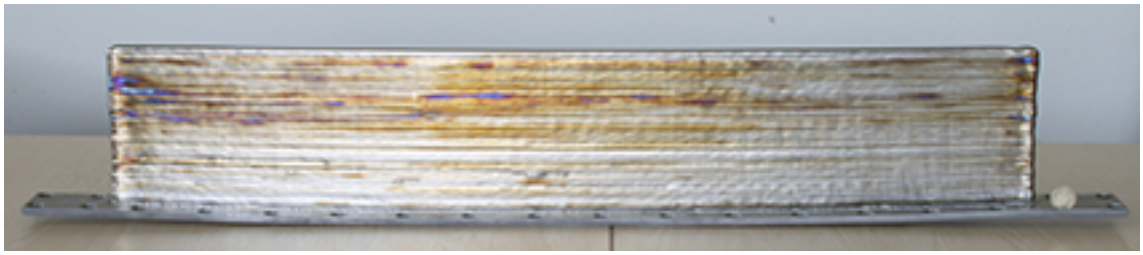

Figure 1.23: Metre long Ti–6Al–4V wall recently manufactured in Cranfield University (Almeida and Williams, 2010).

(a) Top view

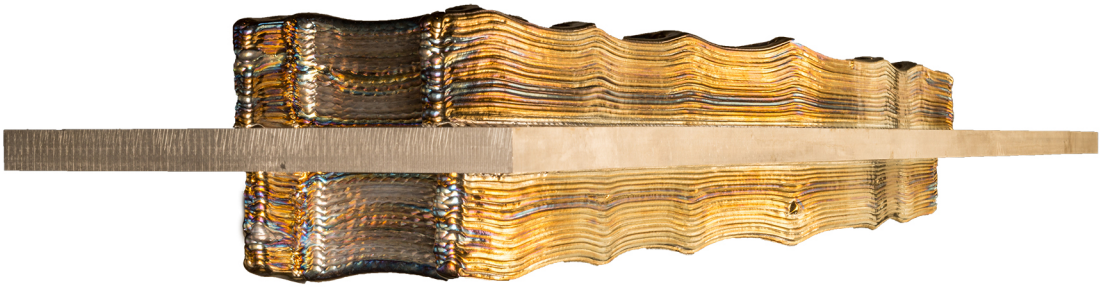

(b) Side view. Please note two components were built back-to-back sharing the same sacrificial substrate

Figure 1.24: 1.2 m Ti–6Al–4V wing spar built by WAAM at Cranfield University. The structure is not a real component however it is representative of an F35 fighter jet wing spar. From baesystems.com (2014).

the likelihood of effective heat management.

Table 1.2: Deposition rates of AM techniques.

Technique	**Deposition Rate** ($kg\,h^{-1}$)	**Reference**
DLF	0.9 to 4.5	Arcella and Froes (2002)
SLM	0.060 to 0.120	Zhang et al. (2003)
Sciaky	10	Sciaky (2014b)
TIG WAAM	1.5	Internal report from Cranfield University
PWD WAAM	1.8	Martina (2010)
CMT WAAM	2.6	Almeida and Williams (2010)

As the subject of the present work is the development of large scale additive manufacturing in an economically viable way, arc-based techniques will be those investigated in the following section.

1.3.3 Deposition of Ti–6Al–4V

Ti–6Al–4V is possibly the alloy that raises the greatest interest in the AM community: Ti–6Al–4V is widely employed in the aerospace industry; moreover, due to the high cost and waste related to the current manufacturing processes, it is beneficial to develop and use techniques that enable a substantial reduction in both cost and waste.

Ti–6Al–4V deposition with both beam and arc-based techniques has been already investigated to different extents, and each technique has required almost a distinct approach. For instance, in the case of SLM a geometric model, a set of equations which predict some metrics, such as Total Wall Width (TWW)[6], Effective Wall Width (EWW)[7] and Layer Height (LH)[8], is not necessary. In fact, multiple passes, one alongside the other, are sufficient to achieve a specific width, given the knowledge of a single pass width. Layer height is determined by powder size distribution.

[6]The width of the as-deposited material
[7]The width which is effectively usable
[8]The height of each layer

In the case of the techniques in which powder or wire are fed directly into the molten pool, as the quantity of powder and/or wire can be varied quite flexibly, knowing exactly how to set the process parameters is necessary. Hence, Almeida and Williams (2010), Martina (2010) focused on a systematic process analysis which led to the development of a reliable geometric model for CMT and PWD, respectively. The main difference in their work regards the selection of the independent variables. While Almeida and Williams (2010) selected wire diameter, Wire Feed Speed (WFS) and WFS/Travel Speed (TS) ratio (the latter to ensure constant material deposition per unit length), Martina (2010) chose WFS, TS and Current as in PWD these three parameters can be set up independently. Consequently for both these processes it is now possible to predict a series of responses, i.e. TWW, EWW, LH and Deposition Efficiency (DE)[9] from the input data.

The approach adopted by Almeida and Williams (2010), Martina (2010) is quite different to that of Heralić et al. (2010, 2008), who developed an on-line control system that adjusts continuously some process parameters to attain good deposition quality. While targeting consistent and robust deposition, this flexible approach of continuous adjustment does not consider process capabilities, i.e. minimum and maximum values of the various geometric features were not investigated.

Most authors, except for Almeida and Williams (2010), Martina (2010), focused on depositing in a bag filled with inert gas, such as argon, to guarantee sufficient protection from oxidation and attain acceptable mechanical properties.

In terms of microstructure, components made by arc-based techniques are characterised by a Widmanstätten structure within large, columnar prior β grains (Almeida and Williams, 2010, Baufeld et al., 2009). The size of the α lamellae varies according to the Z coordinate (building direction), within the same specimen. According to these authors, it is common to find smaller lamellae in the first layers, larger ones towards the middle and then small ones again towards the top, where martensite is

[9]The ratio between the cross-sectional area of the effectively usable material to the total cross-sectional area

present (Figure 1.25). This is likely to be due to the repeated heat treatments that a generic point undergoes, and to the different cooling rates that exist in different Z coordinates (Baufeld et al., 2011, 2009). In the bottom, the substrate can act as heat sink and is responsible for cooling rates high enough to produce even some martensite. In the middle, lamellae growth is continuously stimulated by the heat treatment induced by the deposition of a new layer, while in the top convection cooling produces finer lamellae, whose growth is not stimulated as no other layer is deposited (Martina, 2010).

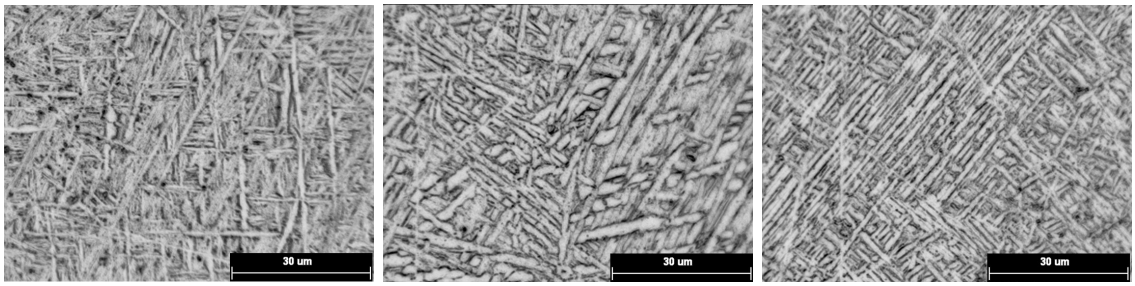

(a) Top layers (b) Middle layers (c) Base layers

Figure 1.25: Variation in α lamellae size across the sample from WAAM manufacture (Martina, 2010).

Banding is a phenomenon reported by many authors (Baufeld et al., 2011, Martina, 2010, Wang et al., 2011); it consists of a series of bands parallel to the substrate work piece (Figure 1.26). A band is predicted with each deposited layer. The first layer to appear is well below the molten region associated with the top layer. Baufeld et al. (2011), Martina (2010) suggest that the absence of bands in the top layers is due to the heat treatment induced by the deposition of the subsequent layers. In fact, it stands to reason that during the deposition of a layer a certain amount of material is brought above the β-transus temperature. According to some authors (Kelly and Kampe, 2004a,b, Martina, 2010), bands coincide not with the liquidus line but with the β-transus.

Baufeld et al. (2011) compared the microstructure of specimens made by DLF and WAAM; in both cases 1.2 mm diameter wire was fed. The authors do not

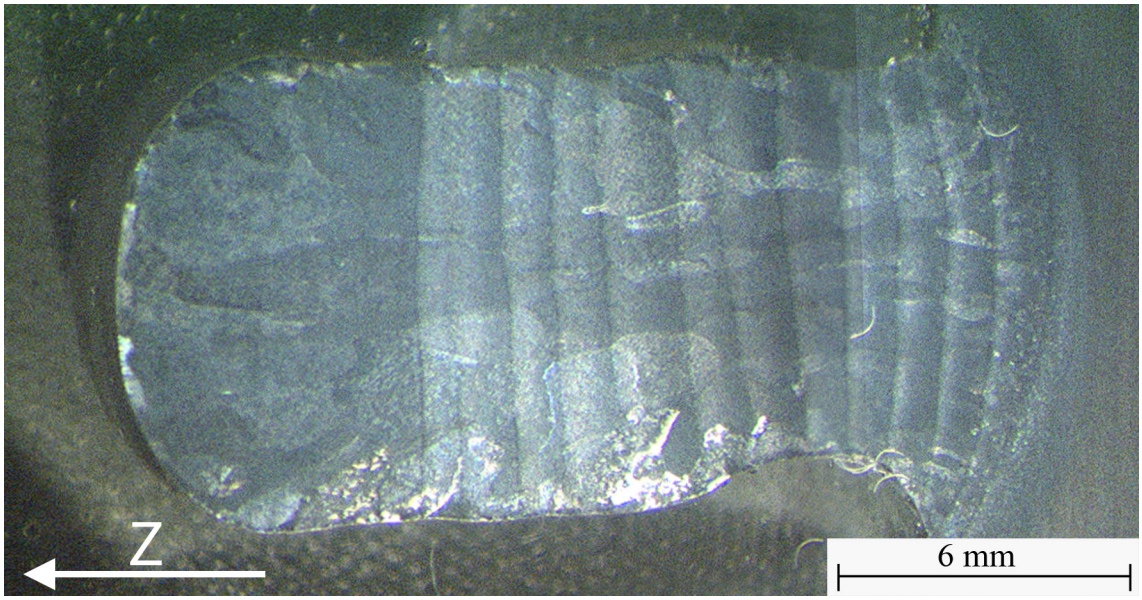

Figure 1.26: Banding in AM components (Martina, 2010). Z is the direction of the deposition; the left hand side of the picture corresponds to the last layers and does not show any banding.

provide any precise figure regarding the size of prior β grains for the two processes, only stating that in DLF specimens they are smaller than in WAAM ones. The α lamellae width in the middle of the deposit was smaller with DLF than WAAM. For both processes, the authors confirmed that in the bottom area smaller α lamellae can be found, and the presence of martensite is suggested. An average measure of α lamellae in the top region is 0.6 µm for both processes.

1.3.3.1 Solidification and texture development in AM

During the deposition of the first layer on the starting substrate (which has an equiaxed or bi-modal microstructure), depending upon the temperature reached the material below the liquidus front either transforms fully to β phase, or it undergoes coarsening of the α phase. In general, coarsening of the β grains occurs too (Wang et al., 2013). New prior β columnar grains develops from the substrate by heterogeneous nucleation. The grains that grow are those with a preferential orientation, which is the one aligned with the solidification front of the molten pool (Wang et al., 2013). If the constitutional supercooling is insufficient, there is no nucleation of new

β grains, and the already existing ones continue their growth following the thermal gradient. According to Wang et al. (2013), the flat base of the molten pool results in grains that are orientated in the <001> direction.

During deposition of new layers, the competitive growth still favours the <001> BCC grains and a strong <001> texture develops throughout the deposited material (Antonysamy, 2012). These grains often traverse the whole height of the component (Wang et al., 2013).

According to Al-Bermani et al. (2010), in EBM components such texture can be as high as 10 $\times$ random. Al-Bermani (2012) showed that also cube and 45° rotated cube components exists, which were associated to the EBM scanning path. Similar behaviour was also seen by Antonysamy (2012) in WAAM components, where the prior β grains were slightly tilted towards the direction of the torch motion.

1.3.3.2 Defects and inhomogeneity

With regards to Ti–6Al–4V, WAAM's defects include porosity, cavities, microstructural inhomogeneities, residual stress and distortion. Porosity can occur due to poor handling of the wire; Wang et al. (2013) demonstrated that by touching the wire with bare hands, introducing porosity deliberately was possible. Martina (2010) observed cavities in PWD WAAM specimens; these were produced by lack of keyhole closure related to wrong deposition parameters. Antonysamy (2012), Baufeld et al. (2009), Wang et al. (2013, 2011) observed epitaxial grain growth with extremely textured α and β phases leading to strongly anisotropic mechanical properties. Finally Almeida and Williams (2010), Ding et al. (2011) reported distortion in WAAM components related to residual stresses, which were particularly significant in the longitudinal direction. The use of Hot Isostatic Pressing (HIP) proved to be effective in reducing the microstructural inhomogeneities by transforming the martensite in Widmanstätten thus increasing ductility; furthermore HIP resulted in pores closure and reduction of distortion, when performed on unclamped structures (Qiu et al., 2015).

1.4 Residual stresses

According to Withers and Bhadeshia (2001a), "residual stresses are those which are not necessary to maintain equilibrium between the body and its environment"; they state that often unexpected failure is caused by the joint effect of residual and service stresses. The same authors (Withers and Bhadeshia, 2001a) explain that residual stresses can be distinguished by what caused them, by their scale, or by the method used to measure them. In fact, residual stresses can occur because of misfits affecting a different location of the same part or considered system, or due to thermal gradients such as those experienced during welding, where the material shrinks during solidification and cooling to room temperature (Withers and Bhadeshia, 2001a). Residual stresses are manifested in component distortion, which might prevent industrial application (Wen et al., 2010).

Withers and Bhadeshia (2001b) stated that from a magnitude point of view, residual stresses of a macroscopic scale are defined as type I, while those changing over the size of a grain are type II. Finally, stresses varying over the microscopic scale, down to the size of a single atom, are type III. In the case of polyphase material, type I stresses can affect the whole component, while type II and III are limited to one phase and are not continuous across them (Withers and Bhadeshia, 2001a). Type I stresses are typical in engineering components, in which the misfits can be generated during the assembly process or because of chemical or thermal interactions (Withers and Bhadeshia, 2001b). Riveting, in which plates are subject to stress by the rivet, is a typical example of mechanically induced type I residual stresses (Withers and Bhadeshia, 2001b).

Residual stresses can be induced on purpose in order to improve the performance of the component. For example, rapid cooling of glass surface can be used to generate a thermal misfit, which results in compressive residual stress (roughly 100 MPa) on the external surface and tensile residual stress in the internal region (Withers and Bhadeshia, 2001b), a configuration which results in improved strength. Similarly,

shot peening (Černy, 2012, Dalaei et al., 2011), which consists of bombarding the part with small particles, is used to generate compressive residual stress. According to Dalaei et al. (2011) this technique proved to be successful in improving fatigue properties, because the treated surface of a part is more resistant to crack initiation, and fatigue crack growth rate is also reduced. However, the same authors noted how a high surface roughness could be detrimental to fatigue properties. Residual stresses can relax during the component life cycle depending upon microstructure, tensile properties, peening state, and stress conditions (Dalaei et al., 2011). Withers and Bhadeshia (2001b) explained how, in practice, potential failures can be minimised by yielding the component in the same direction of the predicted load (the one the component will experience during service), and they also explained how the greatest benefit is achieved in low amplitude, high cycle fatigue, while the smallest benefits are in large strain, low cycle fatigue (Withers and Bhadeshia, 2001a).

Laser Shock Peening (LSP) consists in introducing plastic deformation by a laser induced shock wave (Cuellar et al., 2012). According to Hu and Grandhi (2012) by using a high power density on a sacrificial coating which vaporises and produces plasma; and a transparent dielectric overlay such as water, that confines the vapour and plasma; a high amplitude pressure is generated which is higher than the material's yield strength. Consequently the material is left with compressive residual stress, which proves to increase components fatigue life (Ganesh et al., 2014, Zhou et al., 2014).

In order to mitigate unwanted residual stresses, various methods have been investigated. Ultrasonic Impact Treatment (UIT) is the combination of ultrasonic waves with mechanical impact by means of an ultrasonic transducer. Gao et al. (2014) showed that when applied to the toes of a six pass weld UIT was effective in reducing the tensile stress, especially close to the centreline of the weld.

Thermal tensioning, according to Withers (2013), is based on temperature control, either via cooling or heating locally during or after welding; it can be *transient*,

if the tool moves with the welding torch; or *steady state*, if the component is heated or cooled globally. Regardless, the thermal expansion can prevent or counteract the formation of residual stresses. This method is particularly suitable for plates.

Global Mechanical Tensioning (GMT), according to Price et al. (2007), Richards et al. (2008) consists in tensile loading of the weld; it could be done either during the welding process (*in situ* GMT) or after (*post weld* GMT). These techniques are successful with linear welds or simple geometries, and the equipment is large and heavy (Altenkirch et al., 2009). If the load is applied only to a small region around the welding tool, mechanical tensioning is defined as *local*; one of the local tensioning techniques is rolling (Coules et al., 2012b). Rolling has the potential to overcome some of the impracticalities of GMT (Altenkirch et al., 2009, Kurkin and Anufriev, 1984, Wen et al., 2010, 2009). Rolling of AM parts to control microstructure and mechanical properties is potentially an exciting area and has been chosen as the subject of the present research, thus it will be discussed thoroughly in the following section.

1.4.1 Rolling of welds

One of the way of mitigating residual stresses is rolling, in which a load is applied with a moving roller, as shown in Figure 1.27. If the load is sufficient to compress plasticly the bead in the normal direction, a plastic elongation will occur then in the rolling direction, thus decreasing the longitudinal residual stresses (Altenkirch et al., 2009).

Kurkin and Anufriev (1984) demonstrated the feasibility of *in situ* rolling (Figure 1.27a), in which the roller, trailing the torch, applies the load while the material is still hot. They assumed rolling hot material would have been more beneficial than cold rolling, due to the high temperature which would have aided the deformation. In fact, in the case of the investigated material (Amg6 and 1201 aluminium alloys) they showed that not only distortion can be eliminated, but residual stresses can

be reduced to 20 MPa. They provided some guidelines as well, such as the working distance between the welding tool and the roller (from 30 mm to 300 mm) and the rolling load (from 2 kN to 50 kN).

In addition to *in situ* rolling, alternatives exist. The load can also be applied directly on the weld bead (Figure 1.27b), or on its sides (Figure 1.27c). Both configurations can be used either when the material is still hot or when it has cooled down to room temperature (Altenkirch et al., 2009). In the same research, Altenkirch et al. (2009) experimented that modelled by Wen et al. (2010), who used finite element analysis to investigate *in situ*, interpass and side rolling of friction stir welds. Unfortunately, Altenkirch et al. (2009) failed to achieve significant reductions in residual stress and it was suggested that this was due to the difficulties in rolling near the friction stir welding tool.

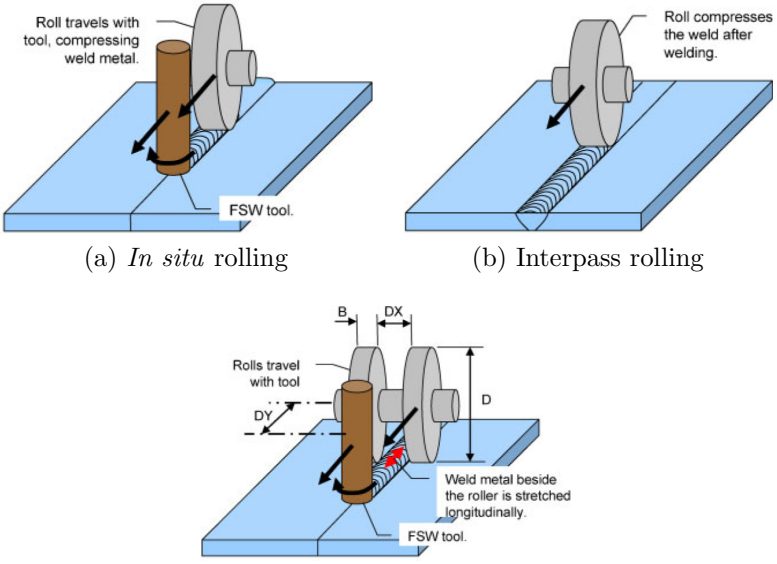

(a) *In situ* rolling (b) Interpass rolling

(c) Side rolling

Figure 1.27: Different rolling setups (Wen et al., 2010). The welding process in the figures is friction stir welding, but rolling can be applied to other welding processes equivalently.

Interpass rolling proved to be effective in reducing both distortion and residual stresses (Altenkirch et al., 2009). Angular and bending distortions were significantly reduced and the tensile stresses were changed into compressive ones (Figure 1.28).

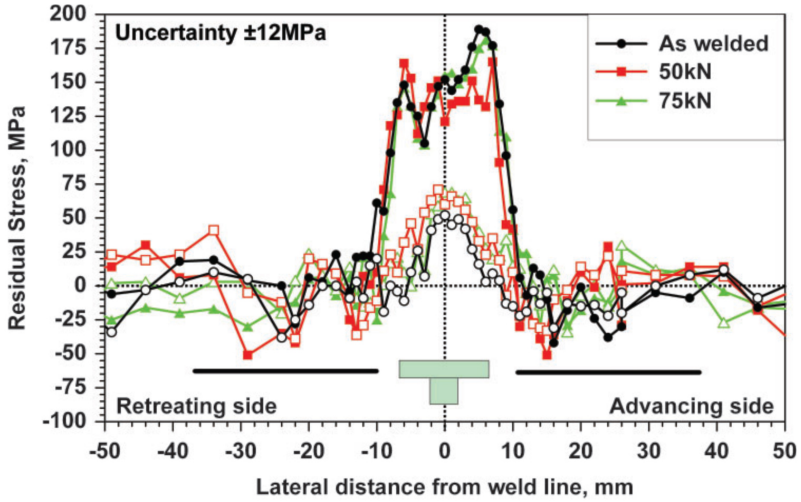

(a) Results of side rolling of AA 2024-T3 alloy. Solid markers represents longitudinal residual stress and open markers transverse one.

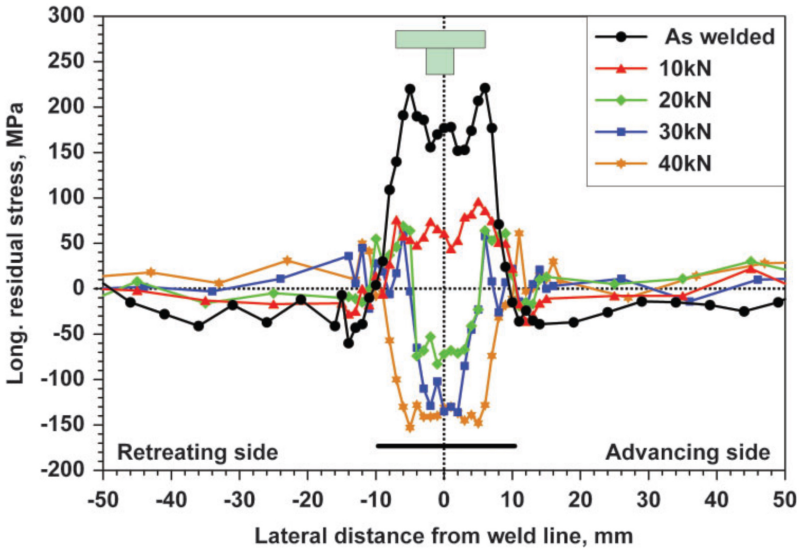

(b) Interpass rolling of AA 2198-T8 alloy

Figure 1.28: Side and interpass rolling results for AA 2024-T3 and AA 2198-T8 alloys (Altenkirch et al., 2009).

Wen et al. (2009) applied rolling to a large friction stir welded component, specifically an integrally stiffened panel whose total length was 3.7 m. In their finite element model, after the friction stir welding process, the panel was characterised by a bowing distortion of about 10 mm; after the rolling pass (set at 1% reduction), the panel was practically flat, the bowing distortion being less than 1 mm.

1.4.2 Rolling of additive manufacture parts

AM components, due to the multiple thermal cycles they undergo during the manufacturing process, are affected by residual stress and distortion (Abe et al., 2001, Akula and Karunakaran, 2006, Anca et al., 2010, Baufeld et al., 2011, Charles and Järvstråt, 2009, Kruth et al., 2007, Levy et al., 2003, Song and Park, 2006, Yan et al., 2009, Zäh and Branner, 2010). Colegrove et al. (2013) demonstrated the feasibility of rolling of WAAM structures and investigated the effect of rolling on the geometry (including surface waviness and deposition efficiency) and on the distortion of G3Si1/ER70S-6 steel walls on S355 HSLA steel baseplates. Moreover, they measured the changes in the microstructure. The investigated loads were 25 kN, 50 kN and 75 kN, while the deposition process was standard MIG; also, they evaluated the differences between interpass rolling (every layer and every four layers) and *in situ* rolling. Furthermore they tested two different roller designs, a profiled one and one with a much deeper groove (named slotted roller).

Colegrove et al. (2013) showed an as-deposited distortion of 5 mm at the midpoint, which increased to 6.5 mm when rolling *in situ* at 25 kN but decreased to 0.4 mm when using a slotted roller at 50 kN. In general, with increasing load there is a reduction in distortion. In terms of surface waviness, once again the best result was achieved with the slotted roller at 50 kN. Interpass rolling, when done every four layers, did not give any particular benefit compared to the as-deposited specimen. The deposition efficiency was maximised when using the slotted roller (97%), and was over 20% better than the as-deposited efficiency (75%).

As for specimens' microstructure, there was a strong reduction in grain size, which was as small as 4.5 µm. According to Colegrove et al. (2013) potentially the deformation resulted in nucleation of more austenite grains which in turn produced a finer transformed microstructure.

1.5 Summary

AM is moving quickly towards a level of maturity which should soon make it suitable for full industrial application. Its advantages in terms of cost reduction, lead time reduction and increased design freedom are evident. Companies are now investing heavily into research on the process to acquire the required data that will enable the qualification of the technique.

Amongst the range of materials that can be processed by AM, titanium is possibly the focus of research in the field, due to the extremely high costs associated with its production and processing by conventional methods. In particular, in the aerospace sector this alloy has been adopted for a growing number of large structural components, affected by BTF ratios and lead times. These structures have the potential for the largest cost benefits associated with the implementation of AM.

The main challenges to process implementations are:

- control of geometry;
- microstructure;
- mechanical properties;
- shielding;
- residual stress and distortion.

1.5.1 Control of geometry and process model

The deposition processes most suited to the AM of large structures are mainly arc-based; unfortunately there aren't commercial systems currently available. To

enable automation it is necessary to know how the process parameters affect the deposit geometry. While efforts have been made to monitor the quality of the bead during deposition to ensure the absence of defects, a systematic characterisation of process behaviour has not been undertaken so far. In particular, to minimise the BTF ratio parameters such as wire feed speed, arc current, travel speed, can be varied to produce deposits with different geometrical characteristics, to match that required in part design. This is especially meaningful with regards to the width of the deposit: an excess of material results in undesirable waste which has to be machined away, and therefore is to be avoided. Consequently it is of paramount importance to study the effect of such parameters and develop a mathematical model to predict their effect upon geometry; such a model enables the selection of the most appropriate parameter combination on a case-by-case basis to minimise waste, maximise productivity and enable automation. Ultimately, this set of process equations is required for the development of Computer-Aided Manufacturing (CAM) software.

1.5.2 Microstructure and mechanical properties of titanium

AM is essentially a micro-casting process, which results in long columnar grains that are highly textured when applied to titanium. This results in strongly anisotropic mechanical properties, with superior elongation in the vertical direction, and higher strength in the horizontal one[10]. The repeated thermal cycles induced by the deposition of each layer cause local variations of the microstructure, with inconsistent α lamellae size. These features are undesirable from a design point of view and may limit the implementation of AM.

High-pressure rolling, when applied to steel AM, produced a refined microstructure. Therefore, it is necessary to determine whether similar improvements can be achieved in Ti–6Al–4V.

[10]If the layers are deposited horizontally

1.5.3 Oxygen levels and shielding requirements

Another problem is related to the required O_2 level within the surrounding atmosphere for production of parts with the desired mechanical properties. Ti–6Al–4V wire contains oxygen as alloying element due to its capacity to act as α phase stabiliser, thus enhancing strength. However, too high concentrations lead to embrittlement, therefore the general approach is to keep the O_2 levels in the deposition atmosphere as low as possible which may not be necessary. Less stringent constraints on O_2 levels could result in cheaper equipment and faster processing times. Higher tolerances could also facilitate the adoption of local shielding devices, as opposed to enclosures. Therefore, it is necessary to understand how the O_2 levels in the deposition environment affect the O_2 contamination of the final part.

1.5.4 Residual stress and distortion

Similar to welded components, AM parts are also affected by residual stresses and distortion. These are possibly the two greatest causes of concern when considering whether the process can be implemented.

A variety of methods has been investigated to mitigate residual stress and distortion. Amongst them, high-pressure rolling seems to be the one with the highest potential, due to its ease of implementation, and limited cost. Furthermore, it has already been tested for welding applications with success. Its feasibility on AM structures was proved on initial steel trials; however, the technique has never been applied to titanium deposits. Therefore its effect on residual stress, geometry, distortion and mechanical properties needs to be determined.

1.6 Research questions

The research questions can be formulated as the following:

- Is it possible to identify a relationship between part geometry and process

parameters during TIG WAAM?

- Does rolling address the critical issue of strong anisotropic properties due to the columnar prior β grains produced by WAAM of Ti–6Al–4V?
- Does rolling of titanium WAAM parts improve the mechanical properties?
- What is the relationship between the O_2 levels present in the atmosphere during deposition and the O_2 levels in the final part?
- Does rolling reduce residual stress and distortion in Ti–6Al–4V WAAM components?

1.7 Aim & objectives

The aim of the research project is to develop large scale Ti–6Al–4V WAAM by producing components with acceptable structural integrity and homogeneity, from the geometrical, microstructural, mechanical and residual stress points of view. The research questions are related to the fundamental issues shown in Figure 1.29.

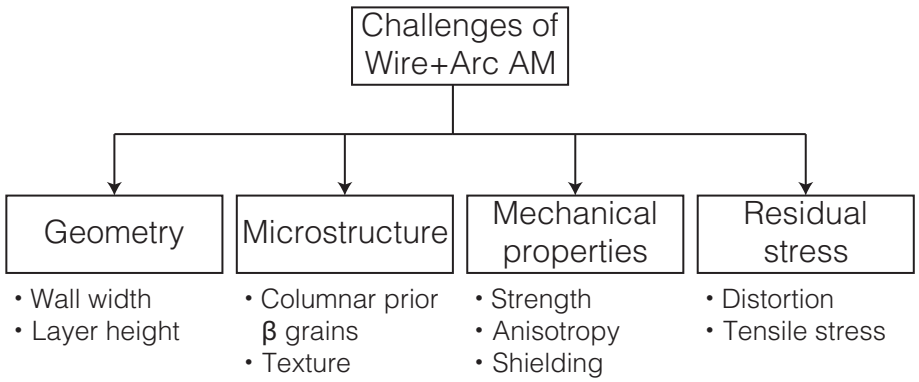

Figure 1.29: Project map with the areas that will be investigated in the research work.

The objectives are the following:

- to identify the relationships between process parameters and Ti–6Al–4V deposits geometry (chapter 2);
- to study the effect of high-pressure rolling on the microstructure of Ti–6Al–4V WAAM components (chapter 3);

- to assess the effect of high-pressure rolling on the mechanical properties of Ti–6Al–4V WAAM components, also with regards to the relationship between the observed microstructure and the mechanical properties (chapter 4);
- to investigate the effect of O_2 in the deposition atmosphere on mechanical properties (chapter 4);
- to evaluate changes in the deposits geometry, distortion and residual stress produced by high-pressure rolling (chapter 5).

Chapter 2

Empirical modelling of TIG-based WAAM

This Chapter contains material from the following articles:

Martina, F., Menhen, J., Williams, S.W., Colegrove, P.A., Wang, F. 2012. Investigation of the benefits of plasma deposition for the additive layer manufacture of Ti–6Al–4V. Journal of Materials Processing Tech. 212, 1377–1386.

Martina, F., Williams, S., Colegrove, P.A., 2013. Design of an empirical process model and algorithm for the tungsten inert gas wire+arc additive manufacture of Ti–6Al–4V components, in: 24th International Solid Freeform Fabrication Symposium, Austin, Texas, USA. pp. 697–707.

2.1 Context

Controlling Wire+Arc Additive Manufacturing (WAAM) geometry in an automatic fashion is not possible yet. Differently from beam-based processes, whose transition from computer drawing to machine code can be considered automatic, WAAM still requires a labour-intensive process of parameters investigation and selection. These depend on the different geometrical features present in the parts. Through numerous iterations, parameter combinations which provide the requested deposit width can be found. A flexible way of controlling the geometry is desirable to automate the

process and to minimise material waste, and it is the objective of this chapter.

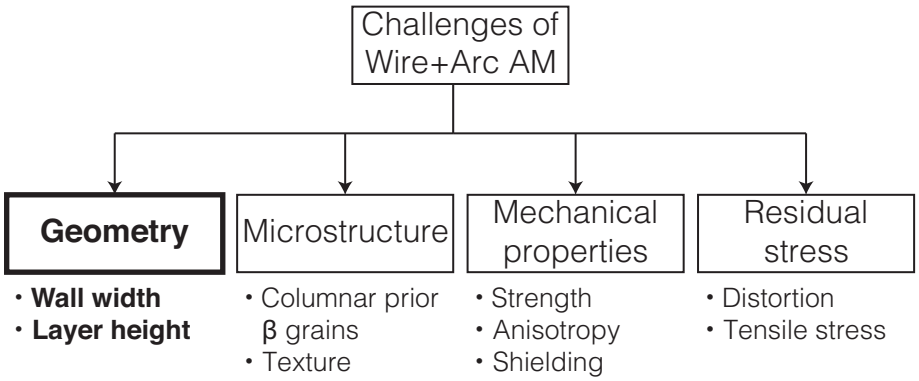

Figure 2.1: Project map. In bold the work package object of the present chapter.

2.2 Introduction

Some problems are preventing Additive Manufacturing (AM) from being implemented in a real industrial environment; the inability to relate process parameters to part geometry being one of them. Martina (2010) developed some empirical relationships between process parameters and walls geometry for Plasma Wire Deposition (PWD) WAAM by adopting a Design Of Experiment (DOE) approach, similarly to that carried out by Almeida and Williams (2010) for Cold Metal Transfer (CMT) WAAM.

For Tungsten Inert Gas (TIG) WAAM, so far it has been impossible to select parameter values on the basis of, for example, the desired part thickness, or layer height. Actually, without great knowledge and expertise, one would not know how thick the layers extracted from the Computer-Aided Design (CAD) drawing should be. Moreover, without prior knowledge of the process, unfeasible parameter combinations could be selected.

This chapter addresses the feasibility issues for TIG WAAM by determining a working envelope for the process. In the preliminary experiments, by considering upper and lower limits for each of the process parameters, as well as testing all their possible combinations, a set of constraints was developed. The constraints separate

the feasible and stable region of parameters combinations which delivers a part of acceptable quality, from the region which does not.

In order to evaluate the geometric characteristics of the parts built by WAAM, a series of metrics was defined, the aim being to compare different parameter combinations in a systematic and analytical way, enabling the possibility of ranking them objectively. The metrics studied are Wall Widths (WWs) and Layer Heights (LHs).

The defined metrics are considered as responses in a DOE, which produced a set of equations that relate the process parameters to geometrical features. Ultimately, the equations should give the capability of predicting characteristics such as LH or WW, for a given set of process parameters, and vice versa, while ensuring an acceptable quality of the deposition.

Finally, a case study that shows how the equations might be used to manufacture a component is provided.

2.3 Experimental procedures

The equipment used for the preliminary and process model experiments were different and are presented in sections 2.3.1 and 2.3.2, respectively. Regardless of the experiments, the TIG torch was mounted on an ABB 6-axis robot. A 100 mm long trailing shield was used to minimise oxidation. Argon gas was used for both the process and the trailing shielding gases. The wire was fed from the front of the welding pool and its chemical composition is shown in Table 2.1. A schematic diagram of the setup is shown in Figure 2.2.

Table 2.1: Chemical composition of Ti–6Al–4V wire used in the experiments.

Ti	Al	V	Fe	O	C	N	H	TOE	Y	Others
89.397	6.14	3.96	0.18	0.14	0.02	0.011	0.001	<0.1	<0.001	<0.05

To reduce the number of independent variables investigated, and therefore the complexity of the experiment, some factors were kept at the same level throughout

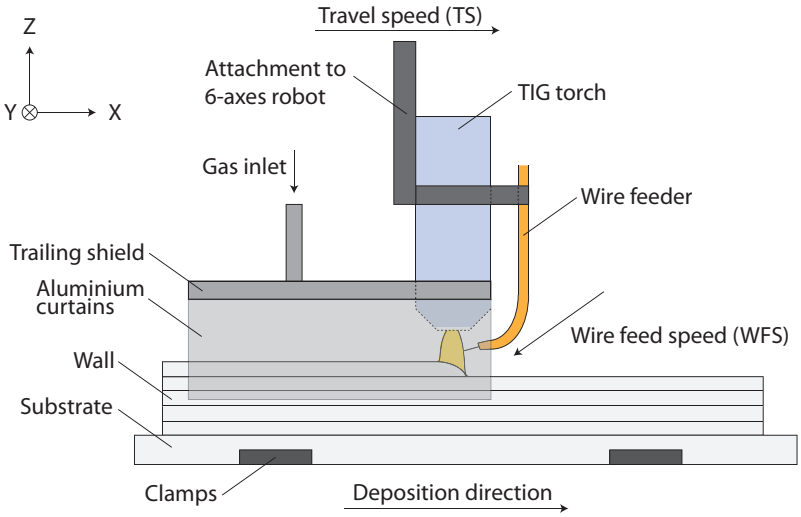

Figure 2.2: Schematic of experimental setup.

the research. These were:

- Electrode-to-workpiece distance = 3.5 mm;
- Tungsten electrode tip angle = 30°;
- Wire diameter = 1.2 mm;
- Gas flows (Table 2.2);
- Pulsed DC current parameters:
  - $I_p/I_b = 1.5$
  - Pulses duration = 0.05 s
  - Frequency = 10 Hz

where in the pulsed waveform I_p is the peak current and I_b is the base current.

Table 2.2: Deposition stages: gas flow rate, and durations.

	Pre purge	**Slope up**	**Deposition**	**Slope down**	**Post purge**
Process gas flow rate ($l\,min^{-1}$)	9	9	9	9	9
Trailing shield gas flow rate ($l\,min^{-1}$)	20	20	20	20	20
Duration (s)	10	0.1	42 to 125 [a]	0.1	20

[a]Duration depended on TS

The I_p/I_b ratio of 1.5 was chosen after some preliminary experiments. On the one

hand, they showed that for low ratios the benefits of pulsing was minimal. On the other hand, for high ratios (>1.8) the background current was low, which resulted in a lower maximum Wire Feed Speed (WFS) given the low heat input during the background heating period (see Table 2.3).

Table 2.3: An example of the effect of the I_p/I_b ratio on the maximum achievable WFS.

Travel speed ($mm\,s^{-1}$)	**Average current** (A)	$\mathbf{I_p}$ (A)	$\mathbf{I_b}$ (A)	$\mathbf{I_p/I_b}$ **ratio**	**Max. wire feed speed** ($m\,min^{-1}$)
3	90	70	110	1.57	1.8
3	90	60	120	2.00	1.6

2.3.1 Preliminary experiments for determining process window

The power source used for this experiment was a Migatronic TIG Commander 320A AC–DC and wire feeder was a Migatronic KT-4. A set of 70 preliminary single layer (bead on plate) experiments provided the necessary information for understanding the general behaviour of the process and determining the limitations of the process parameters. In TIG deposition the investigated parameters could be set independently from each other, leading to combinations which are unfeasible due to either physical limits or impractical parameter combinations. While two parameters were kept constant, the other was varied in fixed steps till an unfeasible combination was found on the basis of visual assessment of the deposited layer. This procedure was repeated until all three main parameters were varied separately.

Once the preliminary experiments were performed, each point was plotted on two separate cartesian planes (WFS vs. Current, and WFS vs. TS). Points were marked differently according to their feasibility and separated by lines whose equations were then described. These lines were additional to those representing the minimum and maximum value for each factor.

2.3.2 Experiments for developing a statistical empirical model

For this part an EWM Plasma/Tig power source, and an EWM TIG torch were used. Walls were made of 15 layers and were 250 mm long. Layer deposition always started from the same end. Before starting each wall, the plates were ground to eliminate impurities and improve the surface finish, and degreased with acetone. Six straight walls were built on Ti–6Al–4V plates measuring 330×210×12 mm^3. The part was allowed to cool down to 50 °C before depositing a new layer for consistent part geometry. It was not necessary to wait for the part to cool down to room temperature, as preliminary experiments showed the geometry of a new bead did not change if the temperature of the already deposited part was below 70 °C (please see appendix A on page 165).

After establishing the process constraints, a D-Optimal design method (Montgomery, 2006) was chosen for the experiment. Optimal designs are computer-generated and are particularly suitable when the experimental region is irregular, the model is nonstandard (i.e. the experimenter knows beforehand some interactions will not be significant), and/or there are requirements on the maximum sample size (i.e. a reduced number of runs must be done). A design is D-Optimal if it "minimises the volume of the joint confidence region on the vector of regression coefficients" (Montgomery, 2006). In practice, the experimenter inputs the constraint equations and specifies any conditions related to unnecessary model terms and sample size. The software then runs an algorithm and returns the set of experiments that have the highest D-Optimal efficiency.

After the preliminary experiment and factors reduction, Wire Feed Speed (WFS) $[X_1]$, Travel Speed (TS) $[X_2]$ and Current $[X_3]$ were selected as the factors in the model.

As for the responses, quadratic behaviour was anticipated on the basis of the work

of Martina (2010), so three-factor second-order polynomial functions were fitted:

$$Y = \beta_0 + \sum_{i=1}^{3} \beta_i x_i + \sum_{i<j}^{3} \beta_{ij} x_i x_j + \sum_{i=1}^{3} \beta_{ii} x_i^2 \tag{2.1}$$

where Y is the predicted response, β_0 is the constant process effect, β_i is the linear effect of X_i, β_{ij} are the interactions of first order and β_{ii} are the quadratic effects of X_i.

Stat-Ease Design-Expert 7.1® (2008) is a statistical software that creates and evaluates general factorial designs, fractional factorial designs, response surfaces, optimal designs, and it was used in the present research. The software indicated that 21 experiments were necessary to calculate the regression coefficients for the full model.

2.3.3 Measurements

During the build process, the deposited Layer Height (LH) from the baseplate was measured with a digital vernier at at 50 mm, 100 mm and 150 mm; the three points were labelled M1, M2 and M3 (lh_{i,M_1}, lh_{i,M_2} and lh_{i,M_3}. The height of each layer (LH_i) was calculated as:

$$LH_i = \overline{x_i} - \overline{x_{i-1}} = \left(\frac{1}{3}\sum_{j=1}^{3} lh_{i,M_j}\right) - \left(\frac{1}{3}\sum_{j=1}^{3} lh_{i-1,M_j}\right) \tag{2.2}$$

This value was used to determine the height increment for deposition of the following layer. For the statistical analysis, given the thermal effect of the base plate, the first four layers were analysed one by one (LH_1, LH_2, LH_3, and LH_4 as shown in Figure 2.3) and for the remaining layers, i.e. from the 5th to the 15th, their overall average was considered:

$$LH = \mu = \frac{1}{11}\sum_{i=4}^{15} LH_i \tag{2.3}$$

The three transverse sections which were taken corresponded to the measurement points; they were placed into resin, ground, polished and etched with hydrofluoric acid in order to take optical microscopy images. The deposited walls have an irregular surface finish which makes a machining operation necessary to achieve plane side surfaces. However, in the present case the difference between the width before machining and the width which is the effectively usable one was minimal and not measurable.

Also the WWs, were considered separately, according to their dependance on the LH. To do this, a series of parallel lines was laid, orientated in the Y direction parallel to the baseplate, on the optical microscope images, each line corresponding to a specific layer height. This was possible because each cross section corresponded

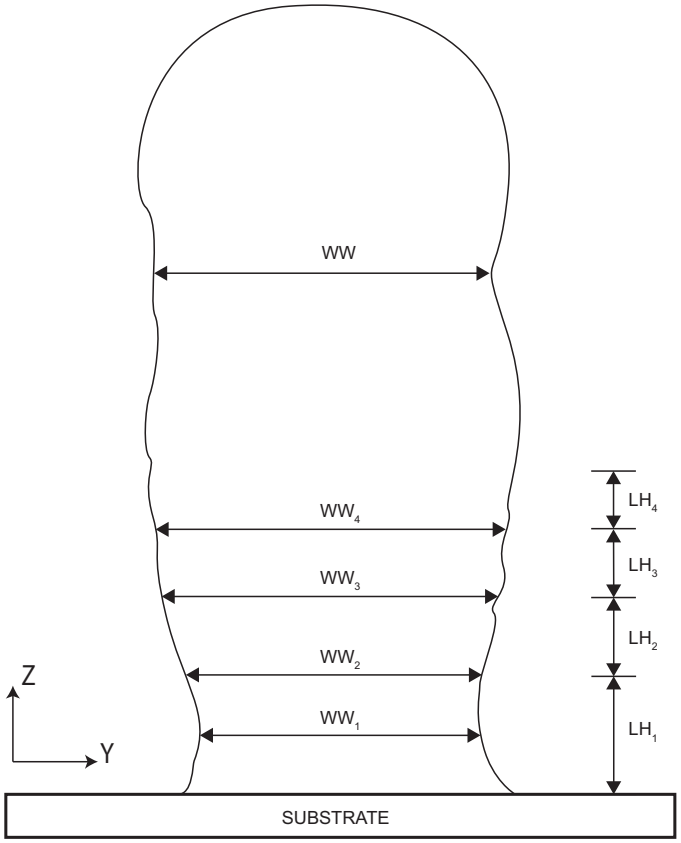

Figure 2.3: Schematic representation of a generic part cross-section. The wall width takes into account the width of the specimen, at its minimum point. The first four layers were considered separately to the upper part of the wall. The layer height corresponds to the increase in specimen's height after the deposition of a new layer and the first four layers were considered separately.

to the previously described measurement points, hence the height of each layer was known and was identifiable on the optical microscope images. Extracting the cross sections in correspondence of the measurement points was necessary, as any other cross section could have been slightly different in height/width due to normal noise occurring in the process.

The wall widths of the first four layers (WW_1 to WW_4) were taken only on the midpoint transverse section. When there was uncertainty in the values, conservative estimates were always taken.

2.4 Experimental results and discussion

2.4.1 Working envelope

The preliminary investigation on Ti–6Al–4V deposition showed that the constraints on the parameters that separate the feasible from the unfeasible combinations could be represented by the following equations:

$$1.2 \leq WFS(\mathrm{m\,min^{-1}}) \leq 4 \tag{2.4a}$$

$$2 \leq TS(\mathrm{mm\,s^{-1}}) \leq 6 \tag{2.4b}$$

$$120 \leq Current\ (\mathrm{A}) \leq 220 \tag{2.4c}$$

$$-184 \leq 60 \times WFS - 1.6 \times Current \tag{2.4d}$$

$$0 \leq -80 \times WFS + 1.6 \times Current \tag{2.4e}$$

$$-3 \leq -3 \times WFS + 1.8 \times TS \tag{2.4f}$$

These are represented graphically by the solid lines in Figure 2.4. To provide additional confidence in the process reliability and feasibility, the size of the region represented by constraints b, e, d, f was reduced by 10%. Their equations became

the following:

$$1.2 \leq WFS(\mathrm{m\,min^{-1}}) \leq 4 \tag{2.5a}$$

$$2 \leq TS(\mathrm{mm\,s^{-1}}) \leq 5.4 \tag{2.5b}$$

$$120 \leq Current(\mathrm{A}) \leq 220 \tag{2.5c}$$

$$-206.16 \leq 68.64 \times WFS - 1.91 \times Current \tag{2.5d}$$

$$22.08 \leq -92 \times WFS + 1.84 \times Current \tag{2.5e}$$

$$-2.69 \leq -3.4 \times WFS + 2.02 \times TS \tag{2.5f}$$

These are represented graphically by the dashed lines in Figure 2.4. The low WFS and TS limits are due to the need for high deposition rates and therefore lower values were not considered. The WFS upper limit was due to the hardware limitation of the Migatronic KT-4 wire feeder. The current upper limit is related to WFS and TS upper limits, as 220 A is the current necessary to melt the amount of the WFS upper limit ($4\,\mathrm{m\,min^{-1}}$) when the torch moves at the maximum speed ($6\,\mathrm{mm\,min^{-1}}$).

Please note the current considered in the DOE is the average one, given by the average of I_p and I_b described in section 2.3 on page 53.

2.4.2 Process capability

The ranges of measured responses are shown in Figure 2.5a, and a comparison against competing processes is shown in Figure 2.5b. The comparison data, for the CMT and PWD processes considers only out-of-chamber manufacturing methods, and is taken from the work of Almeida and Williams (2010), Eze (2009), Martina (2010), Milewski et al. (1999), Tolochko et al. (2004). It was assumed that the WW equalled the spot size for laser-based processes. Figure 2.5a shows how the range of both WWs and LHs is quite consistent and does not vary depending on the layer number. In Figure 2.5b, TIG deposition performs similarly to PWD, in terms of

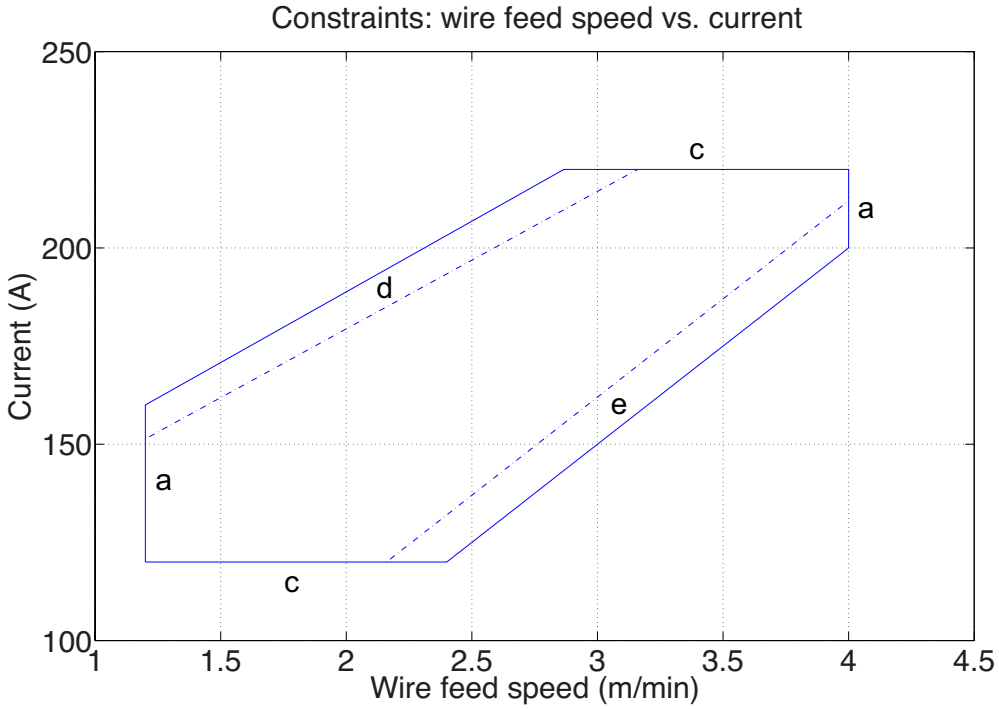

(a) Wire feed speed vs. Current

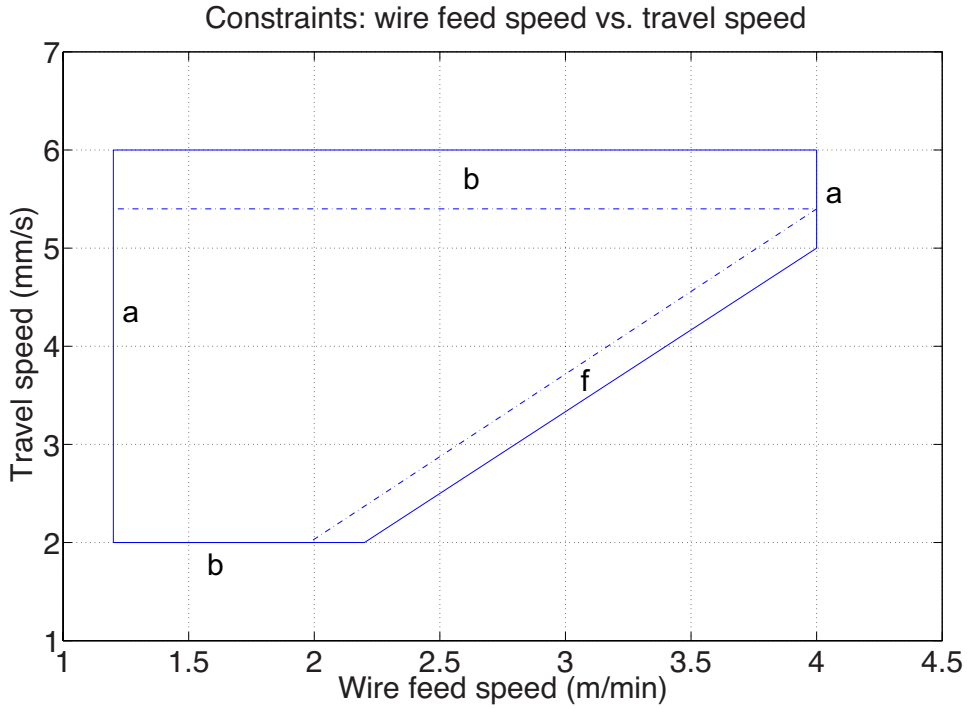

(b) Wire feed speed vs. Travel speed

Figure 2.4: Working envelope. The letters indicate the constraint each line refers to.

both WW and LH, although both are slightly smaller with TIG. The capability of TIG deposition is complementary to CMT, with the latter producing thinner walls with a much greater layer height. This suggests the possibility of combining the two processes to increase the overall capability of a manufacturing cell. The main advantage of the powder-bed laser deposition process is the small feature size capability, however they are characterised by a much lower deposition rate, which ranges from $100\,\mathrm{g\,h^{-1}}$ to $200\,\mathrm{g\,h^{-1}}$.

Figure 2.5c shows the ranges of wall widths that are achievable for each layer height. The minimum WW that can be obtained irrespective of the LH is around 5 mm. While the low WW value stays constant, the high value increases steadily and reaches its maximum at around 14 mm for a LH of 1.5 mm. For LH>1.5 mm the WW range reduces progressively, and eventually for a LH of 1.9 mm the WW ranges from 8 mm to 9 mm only. The process flexibility enables the layer height to be fixed for the whole part and the wall width may be varied according to the specific feature that needs to be built. What Figure 2.5c suggests is that beads with extreme aspect ratios ($^{\mathrm{WW}}/_{\mathrm{LH}}$) are not always achievable. A plot of the minimum and maximum aspect ratio for each layer height is shown in Figure 2.5d. The highest aspect ratios are produced for a very low LH; this means that for the lowest LH, only *relatively* high WWs are produced. As the LH increases, the minimum aspect ratio decreases linearly; this means the molten pool has the same minimum width up to a LH of 1.2 mm (see also constant minimum WW in Figure 2.5c). Above this value, the molten pool must increase in width in order to enable the deposition of thicker layers, and the minimum aspect ratio plateaus. As for the maximum aspect ratio, its trend is always negative; this means that as the LH increases, the process becomes less capable of adjusting the WW accordingly. This becomes more evident for LH above 1.6 mm, when the maximum aspect ratio reduces dramatically and in fact only a limited range of WWs can be produced. In conclusion, when thick layers are deposited the largest portion of the energy is used for melting the wire at the

expense of the underlying material.

The maximum deposition rate achieved using TIG deposition was $1.2\,\mathrm{kg\,h^{-1}}$; however it was constrained by the $4\,\mathrm{m\,min^{-1}}$ limit of the wire feeder used when doing the preliminary experiments (see section 2.3.1 on page 55). The process showed the potential for further increasing the deposition rate, provided both the heat input and the WFS could be increased. The time to deposit the 15 layers, considering deposition time only, ranged from 10 min 30 s to 31 min 15 s, and depended on travel speed.

Figure 2.6 shows a plot of the layer heights and wall widths, which considers the first four layers and the average values for the remaining layers for two specimens. The LH and WW are characterised by an opposite trend, the former decreasing, and the latter increasing, as the layer count increases. This justifies modelling the responses for the first four layers separately as described in section 2.3.3 on page 57. Furthermore, the trend lines confirm how the layer height becomes regular after the fourth layer.

2.4.3 Statistical analysis and process equations calculation

To determine the relationship between the measured response and the statistically significant variables, ANalysis Of VAriance (ANOVA) was performed. The coefficients from the response models are shown in Table 2.4.

2.4.3.1 Statistical tests

Table 2.5 presents the coefficients of determination (R^2) and $Adjusted - R^2$ for the models. The R^2 coefficients, which according to Montgomery (2006) measure the proportion of the variability in the data that can be explained by the model, indicate that over 90% of the variability can be explained by the models. In six cases it is over 95% and in five over 97%. In practice this should translate to good agreement with the actual dimensions.

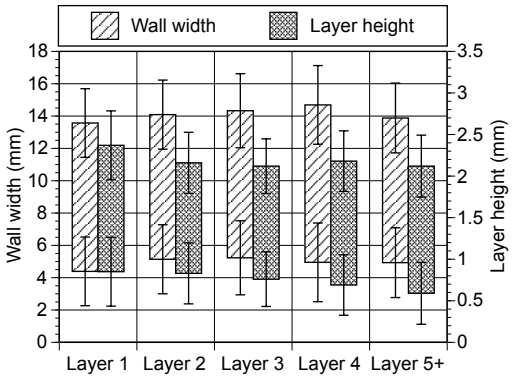

(a) Ranges of responses (error bars indicate standard deviations calculated by Stat-Ease Design-Expert 7.1®, 2008)

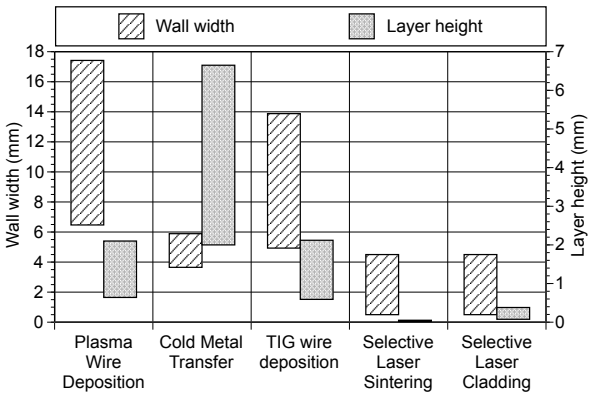

(b) Comparison between TIG deposition and other AM processes (WW and LH responses are considered)

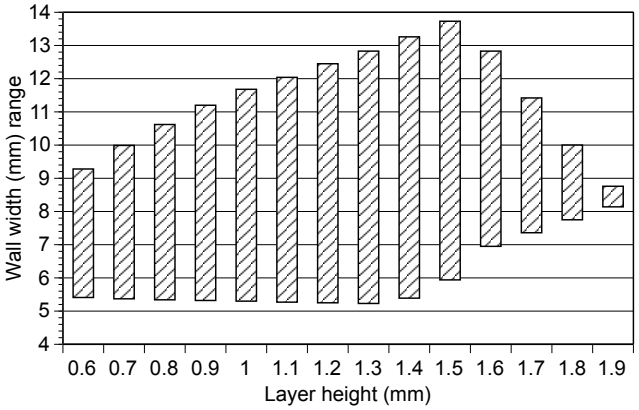

(c) WW range vs. LH

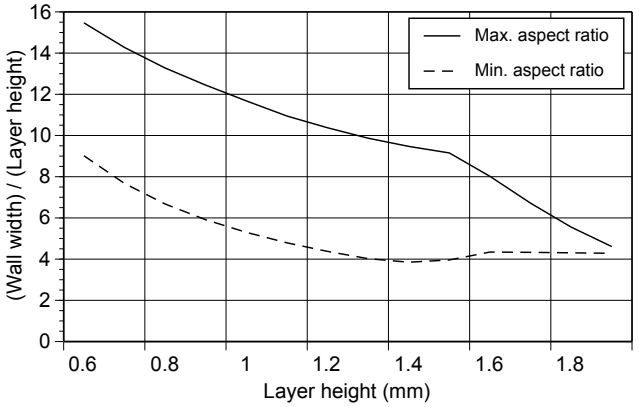

(d) Plot of min/max aspect ratios vs. LH

Figure 2.5: Process capability.

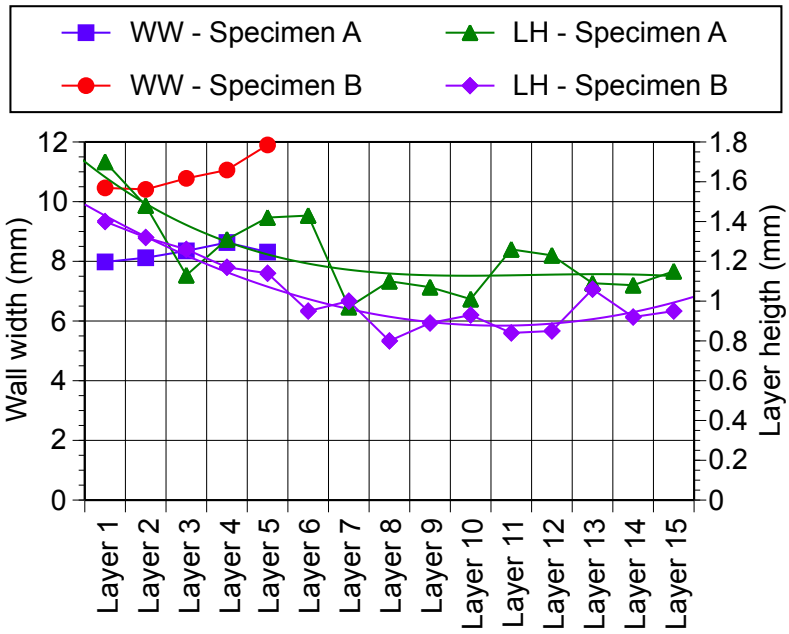

Figure 2.6: Plot of layer heights and wall widths for two experimental runs. Specimen A: WFS = 2.54 m min^{-1}, TS = 4.24 , I = 171.25 A; Specimen B: WFS = 1.2 m min^{-1}, TS = 2 , I = 160 A. The LH data was fitted with third order curves.

Montgomery (2006) explains that the $p - value$ helps the decision maker to determine the significance of the data, and its threshold is usually 0.05; and *Lack of Fit* is the sum of squares of dropped factors. Provided that all and only the insignificant terms were excluded from the model, one can assume that the significant *Lack of Fit* (indicated in bold in Table 2.5) is given by random errors in the data.

$Pred - R^2$ values, which predict the variability explained by the model for new data, are in reasonable agreement with the $Adjusted - R^2$ values and in all three cases the *Adeq. Precision* tests, which measure the signal-to-noise ratio, are greater than 4, which is the minimum value typically accepted for this term.

Table 2.4: Coefficients for model equations.

	β_0	**WFS**	**TS**	**Current**	**WFS × TS**	**WFS × Current**	**TS × Current**	**WFS²**	**TS²**	**Current²**
WW_1	−5.49305	−0.10944	−1.25221	0.17312	–	–	−0.00982	–	0.2083	−0.000249
WW_2	−4.4316	0.08481	−1.11694	0.16068	–	–	−0.01.25	–	0.23796	−0.000197
WW_3	1.24218	−0.25415	−0.38795	0.090561	−0.130	–	−0.012865	0.223	0.16675	–
WW_4	0.79272	−1.49566	0.66881	0.093807	–	–	−0.0127	0.29955	–	–
WW	3.15262	−0.14321	−1.42134	0.08558	–	–	−0.00986	–	0.216	–
LH_1	2.93727	0.34675	−0.34289	−0.010054	0.094132	0.00678	−0.00261	−0.29303	0.051225	–
LH_2	1.97787	0.81741	−0.61115	−0.0031	−0.066251	–	–	–	0.0697	–
LH_3	2.21991	0.84609	−0.60878	−0.00786	−0.085715	–	0.00111	–	0.0561	–
LH_4	1.97611	1.03728	−0.53129	−0.01	−0.1125	–	0.00152	–	0.0460	–
LH	0.72316	1.33352	−0.60234	0.00161	−0.068233	−0.00285	–	–	0.0738	–

Table 2.5: Statistical tests performed on the final models.

	R^2	**Adjusted $- R^2$**	**Pred. $- R^2$**	**Adeq. Precision**	**Lack of Fit p-values**	**P-values**
WW_1	0.987	0.9805	0.9576	47.849	**0.0128**	<0.0001
WW_2	0.9776	0.9663	0.9228	34.901	**0.0024**	<0.0001
WW_3	0.9922	0.9867	0.9679	47.329	0.0796	<0.0001
WW_4	0.981	0.9724	0.9466	35.301	0.0842	<0.0001
WW	0.9713	0.9611	0.9435	36.139	0.7165	<0.0001
LH_1	0.9534	0.9224	0.8111	16.667	**0.0011**	<0.0001
LH_2	0.9206	0.8941	0.83	20.408	0.1407	<0.0001
LH_3	0.919	0.8816	0.7654	18.736	0.2549	<0.0001
LH_4	0.9237	0.8884	0.7474	19.066	0.0523	<0.0001
LH	0.901	0.8554	0.738	16.664	**0.0017**	<0.0001

2.4.3.2 Analysis of plots

3D surfaces and contour plots were generated to represent graphically the regression equations. The WW (Figure 2.7 to Figure 2.9) does not seem to depend on the WFS, and it is mostly affected by the current and the TS. In fact, the surface plot in Fig 2.7a appears flat on the WFS axis and is then characterised by a linear increase as the Current increases. In Fig 2.7b, while the surface is still insensitive to any variation in WFS, it decreases as the TS increases. The lack of dependence on the WFS is shown also by its $p-value$, which is 0.3870. In fact, WFS $p-value$ is just about significant only in the case of the WW_3 model, in which it is 0.0401. In all other cases, it is always over 0.3 and even above 0.7 (WW_4). This would have normally resulted in this term being excluded from all process equations; however, due to its physical significance, it was kept.

The insensitivity to WFS in terms of WW is the main difference with PWD. In fact, Martina (2010) showed how in PWD an in increase in WFS results in an increase in WWs. This is possibly due to the effect of the plasma gas which applies an additional force on the molten pool, effectively spreading the molten pool over a larger surface, if the fed material increases.

On the contrary, the effect of TS and Current is in agreement with what was seen previously in PWD (Martina et al., 2012). The maximum WW is 13.87 mm and is achieved by using the lowest TS and Current close to the upper limit. The minimum WW is 5.21 mm and can be obtained by using the highest TS and the lowest Current. In other words, high heat input results in wider walls; and vice versa.

Contour plots in Figure 2.8 show the effect of the interaction of WFS and Current, for three different level of TS ($2\,\mathrm{mm\,s^{-1}}$, $4\,\mathrm{mm\,s^{-1}}$ and $6\,\mathrm{mm\,s^{-1}}$). Note the colourmap range is the same for the three figures. The contours are only shown for the region covered by the constraints described in section 2.4.1 on page 59. As seen previously, the behaviour of the WW is influenced marginally by the WFS and

substantially by the Current, especially at low TS (Figure 2.8a). At this TS, for a given WFS changing the current from 120 A to 200 A could lead to an increase in WW of 4 mm. The process is less sensitive to Current at medium TS (Figure 2.8b), while at high TS the impact of Current is minimal (Figure 2.8c).

Contour plots in Figure 2.9 show the effect of the interaction of WFS and TS, for three different levels of Current (120 A, 170 A and 220 A). Also in this case the colouring suggests very little effect of WFS, and the predominance of TS. Thinner walls can be achieved with a high TS, low WFS and low Current (120 A, Figure 2.9a). For medium levels of Current (170 A), a range of WWs spanning 9 mm can be obtained, and WW decreases with increasing TS (Figure 2.9b). For high levels of Current (220 A), the WW range spans only 6 mm, as the number of feasible parameter combinations is small, due to the constraints (Figure 2.9c).

The LH results are plotted in Figure 2.10 to Figure 2.12. Opposite to the WW, in this case the WFS does affect the response, as can be seen in Figure 2.10a in which the surface increases with the WFS. In the plot of the interaction of the WFS with the TS (Fig 2.10b), the surface shows a more quadratic behaviour given by the effect of the TS. The maximum LH is 1.91 mm and can be obtained by using a TS value close to its lower limit, and the lowest Current. The minimum LH is 0.53 mm and can be achieved with at least 44 different parameters combinations, one of them being with the lowest WFS, and a TS close to its upper limit. In other words, given that for continuity:

$$LH \times WW \propto WFS$$

and the WW is independent of WFS. It follows that $LH \propto WFS$. In fact, the maximum LH is achieved with the highest WFS compatibly with the constraints shown in Figure 2.4. Furthermore, given that minimum Current minimises the WW (see Figure 2.8), for the conservation of volume this must result in maximisation of LH.

The difference with PWD (Martina, 2010) is once again related to the WFS. In TIG deposition, due to the lack of constraint in the vertical direction the effect of

WFS is more prominent. Hence, an increase in WFS will result in a higher deposit, rather than a wider one.

The responses modelled for the first four layers (WW_1, WW_2, WW_3, WW_4, LH_1, LH_2, LH_3, LH_4) behave similarly to WW and LH, and therefore their specific plots will not be included.

An attempt to optimise the process could present the typical problems of multi-objective optimisation, which according to Trautmann and Mehnen (2009) aims at optimising concurrent objectives which are contradictory but depend on the same set of variables. Therefore, as reported by Ehrgott (2005), there is no unique optimal solution, but often a set of different solutions calculated by using desirability functions (see section 2.4.3.4 on page 77).

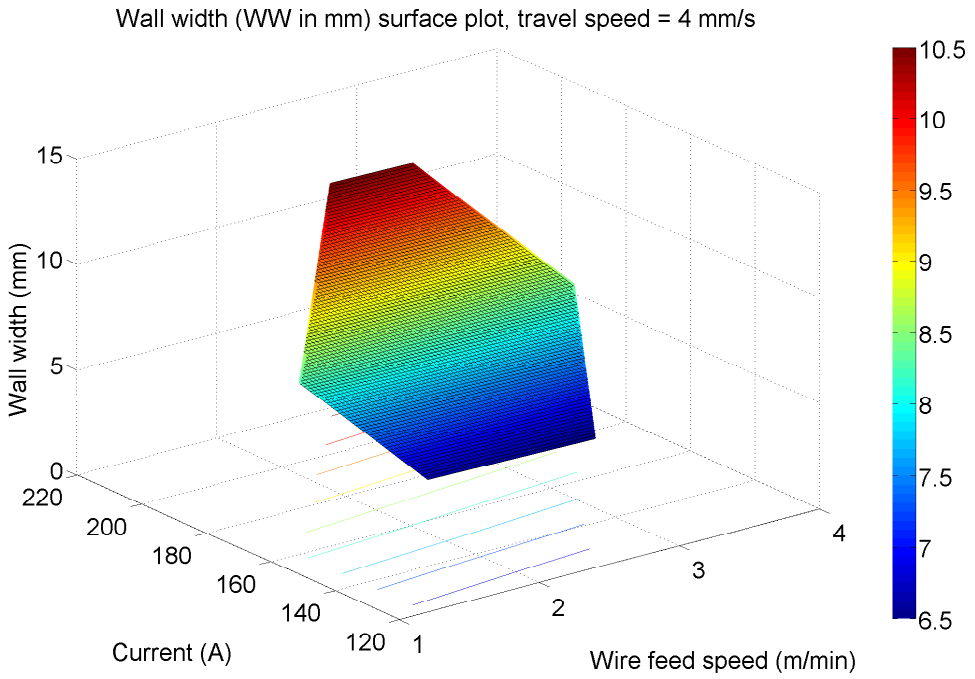

(a) WW as a function of WFS and Current (TS = 4 mm s^{-1})

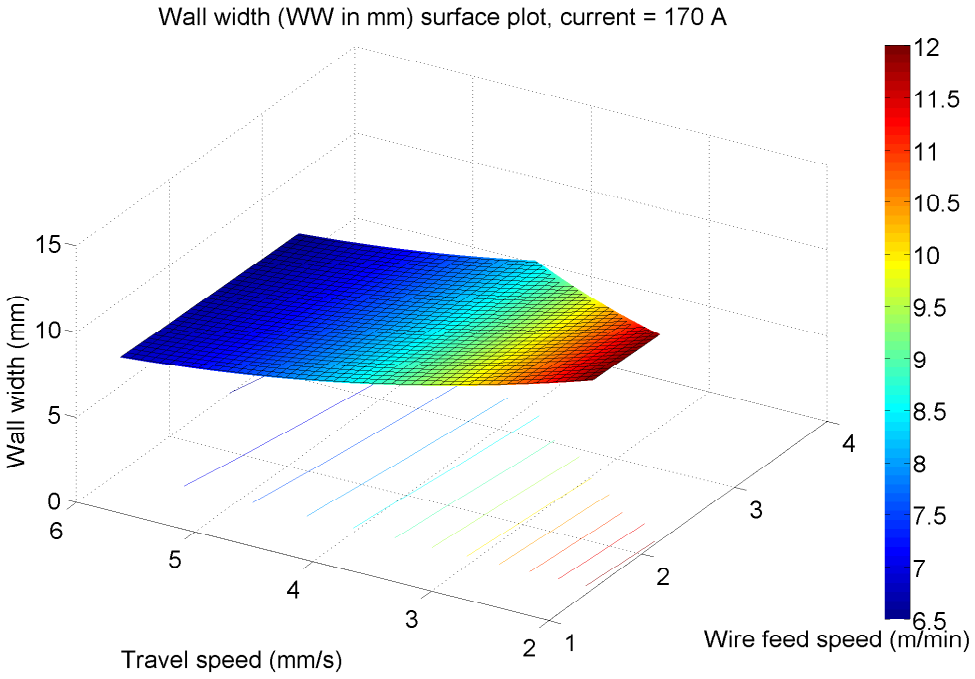

(b) WW as a function of WFS and TS (Current = 170 A)

Figure 2.7: Wall width 3D surfaces.

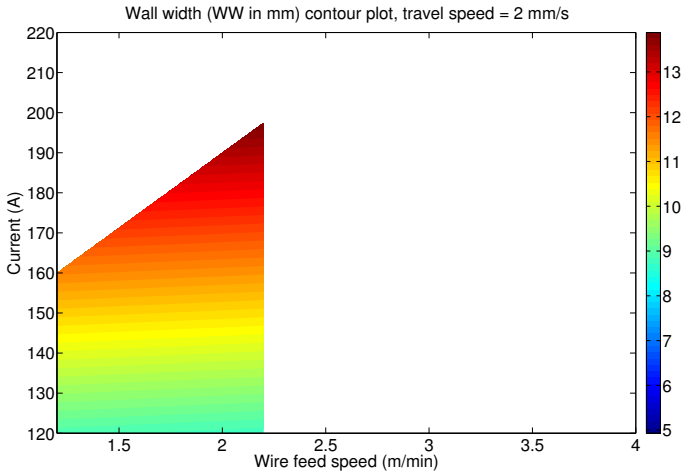

(a) TS = $2\,\mathrm{mm\,s^{-1}}$

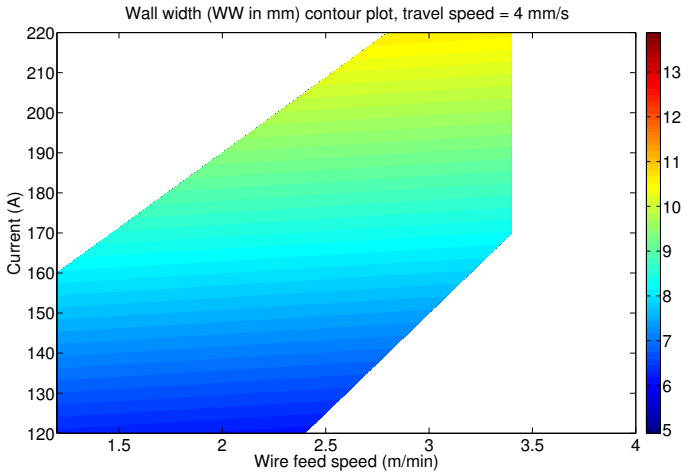

(b) TS = $4\,\mathrm{mm\,s^{-1}}$

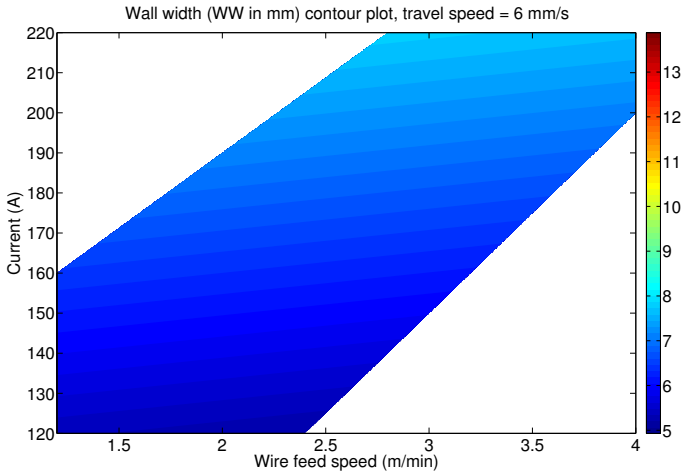

(c) TS = $6\,\mathrm{mm\,s^{-1}}$

Figure 2.8: Wall width contour plots on the WFS – Current plane. Note colormap range is the same for the three figures.

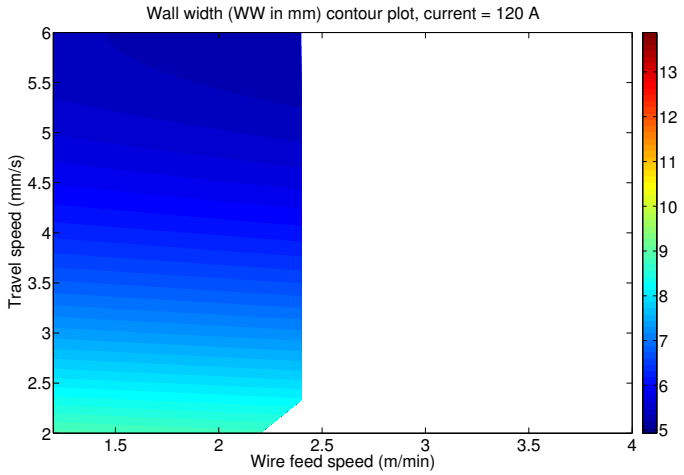

(a) Current = 120 A

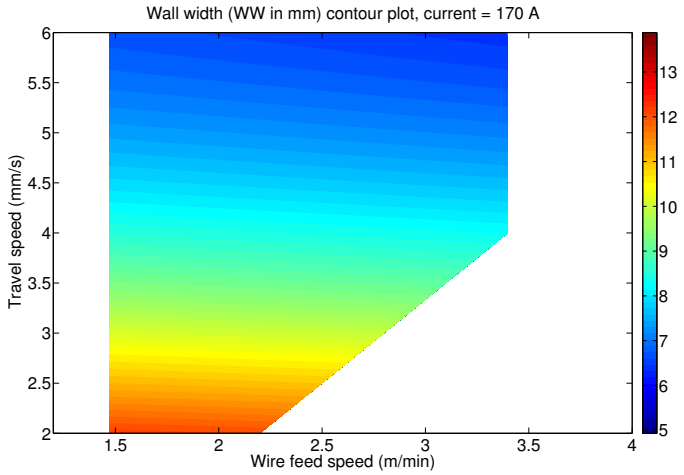

(b) Current = 170 A

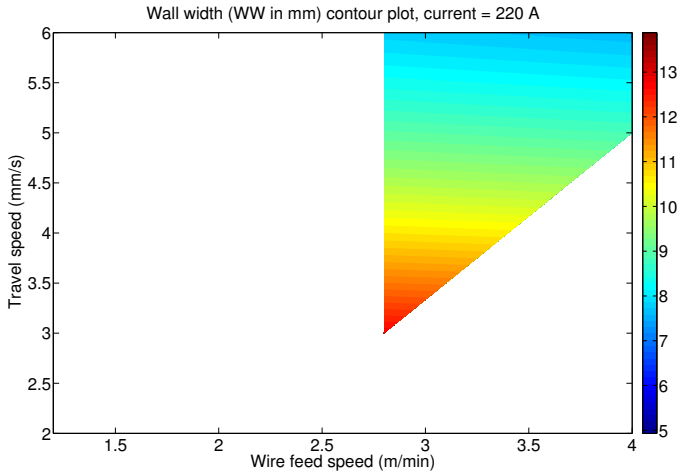

(c) Current = 220 A

Figure 2.9: Wall width contour plots on the WFS – TS plane. Note colormap range is the same for the three figures.

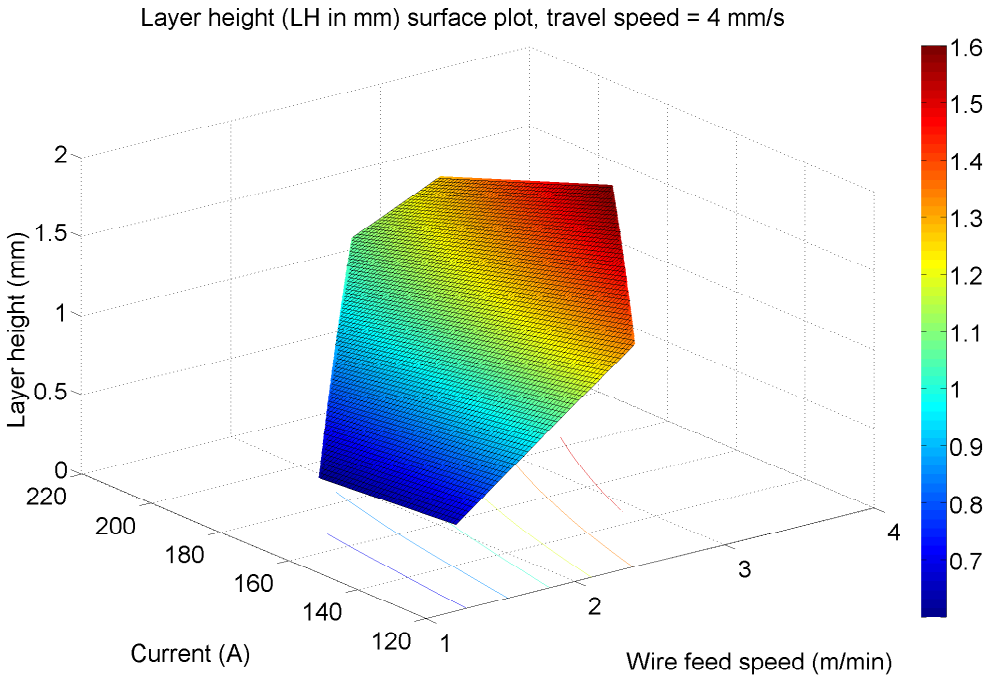

(a) LH as a function of WFS and Current (TS speed = 4 mm s^{-1})

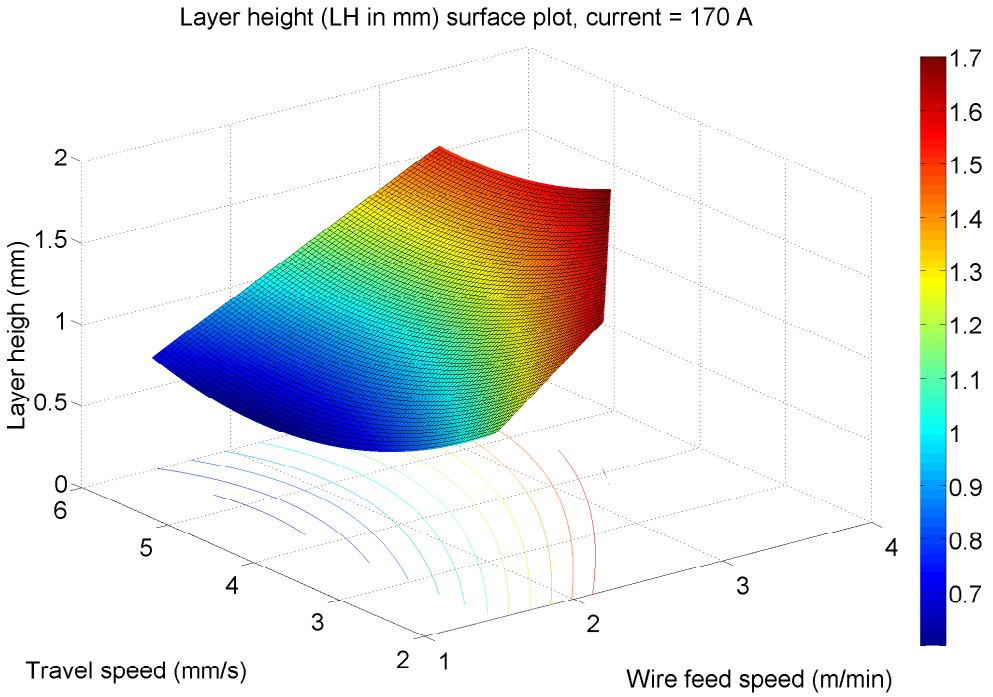

(b) LH as a function of WFS and TS (Current = 170 A)

Figure 2.10: Layer height 3D surfaces.

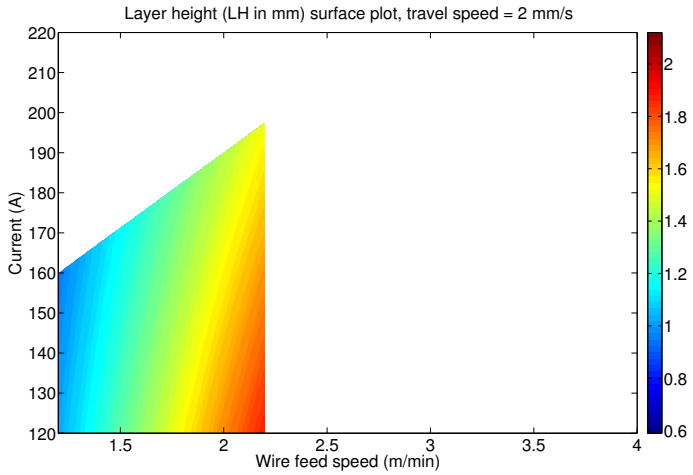

(a) TS = 2 mm s^{-1}

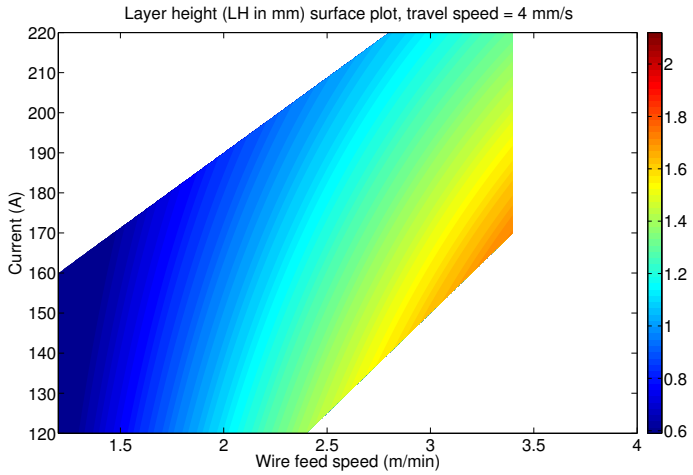

(b) TS = 4 mm s^{-1}

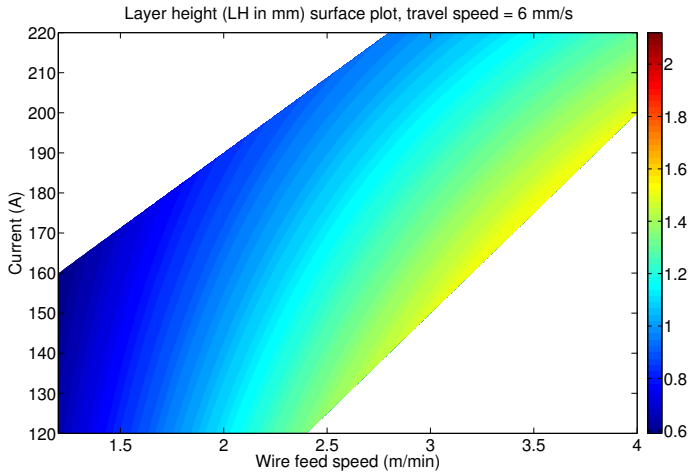

(c) TS = 6 mm s^{-1}

Figure 2.11: Layer height contour plots on the WFS – Current plane. Note colormap range is the same for the three figures

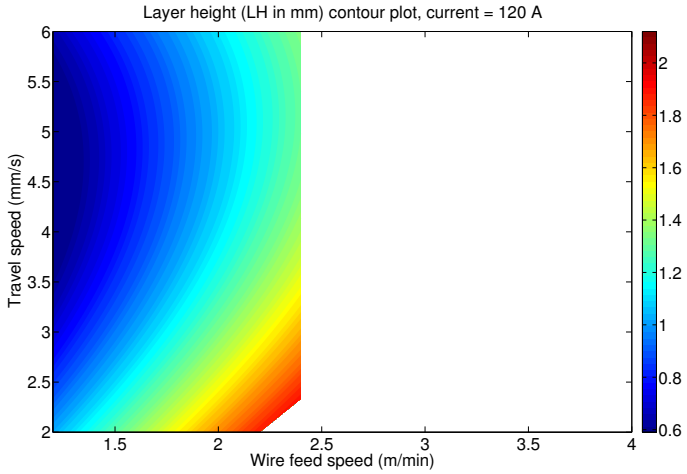

(a) Current = 120 A

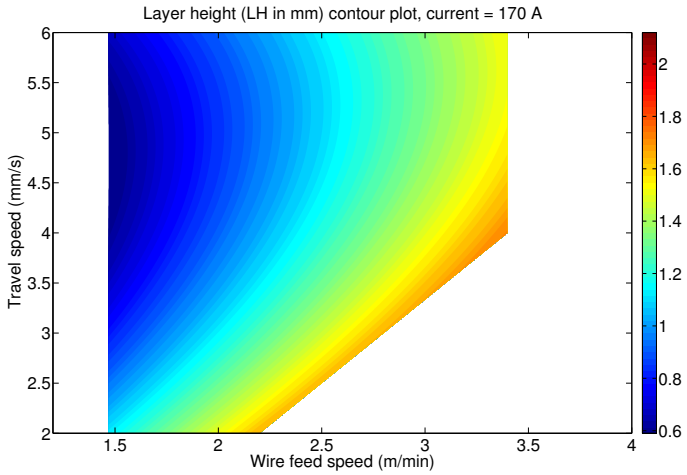

(b) Current = 170 A

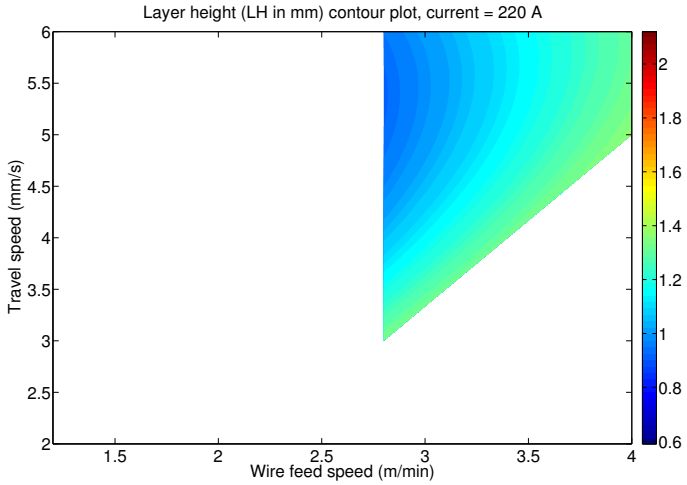

(c) Current = 220 A

Figure 2.12: Layer height contour plots on the WFS – TS plane. Note colormap range is the same for the three figures.

2.4.3.3 Model validation

Two additional walls were built to validate the models:

1. *Validation 1*: the parameters were selected randomly within the working envelope, with:
   (a) WFS = $2.5\,\mathrm{m\,min^{-1}}$
   (b) TS = $4\,\mathrm{mm\,s^{-1}}$
   (c) Current = 150 A.
2. *Validation 2*: the parameters were chosen so that a WW of 12 mm could be obtained, with:
   (a) WFS = $2.4\,\mathrm{m\,min^{-1}}$
   (b) TS = $2.6\,\mathrm{mm\,s^{-1}}$
   (c) Current = 190 A.

The measured values were compared with those predicted by Stat-Ease Design-Expert 7.1® (2008), as shown in Figure 2.13. All values fell within the calculated 95% confidence intervals, except for the LH_2 of the first specimen (underestimated), and WW_2–WW_3 of the second (overestimated). It must be said the most important parameter to have confidence in is the WW, for which the model proved to be reliable. In fact, should the WW be underestimated by a large amount, the manufactured part would be scrapped. On the contrary, solutions such arc voltage control proved to be capable of overcoming the inaccuracy that might occur in the LH prediction, as its closed loop feedback instantaneously adjusts the electrode-to-workpiece distance. Consequently, errors in LH prediction are not crucial for the successful deposition of the part.

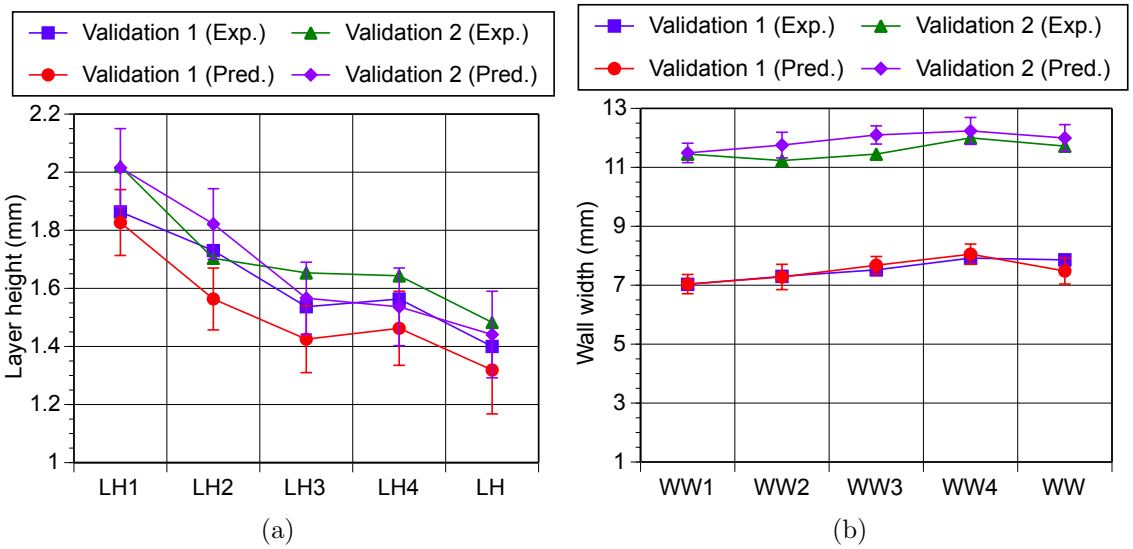

Figure 2.13: Comparison of experimental vs. predicted results for two specimens built in order to validate the calculated models. (a) evaluation of layer height models; (b) evaluation of wall width models. Error bars represent 95% confidence intervals.

2.4.3.4 Case study

Let us analyse a practical example. A manufacturer is asked for a straight wall for mechanical properties testing. The design specification reports a part length of 250 mm, a height of 150 mm and a width of 10 mm. The width already includes a safety machining margin to achieve an effective width of 9 mm. The manufacturer wants to deliver the part as early as possible so he identifies two requirements: maximisation of the WFS, which accounts for the deposition rate, as well as maximisation of LH, to reduce the number of layers and therefore start/stops. In practice, he sets a target for the WW, while attempting the maximisation of both WFS and LH. The optimisation procedure is based around the simultaneous optimisation technique described in Derringer and Suich (1980) and Montgomery (2006, p. 451). The optimisation algorithm ran by Stat-Ease Design-Expert 7.1® (2008) returns a set of solutions with Desirability index equal to 0.752 (this index is equal to 1 when all constraints and targets are met). The first proposed solution would give a WW of 10 mm and a LH of 1.5 mm, with WFS = 3.2 m min^{-1}, TS = 3.7 mm s^{-1} and I = 195 A. The manufacturer then knows that 100 layers would be necessary to

build the part. Each layer would take 68 s for the actual deposition, plus 10 s for the pre purge and 20 s for the post purge, giving a time for each layer of 98 s. Without including the start/stops, the total building time is 2 h 40 min.

2.4.4 Model limitations

One of the downsides of ANOVA and DOE in general is the lack of physical understanding as a consequence of the regression analysis. The whole process is treated as a *black box* into which inputs are fed and output measured (Montgomery, 2006). The resulting process equations are convenient from a practical point of view, because they enable process optimisation in both the numerical[1] and the point prediction[2] forms. To a certain extent, the calculation of the regression coefficients for each of the terms enables a minimum understanding of their *weigth*, i.e. the magnitude of their effect on the measured responses; however this is still far from clarifying what the constitutive relationships are.

Another of the limitations of this work is only straight wall, vertical structures have been investigated. At the moment, it is unknown if the model would work also when producing curved or non-vertical structures. Moreover, multi-pass walls (i.e. walls of greater thickness, generated by the deposition of side-by-side beads at the same Z coordinate) have not been attempted.

Finally, the model was not tested on different equipment (torches, power sources, etc.), so it is unclear whether these results are transferrable. The same applies for different materials. Martina (2010) found an identical behaviour between stainless steel and Ti–6Al–4V in terms of process working envelope; however the empirical process equations are unlikely to be transferrable.

[1]The calculation of what the process parameters should be, given the desired response
[2]The calculation of a response for a given set of inputs

2.4.5 A physics-oriented approach

To overcome some of the limitations described in the previous section, the experimental data was reanalysed with a physics-oriented approach. Instead of looking at the process as a *black box*, the input data available for the steady-state deposition was reorganised in a physically meaningful way. Two equations were developed:

$$WW = 3.70 + 8.48\ HI \tag{2.6}$$

$$LH = 0.59 - 1.08\ HI + 0.12\ {}^{WFS}/_{TS} \tag{2.7}$$

HI is the heat input, calculated as

$$HI = \frac{V\ Current}{TS} \tag{2.8}$$

where V is the arc voltage. The statistical tests performed on these equations are shown in Table 2.6; R^2, $Adjusted - R^2$ and $Pred - R^2$ are worse than the respective models output of the DOE, however the alternative models show better *Adeq. Precision* which means they have a better signal-to-noise ratio.

Table 2.6: Statistical tests performed on the alternative models.

	$\mathbf{R^2}$	**Adjusted** $\mathbf{- R^2}$	**Pred.** $\mathbf{- R^2}$	**Adeq. Precision**	**Lack of Fit p-values**	**P-values**
WW	0.9192	0.9147	0.9060	39.193	0.2279	<0.0001
LH	0.8325	0.8128	0.7202	20.090	**0.0011**	<0.0001

In the case of the WW, the heat input alone can explain most of the variation around the mean seen in the experimental data, regardless of the WFS and in turns regardless of the quantity of added material. This confirms the lack of statistical significance of the WFS model term captured also in the initial analysis (see page 67).

As for the LH, the heat input has a negative coefficient: the molten pool dimension increases with the heat input producing wider walls, and lower layer heights.

The addition of the $^{WFS}/_{TS}$ term accounts for the added material per unit length. If the TS is fixed, so is the heat input (see equation 2.8); if the WFS is increased then the WW does not vary, and in turns the LH must increase accordingly.

2.5 Summary and conclusions

In this Chapter the feasibility of TIG deposition for AM purposes has been demonstrated:

- A working envelope in which the process behaves steadily and delivers acceptable parts has been defined;
- The process has been modelled empirically, through a systematic approach i.e. DOE, and specifically D-Optimal design;
- Modelled responses include: LH, WW for the first four layers, and the average for the remaining ones;
- The model has been validated successfully.

In terms of process capability:

- LH ranged from 0.6 mm to 2.12 mm;
- WW ranged from 4.9 mm to 13.9 mm;
- Maximum deposition rate was 1.2 kg h^{-1} (limited by wire feeder).

From a statistical point of view:

- WW is highly dependant on the current;
- LH is dependant on wire feed speed.

The DOE findings were confirmed by a subsequent analysis which related the WW to process heat input, and the LH to both heat input and $^{WFS}/_{TS}$ ratio. Recommendations include:

- Alternate the deposition direction to avoid build up at the beginning of the wall, and sloping at the end;
- select parameter combinations which are not on the edge of the working envelope;
- in case of more than one suitable combination, consider productivity factors such as maximising WFS and LH;
- study of alternative methods of shielding;
- study of alternative methods of wire feeding;
- maximise substrate utilisation by cutting as little substrate as possible to accommodate the actual part and the clamps;
- maximise productivity by depositing more than one part in the same cell.

Chapter 3

Effect of rolling on microstructure of WAAM parts

This chapter contains material from the following articles:

Martina, F., Williams, S., Colegrove, P.A., 2013. Improved microstructure and increased mechanical properties of additive manufacture produced Ti–6Al–4V by interpass cold rolling, in: 24th International Solid Freeform Fabrication Symposium, Austin, Texas, USA. pp. 490–496.

Colegrove, P.A., Coules, H.E., Fairman, J., Martina, F., Kashoob, T., Mamash, H., Cozzolino, L.D., 2013. Microstructure and residual stress improvement in wire and arc additively manufactured parts through high-pressure rolling. Journal of Materials Processing Tech. 213, 1782–1791.

Martina, F., Colegrove, P.A., Williams, S.W., Meyer, J., 2014a. Microstructure of interpass rolled Wire + Arc Additive Manufacturing Ti–6Al–4V components. Journal of Materials Processing Tech. (submitted).

3.1 Context

Titanium Wire+Arc Additive Manufacturing (WAAM) deposits are characterised by long prior β columnar grains. This microstructure is undesirable from a mechanical point of view. In the present chapter, rolling is used as a means to eliminate the columnar grains and produce a refined, equiaxed, texture-free microstructure.

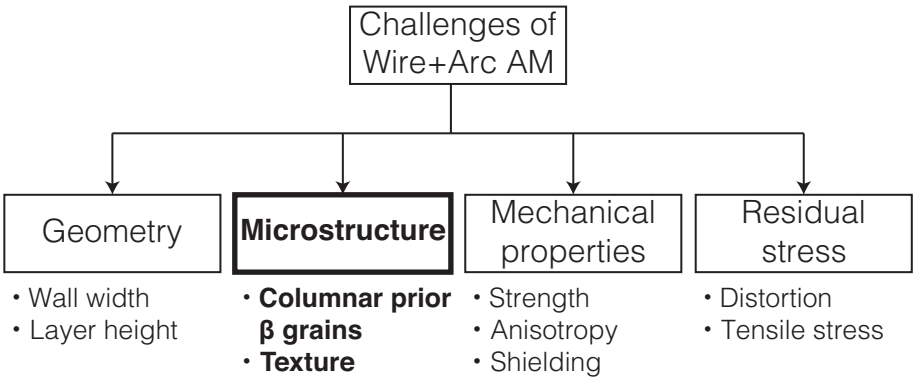

Figure 3.1: Project map. In bold the work package object of the present chapter.

3.2 Introduction

In Ti–6Al–4V Additive Manufacturing (AM) components, prior β grains are equiaxed within the substrate, however due to epitaxial grain growth large columnar grains are observed in the bulk of the deposited components; these traverse the deposited layers and can be as long as the whole height of the component. Wang et al. (2013) show how the prior β grains grow perpendicular to the thermal gradient and are highly textured, leading to anisotropic mechanical properties.

Ding et al. (2011) explained that other issues affecting AM components are residual stress and distortion. A variety of methods may be used to reduce these; one of the most effective is inter-pass rolling. Originally developed for welding by Kurkin and Anufriev (1984), inter-pass rolling has been investigated recently by Coules et al. (2012b). As stated in Altenkirch et al. (2009) the method consists in introducing plastic deformation: the material is compressed normal to the surface and consequently it is strained plastically parallel to the surface. This longitudinal deformation counteracts the mismatch strain caused by welding. In turns, residual stresses are significantly reduced. Rolling methods can be applied either *in situ* or *post weld*, however Coules (2013) demonstrated that the latter is more effective than the former.

Inter-pass rolling was applied recently to linear steel WAAM deposits by Colegrove et al. (2013). Particularly at the interface with the substrate, there was

a residual stress reduction, however rolling was less effective than when applied to welded joints, due to the strain that occurs in the transverse direction during rolling. To overcome this shortcoming, a roller that restrained the material in the transverse direction was developed; this roller proved to be more effective in reducing both residual stress and distortion. The most significant finding from this work's point of view was the reduction in grain size due to the enhanced recrystallisation that occurred with the deposition of the subsequent layer on the plastically deformed component.

Therefore this chapter investigates whether similar reductions in grain size are achievable when rolling Ti–6Al–4V WAAM components.

3.3 Experimental procedure

The experiments were performed on a custom-made rolling rig, equipped with a Lincoln Electric Invertec V310–T AC/DC Tungsten Inert Gas (TIG) power supply. A schematic view of the setup is shown in Figure 3.2a (the X, Y and Z directions are defined in this figure). The electrode-to-workpiece distance was 3.5 mm. The parameters for the pulsed TIG process are presented in Table 3.1 which produced a Wall Width (WW) of 6 mm. The composition of the Ti–6Al–4V wire is shown in Table 3.2.

Table 3.1: Deposition parameters.

Wire feed speed	$1.6\,\mathrm{m\,min^{-1}}$
Travel speed	$4.5\,\mathrm{mm\,s^{-1}}$
Peak current	150 A
Background current	70 A
Average current	110 A
Pulse duration	0.5 s
Frequency	10 Hz
Gas flow rate	$10\,\mathrm{l\,min^{-1}}$
Trailing shield gas flow rate	$20\,\mathrm{l\,min^{-1}}$
Torch stand-off	3.5 mm

Table 3.2: Chemical composition of Ti–6Al–4V wire used in the experiments.

Ti	Al	V	Fe	O	C	N	H	TOE	Y	Others
Bal.	6.08	4	0.18	0.16	0.035	0.011	0.0017	<0.2	<0.001	<0.05

3.3.1 Evaluation of microstructure

These experiments were used to characterise the microstructure in WAAM samples that were rolled between depositing layers. Baseplates were 405 mm long, 60 mm wide and 6 mm thick, and were clamped by screws along each side of the plate. (Figure 3.2b). Six walls were built: a "control" left in the as-deposited condition; three samples that used a "profiled" roller with loads of 50 kN, 75 kN and 100 kN, and two that used a roller with a flat profile and loads of 50 kN and 75 kN. The specimen rolled at 100 kN fractured during rolling of the seventh layer and was excluded from any analysis.

The "profiled" roller's shape approximately conformed to the profile of the deposit as shown in Figure 3.2c. Both rollers were made of case-hardened H13 tool steel and a rolling speed of $8\,\mathrm{mm\,s^{-1}}$ was used. Layer deposition and rolling application were alternated and the part was allowed to cool to room temperature, before rolling was applied. Deposition started 20 mm from the end of the baseplate and stopped 15 mm from the other end (Figure 3.2b), giving a total wall length of 370 mm. Rolling began and ended 35 mm from the ends of the deposit.

Three sections were taken at the same points M1, M2 and M3 (Figure 3.2b); mounted into resin, ground, polished and etched with a solution of hydrofluoric acid for optical microscopy imaging. The images were used for prior β grain size measurement, which was done with the the linear intercept method described in ASTM E112 – 96 (2004). For each image, five measurements were taken for three directions (0°, 45°, 90°) giving a total of 15 measurements per sample.

The thickness of α lamellae in the samples produced with the profiled roller was measured using five Scanning Electron Microscope (SEM) images. Each image

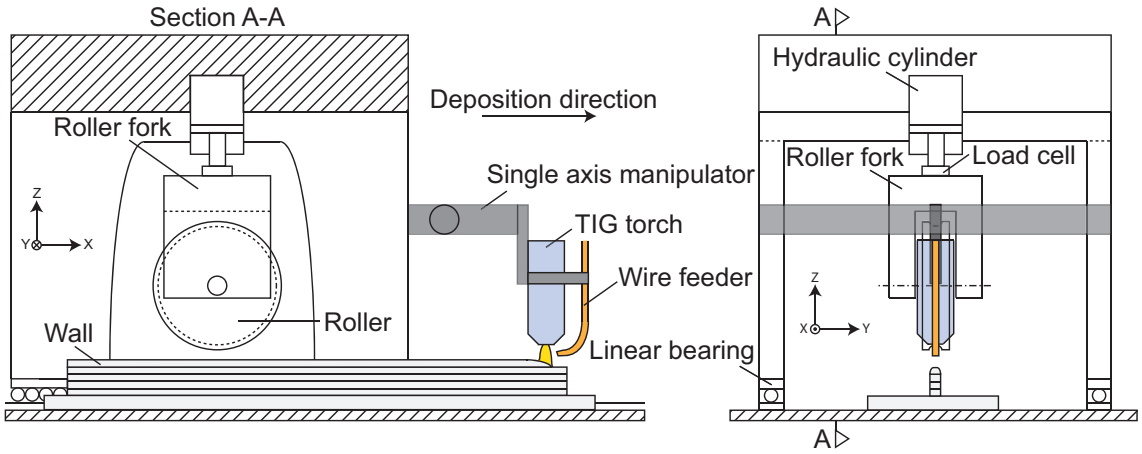

(a) Schematic diagram of rolling and welding equipment.

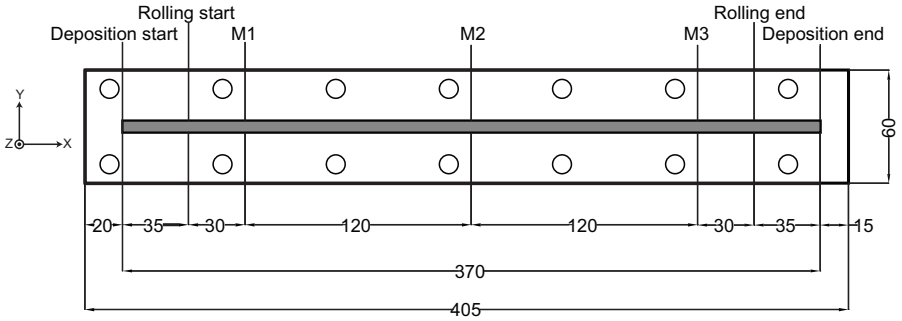

(b) Details of base plate including holes for clamping

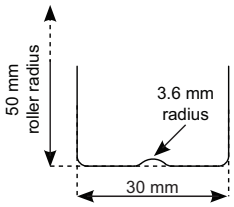

(c) Dimensions of the roller

Figure 3.2: Experimental setup for rolling investigation.

corresponded to a specific location within a generic band, as described in Martina et al. (2012). Prior to the SEM investigation, the samples were re-polished for eight minutes at 100 kg/m^2 and 80 rpm. SEM images were taken using a backscatter detector, a voltage of 20 keV and a spot size of four. The images were processed with Adobe Photoshop CS4® (2008). For each image, five measurements were taken for the four directions (0°, 45°, 90°, 135° orientations) giving 20 measurements per location, in accordance with ASTM E1382 – 1997 (1997), to take into account the strong anisotropy of the microstructure. The number of intercepts across each line was determined using ImageJ (2012) software and its plugin Measure Roi PA (2012). Finally the α lamellae thickness was determined as $^1/_{1.5(1/\lambda)_{mean}}$ where λ_{mean} is the mean intercept length (Tiley et al., 2004).

Electron Backscatter Diffraction (EBSD) scans were performed with a voltage

of 20 keV and a step size of 3 µm. The reconstruction of the β phase from the EBSD scans was performed at the University of Manchester by Jack Donoghue and Alphons Antonysamy using the software developed in Davies (2009), Davies et al. (2011), based on the method presented in Humbert et al. (1994).

3.3.2 Fundamental study

The fundamental study was used to understand the microstructural changes that occur as a result of rolling and deposition. Baseplates were 250 mm long, 60 mm wide and 6 mm thick, and were clamped by screws along each side of the plate. In this study four linear walls of 20 layers each were deposited without any inter-pass rolling. Subsequently the following treatments were applied: for two walls only the last layer was rolled with loads of 50 kN and 75 kN respectively; for the other two, only the last layer was rolled at 50 kN and 75 kN respectively after which an *additional* layer was deposited. Only the profiled roller was used for this investigation. These four walls were sectioned, and critical points in terms of microstructural changes were identified. The sample rolled at 75 kN with a subsequent layer deposited was repeated: before depositing the 21st layer two R-type thermocouples[1] were spot welded into the bottom of ϕ 3.2 $\times$ 3 mm deep holes, drilled perpendicular to the side of the deposit, 4.5 mm and 4.9 mm below the top. These holes corresponded to 5.6 mm and 6 mm below the expected top of the 21st layer. With regards to the point 6 mm below the surface, the experiment was repeated a further two more times to validate the temperature measurements. In the first repetition the temperature was measured in four points with R-type thermocouples. In the second, it was measured in four more points with K-type thermocouples[2].

[1]Rated for temperatures up to 1600 °C
[2]Rated for temperatures up to 1350 °C

3.4 Experimental results

The microstructures from the five samples are shown in Figure 3.3. All the samples were slightly narrower near the baseplate due to the different heat flow in this region which has been previously reported in Martina (2010).

The control sample demonstrated large, columnar prior β grains, which grew epitaxially from the baseplate toward the top of the sample (Figure 3.3a). In the rolled samples there was a significant reduction in the prior β grain size which decreased with increasing rolling load (Table 3.3). Note that it was not possible to provide a grain size measurement for the control sample because the columnar grains violated the equiaxed grain structure required by ASTM E112 – 96 (2004).

Table 3.3: Prior β grain sizes.

	Profiled roller	Flat roller
50 kN	125 µm	139 µm
75 kN	89 µm	56 µm

The grain refinement is even more evident in the EBSD images provided in Figure 3.4. These images are maps of the reconstructed β phase. The control specimen, showed in Figure 3.4a was characterised by highly textured prior β grains, as indicated by the uniform red colouring of the epitaxial grains. Differently from the other images in the same figure, Figure 3.4a was obtained from an EBSD scan which included part of the baseplate. Please note how the baseplate showed a microstructure which was much finer, as well as less textured. The transition between the baseplate and the anisotropic portion was also more evident thanks to the colouring. Figure 3.4b to Figure 3.4e show EBSD images obtained from scans performed in the centre of the walls, rolled with both the profiled and the flat roller. The randomisation of the texture was significant, as well as the isotropic configuration of the prior β grains. Higher rolling loads correspond to finer grains, in agreement with what was measured and shown in Table 3.3.

The main difference between the microstructures produced by the flat and pro-

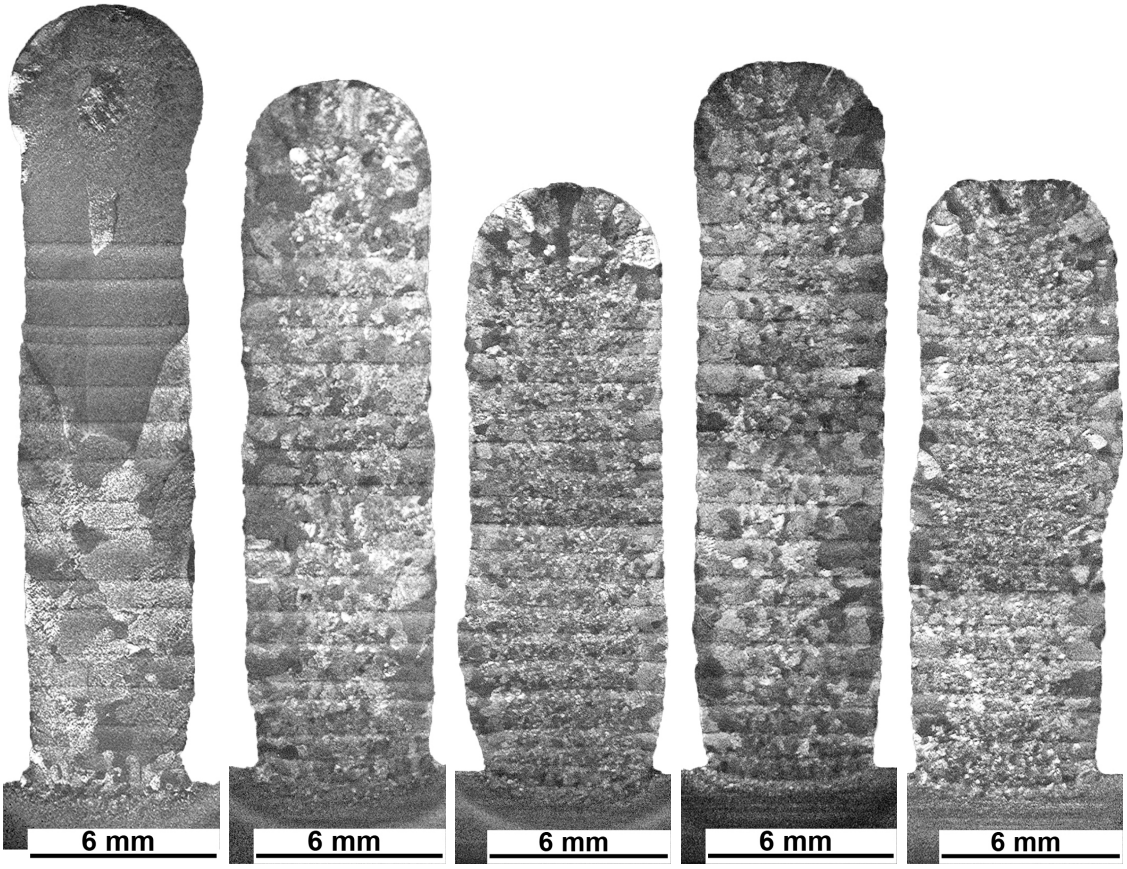

(a) Control (b) Profiled roller at 50 kN (c) Profiled roller at 75 kN (d) Flat roller at 50 kN (e) Flat roller at 75 kN

Figure 3.3: Optical microscopy images of control and rolled samples.

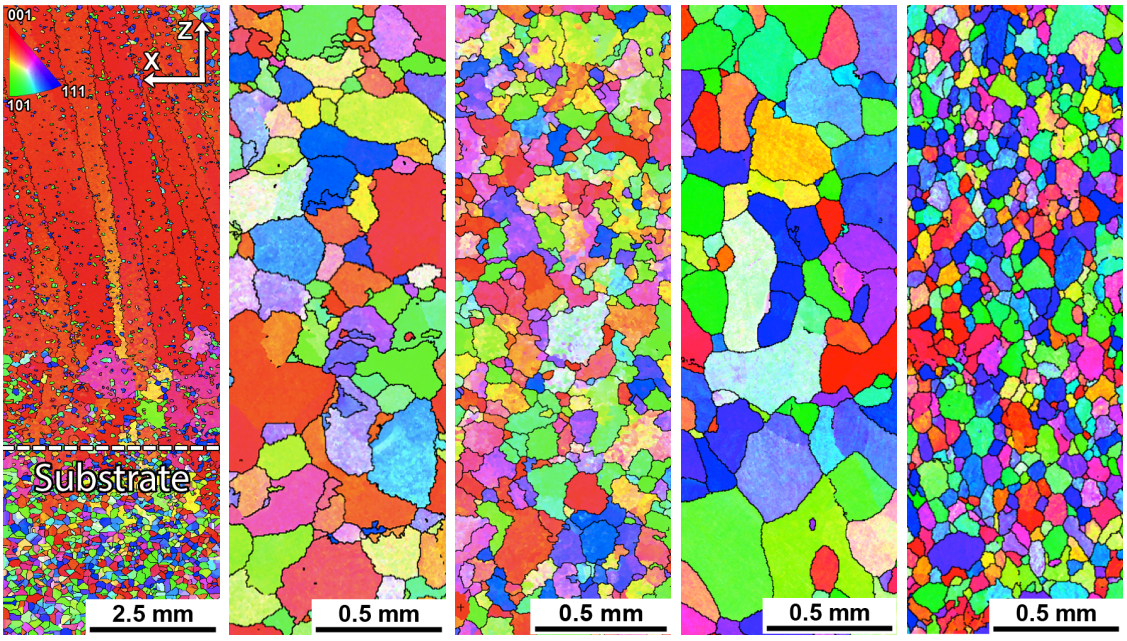

(a) Control (from the bottom part of the wall) (b) Profiled roller at 50 kN (c) Profiled roller at 75 kN (d) Flat roller at 50 kN (e) Flat roller at 75 kN

Figure 3.4: EBSD images of reconstructed prior β grains of control and rolled samples ((a), (b) and (c) edited from Antonysamy, 2012). Please note the difference in scale.

filed rollers is the size of the prior β grains along the sides of the samples. While the grain size was fairly uniform across the sample with the profiled roller (Figure 3.3b and 3.3c), the sample produced with the flat roller had grains that were approximately five to ten times larger along the surface of the walls (Figure 3.3d and 3.3e).

Horizontal bands were observed in the macrostructures of all the samples, one being produced with each deposited layer (Figure 3.3 and Figure 3.5a). In addition, columnar prior β grains were observed in the top ca. 2 mm of all samples. Within the top region of all samples, martensite was found, which is evidenced by the characteristic needle-like microstructure (Lütjering and Williams, 2007, p. 30) and is shown in Figure 3.5b for the sample rolled at 75 kN with the profiled roller.

The rest of the sample had a Widmanstätten microstructure (Figure 3.5c). Within each band, the thickness of the α lamellae varied, being larger near the top and smaller near the base, and is plotted in Figure 3.5d. While this repetitive pattern was observed in all the samples, the overall thickness of the α lamellae decreased as the rolling load increased.

The change in texture, for both the α and β phases respectively, is shown in Figures 3.6 and 3.7. The change in α phase texture when rolling was substantial and evident when comparing Figure 3.6a to Figure 3.6b and Figure 3.6c. The control specimen showed an α texture pole intensities peaking at six $\times$ random, while in the rolled sample maximum intensities are below two $\times$ random.

As for the β phase, the control sample, shown in Figure 3.7a, was characterised by an established $<001>_\beta$ fibre texture peaking at 22 $\times$ random. As the rolling load increased (Figure 3.7b and Figure 3.7c), the texture observed in the control specimen gradually transformed into a rolling one. According to Antonysamy (2012), in the rolled specimens the texture seemed to rotate away from the Z direction and strangely had a symmetry rotated by 90° with regards to what is seen in rolled sheets.

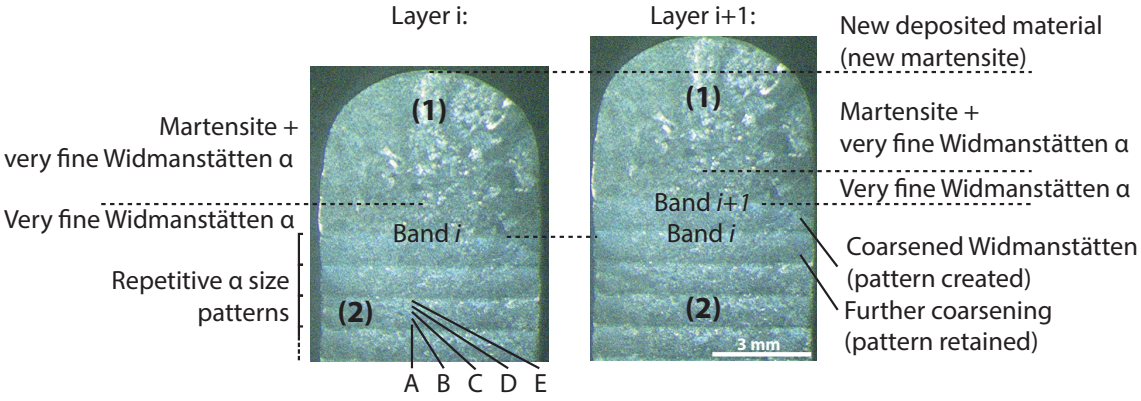

(a) Microstructure observed before and after the deposition of a new layer, and their locations within the components

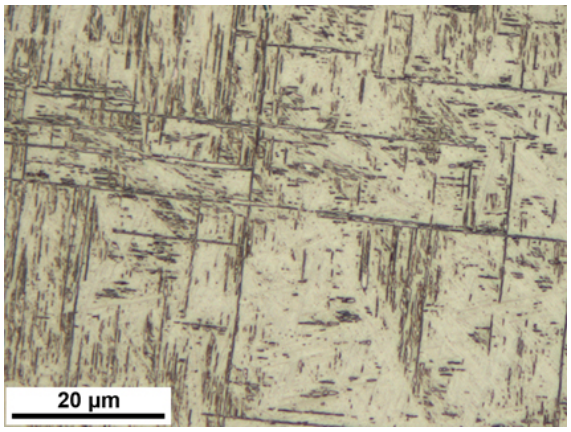

(b) Optical microscopy image of martensite observed in the top of the sample rolled at 75 kN, indicated by 1) in Figure 3.5a

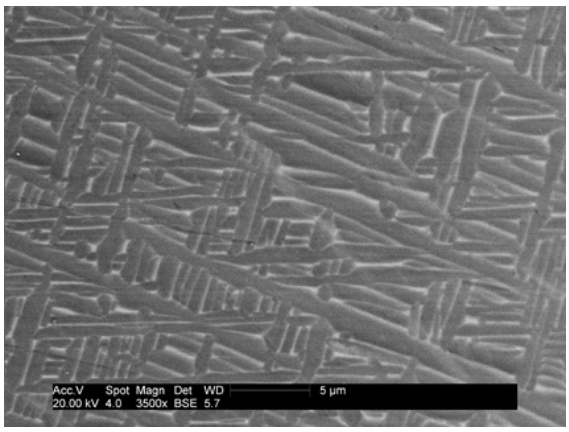

(c) SEM image of the Widmanstätten microstructure observed in the rest of the sample, indicated by 2) in Figure 3.5a

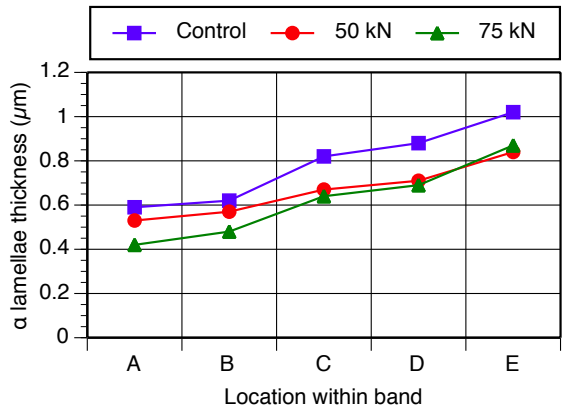

(d) Plot of the α thickness vs. the locations showed in (a)

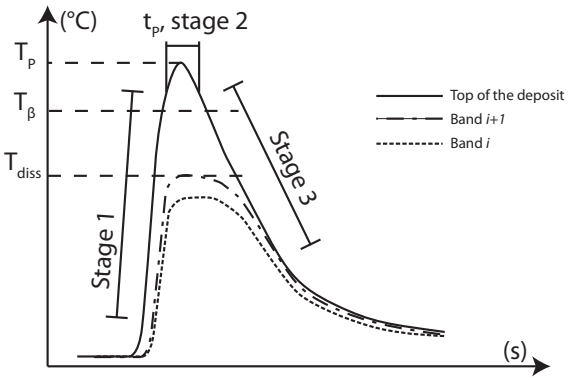

(e) Schematic of cooling curves for top of deposit, first band, and area immediately below

Figure 3.5: Microstructure analysis of top of WAAM wall.

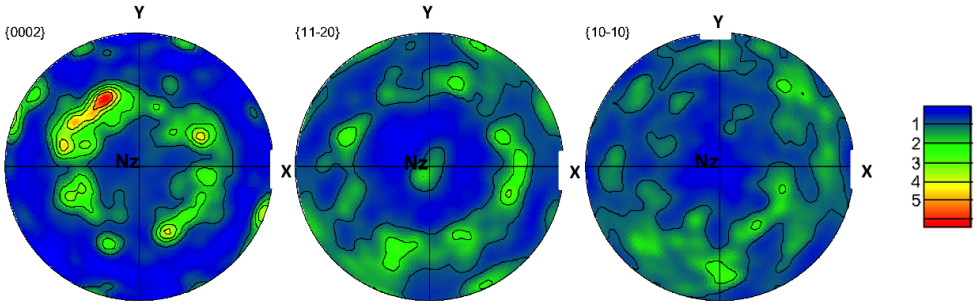

(a) Control

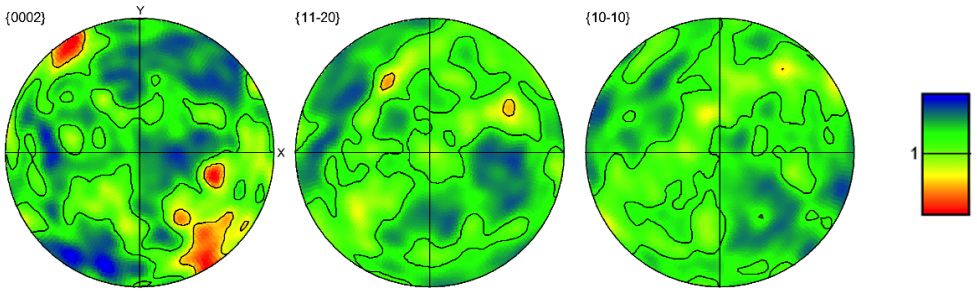

(b) Profiled roller at 50 kN

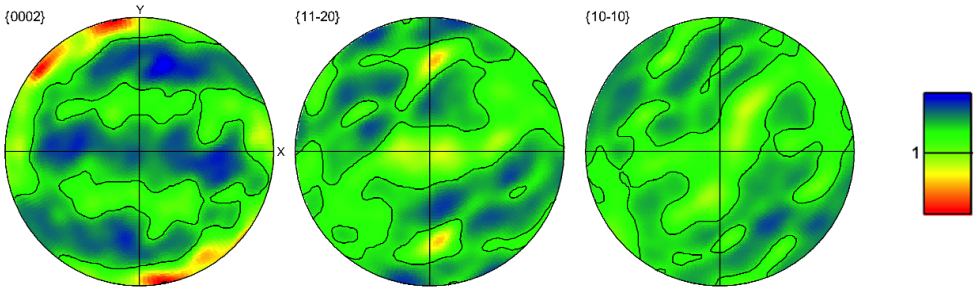

(c) Profiled roller at 75 kN

Figure 3.6: α texture for control and rolled samples (Antonysamy, 2012).

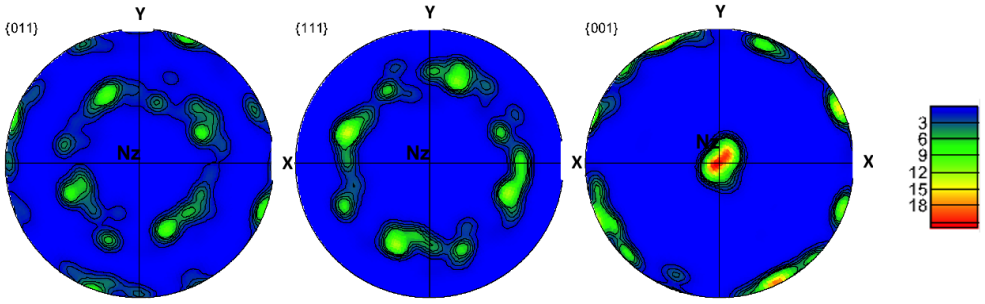

(a) Control

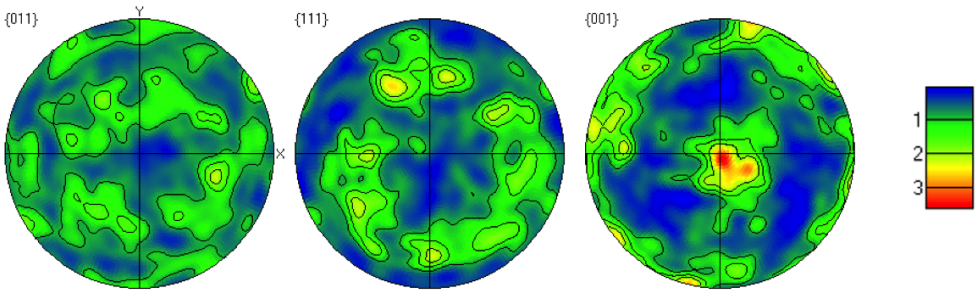

(b) Profiled roller at 50 kN

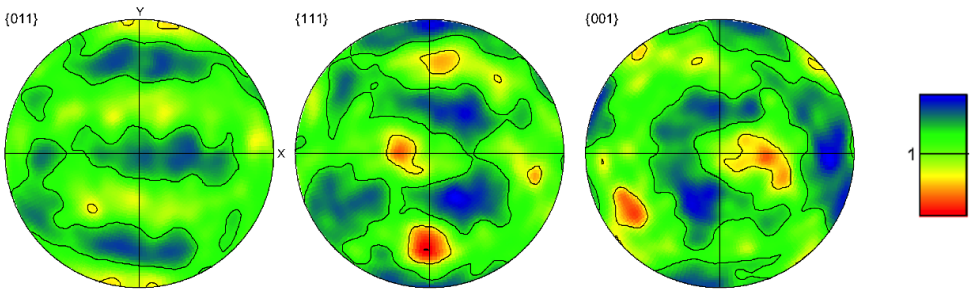

(c) Profiled roller at 75 kN

Figure 3.7: Reconstructed prior β grains texture for control and rolled samples (Antonysamy, 2012).

3.4.1 Fundamental study

The microstructures of the samples from the fundamental study are shown in Figure 3.8, images (a) to (g). (b) and (d) show the samples whose last layer was rolled only; due to process noise it is impossible to determine exactly the extent of the lateral plastic deformation induced by the rolling step (Figure 3.9). However, it is possible to identify the shift in the Z coordinates of the top band (highlighted by the red line), as well as a modest reduction in height. Apart from the deformation induced by the roller, the microstructure of these samples was relatively unchanged. The samples that had a subsequent layer deposited (Figures 3.8a,e) had a significantly different microstructure. There were three different regions which are labelled with 1, 2 and 3 in Figures 3.8(f,g): the first, closer to the top of the deposit (1), exhibited columnar prior β grains aligned with the Z axis. These grains grew from the ones within the region below (2), which was characterised by a refined equiaxed microstructure. The third region had long columnar prior β grains that were identical to those observed in the control. The microstructure of the α phase within these regions was also significantly different. Within regions (1) and (2) the microstructure was predominantly martensitic, while in region (3) the microstructure was the Widmanstätten microstructure that is observed in the bulk material.

The location of the points 5.6 mm and 6 mm from the top surface of the sample rolled at 75 kN with a subsequent deposited layer are shown in Figure 3.8f: the first point corresponds to the boundary between region 2 and 3, while the second corresponds to the first horizontal band in the deposited microstructure. The peak temperature of these points is shown in Figure 3.8h: the first had a peak temperature of 780 °C and a cooling rate from 700 °C to 400 °C of 8.4 °C s^{-1}; the second, after removing the three outliers[3] at 589 °C, 990 °C and 1068 °C had an average peak

[3]An outlier is an observation which is clearly deviating from the rest of the data set. Grubbs (1969) concluded it is acceptable to reject measurements on physical grounds. In such cases the median can be a better estimator

temperature of 740 °C[4] with a standard deviation of 26 °C, and a similar cooling rate from 700 °C to 400 °C of 7.4 °C s^{-1}. In Figure 3.8h the temperature distribution of the first band was based on six-point averages calculated every five seconds. Error bars were calculated in the same way. Please note that without removing the outliers the average peak temperature would have been 788 °C[5] with a standard deviation of 148 °C.

Figure 3.10 shows higher magnification EBSD images, focused on the areas marked with (2) and (3) in Figures 3.8(f,g). The EBSD scans were done on the same samples used for the optical micrography images and it was possible to identify the same grain boundaries. This figure is helpful in highlighting the transition from the columnar, highly textured area constituting the bulk of the deposit to a moderately less textured one, which still showed some columnar grains (although with a lower aspect ratio). Further above, the texture was completely randomised and the microstructure fully equiaxed, as evidenced by the colouring scheme. Finally, there was another columnar region at the top of the deposit.

[4]Median equal to 738 °C

[5]In this case the median was 739 °C which is much closer to the average temperature without outliers

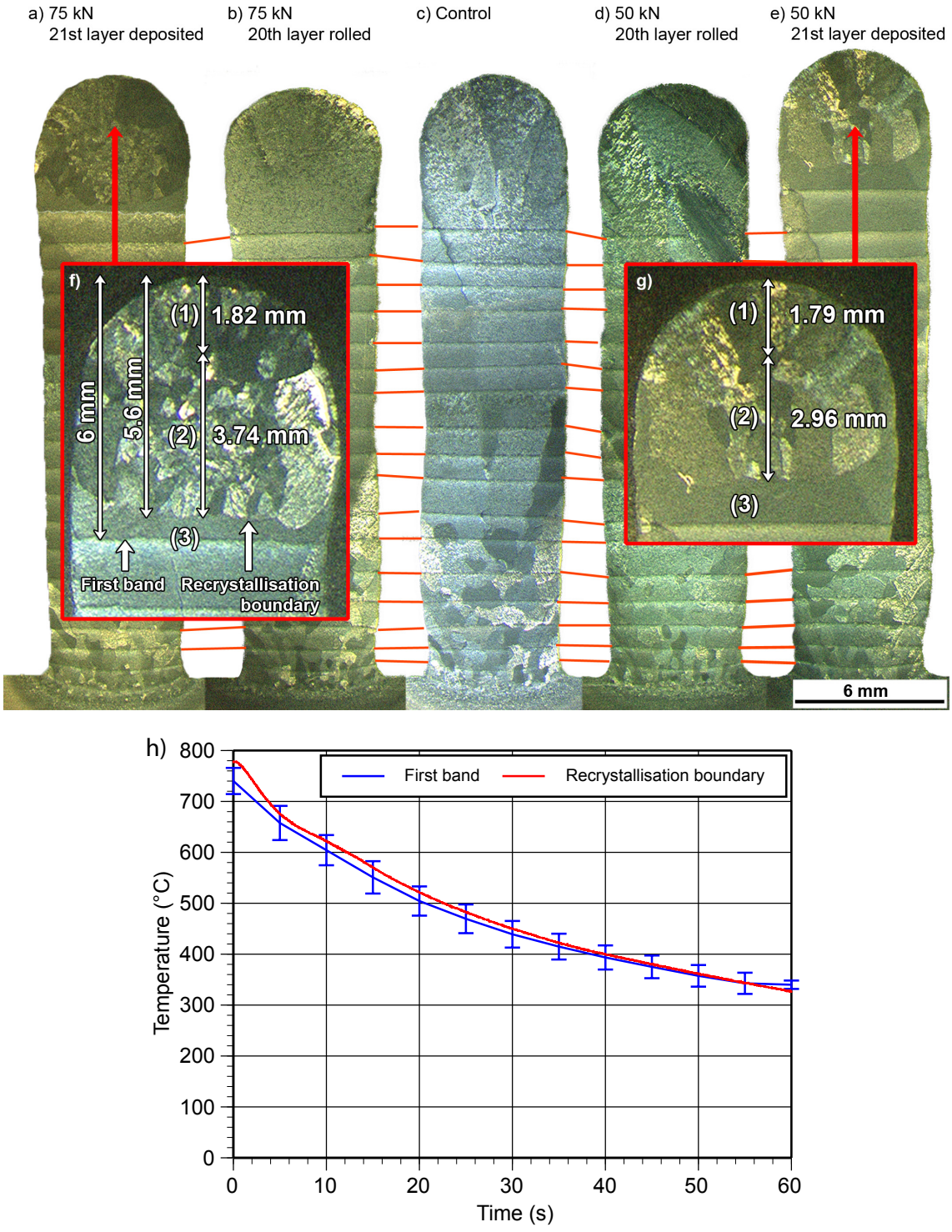

Figure 3.8: Optical micrography images from the fundamental study samples rolled with loads of (a) 75 kN, (b) 75 kN with subsequent deposited layer, (c) control, (d) 50 kN and (e) 50 kN with a subsequent deposited layer. (f) and (g) higher magnification of recrystallised areas for samples rolled at 75 kN and 50 kN, respectively, with subsequent deposited layers; (h) thermal history at 5.6 mm and 6.0 mm below the top of the sample rolled with 75 kN with a subsequent deposited layer.

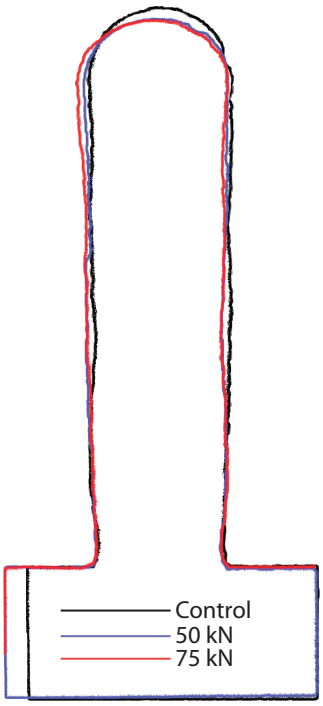

Figure 3.9: Overlap of contours of control, 50 kN and 75 kN specimens (only last layer rolled).

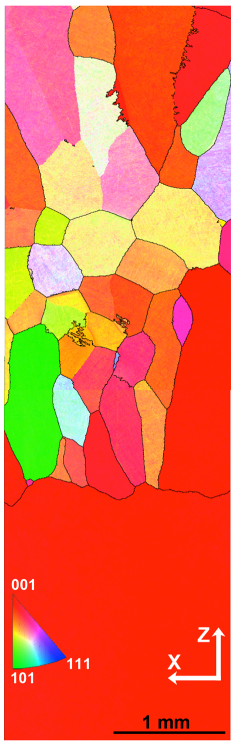

(a) 20th layer rolled at 50 kN after depositing the 21 layer

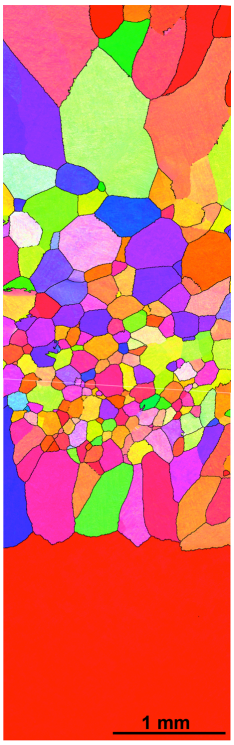

(b) 20th layer rolled at 75 kN after depositing the 21 layer

Figure 3.10: EBSD images of top of fundamental study specimens.

3.5 Discussion

3.5.1 Recrystallisation of prior β grains

The remarkable grain refinement observed in the rolled specimens, which is proportional to the applied load, is probably one of the main achievements of the present research. In fact, epitaxial grain growth, which results in large columnar grains in the direction of the heat flow, i.e. in the positive Z direction, is still one of the major drawbacks of AM technology when applied to titanium alloys.

The prior β grain refinement is due to recrystallisation. Given that recrystallisation is activated thermally and driven by stored energy (Humphreys and Hatherly, 2004, p. 1), the reduction in grain size can be explained by:

1. Plastic deformation of metals, such as rolling, introduces stacking faults, points defects, dislocations and twins, which represent the fraction of the mechanical energy that is retained (Cotterill and Mould, 1976, p. 15). However, approximately 99% of the mechanical energy is released in the form of heat during deformation (Humphreys and Hatherly, 2004, p. 12). A minimum strain of 1 % to 3 % is required for recrystallisation to happen (Humphreys and Hatherly, 2004, p. 222), a condition satisfied in the present case (see Table 5.1 on page 131).

2. While rolling induced the accumulation of stored energy, the deposition of a new layer provided the heat necessary to trigger recrystallisation. The minimum stored energy and temperature required for recrystallisation are material-dependant quantities. In situations in which different annealing temperature can be chosen, the recrystallisation temperature is the one at which the material is 50% recrystallised in 1 hour (Humphreys and Hatherly, 2004, p. 218). The recrystallisation temperature in commercially pure titanium is 646°C to 669°C, well below its β-transus temperature of 882°C (Contieri et al., 2010). In terms of heat treatment, for commercially pure titanium in the ASM

Handbook: Heat Treating (1991, p. 2051) an annealing temperature of 705 °C to 790 °C and time of 1 h to 4 h are recommended. In the specific case of the Ti–6Al–4V alloy, the recrystallisation temperature ranges from 535 °C to 830 °C, and is approximately one third to one half of the melting temperature (Humphreys and Hatherly, 2004, p. 4). This temperature, which is also dependant on the strain, decreases as the strain increases (Humphreys and Hatherly, 2004, p. 221). The peak temperature, particularly near the deposition torch, greatly exceeds that required for recrystallisation. In fact, temperatures up to 1000 °C are achieved even millimetres away from the melt pool, where the temperature is above the melting point.

3. The temperature greatly affects the rate of recrystallisation (Humphreys and Hatherly, 2004, p. 229), and it is actually more significant than time. In fact, an increase of only 10 °C will produce the same results as doubling the annealing time (Dieter Jr., 1961, p. 155). Therefore, in spite of the very short duration of the thermal cycle during WAAM, it is possible to achieve a fully recrystallised structure due to the high temperature experienced during processing.

In the present case, the dominant cause of the reduction in prior β grain size is the rolling load, and not the thermal profile. A higher strain results in a larger amount of stored energy and ultimately in a larger amount of effective nuclei (Humphreys and Hatherly, 2004, p. 221). The thermal profile will remain similar for the three samples due to identical deposition parameters being used. There will be a minor effect from the wider deposit which will cause a slight increase in cooling rate, however this is unlikely to significantly affect the microstructure.

Please note that investigations of static recrystallisation on titanium are limited to commercially pure titanium, a much simpler phenomenon due to the absence of a second phase. In the literature, it seems that only Xue et al. (2012) studied static recrystallisation of Ti–6Al–4V up to temperatures of 880 °C. More research has

been performed on dynamic recrystallisation (happening during hot deformation); however this is not relevant to the present case, in which the part was allowed to cool to room temperature before performing the rolling pass.

At the top of the deposit there was a region with columnar prior β grains which extended approximately 2 mm (see optical microscopy images in Figure 3.3 and Figure 3.8). Even though this layer was rolled, it was not followed by another deposition step, so recrystallisation couldn't be triggered. Although not measured, the boundary with the equiaxed material underneath may have corresponded closely to the region that was molten during the deposition of the last layer; the solidifying grains grew epitaxially from the material underneath, which was largely recrystallised.

Finally the results with the flat roller demonstrated a non-uniform refinement of the prior β grain size which was less refined toward the side walls. As seen in Figure 3.3d and Figure 3.3e, the flat roller caused a significant amount of flattening of the deposited material. Consequently the strain induced in the material was likely to be concentrated around the centre of the deposit. Because of the relationship between strain in the material and prior β grain size (please see Table 3.3), the concentration of the strain in the centre of the deposit resulted in greater prior β grain refinement in this region. The effectiveness of the flat roller is particularly beneficial, as the flat roller is characterised by practical advantages such as:

- the independence of the roller width from the wall width, which means one roller could be used for a variety of WWs;
- the capacity of rolling intersections and corners, features commonly present in WAAM parts;
- improved top surface profile for subsequent deposition;
- potential use of in-process inspection, which thus far requires flat surfaces.

The demonstrated relationship between rolling and prior β grain refinement could be investigated further, and used to tailor or predict the prior β grain size as a function of the rolling load.

3.5.2 Fundamental study

In the fundamental study, the temperature at the recrystallisation boundary (5.6 mm from the top, see Figure 3.8h) was 780 °C, well below the β-transus temperature and the β phase recrystallisation temperature mentioned in Seshacharyulu et al. (2000). There are errors in this measurement due to precise placement of the thermocouple and the contact resistance between the thermocouple and the material, however this should have been taken into account because the temperature measurements were repeated three times. The temperature at which recrystallisation happens is thought to depend on the amount of strain present in the part (as described in section 3.5.1 on page 99), therefore the temperature measured at the recrystallisation boundary makes sense only if related to the rolling load and to the width of the part. A different width, or a different rolling load, would have resulted in a different strain, hence the temperature required for recrystallisation would have been different. In fact, the change in the position of the boundary when rolling at 75 kN instead of 50 kN (see Figure 3.8f vs. Figure 3.8g), suggests that the temperature for recrystallisation is dependent on the amount of strain rather than the thermal profile, which was the same for the two samples, regardless of the rolling load.

3.5.3 α phase

3.5.3.1 Origin of visible "bands" in microstructure

Bands can be identified in all deposits; these features were generated by an α phase of different thickness, resulting from the repeated heat cycles associated with the deposition of each layer. Kelly and Kampe (2004b) discussed the possibility of a chemical effect given by the segregation of aluminium and vanadium during the phase transformation, referred to as transverse solute banding, however the present analysis will focus on the thermal aspect. As shown in Figure 3.5e, a typical thermal cycle can may be simplified into three main sections: heating (stage 1), a period t_P

when the material is around the peak temperature T_P (stage 2), and cooling (stage 3). It appears that there is little difference in cooling rate in the top 4 mm to 6 mm of the deposited structure, i.e. irrespective of the peak temperature and distance from the heat source the average cooling rate on the tail (stage 3) is similar. This is confirmed by the experimental measurements shown in Figure 3.8h. Indeed the cooling rate measured at the two locations ($7.4\,^{\circ}\mathrm{C\,s^{-1}}$ to $8.4\,^{\circ}\mathrm{C\,s^{-1}}$) is sufficient to produce at least a partially martensitic microstructure (Gil et al., 2001). Looking at the area between the top of the deposit, and the band i which appears during the deposition of layer i (Figure 3.5a), nearer to the deposition heat source both t_P and T_P are such that martensite can be produced (Figure 3.5e), and martensite is found in the top of all deposits (Figure 3.5b). Further from the deposition heat source, thermal conditions are such that very fine Widmanstätten is generated. Upon deposition of a new layer $i+1$ which creates the band $i+1$, martensite will be produced in the newly deposited material and immediately below. Closer to, but above the band $i+1$ there is sufficient temperature and time during stage 2 to transform the martensitic α into very fine Widmanstätten. In fact, during *annealing* according to Lütjering and Williams (2007, p. 29) martensite decomposes to $\alpha+\beta$ either by β particles at dislocations, or β layers between α boundaries. In the area between the bands i and $i+1$, coarsening of the previously very fine Widmanstätten occurs, and the pattern shown in Figure 3.5d is generated. Below band i no significant microstructural changes occurs, apart from a possible coarsening of α lamellae which retain the repetitive pattern anyway.

The temperature of the point that is associated with the top band in the microstructure (6 mm below the top of the wall) was 740 °C. This point appears to be related to the α dissolution temperature of 748 °C (Kelly and Kampe, 2004a from Katzarov et al., 2002). However such an agreement between the measured and the α dissolution temperatures might have been just coincidental. Elmer et al. (2004) demonstrated that critical temperatures such as β-transus vary according to heating

rates, which are responsible for the kinetics of the $\alpha \rightarrow \beta \rightarrow \alpha/\alpha'$ transformation. Heating rates are not shown in Figure 3.8h as, firstly, they would have been the same for all the curves, the points being at the same location; and, secondly, they would have not provided any valuable information given that heating rates in other points of the deposited structures were not measured, and no comparison could have been made. Elmer et al. (2004) showed that for high heating rates (like the ones experienced in welding and AM), significant superheating (up to 300 °C) might be necessary to observe certain transformations. In other words, different welding parameters (which would have given different heat inputs, similarly to what was discussed in Elmer et al., 2003), and consequently also different walls geometries, would have led to different heating rates and ultimately in changes in the temperature responsible for the observed combination of very fine Widmanstätten and martensite. In conclusion, what really matters is that the measured temperature was high enough to transform at least some β to α, and the cooling rate was high enough to subsequently generate very fine Widmanstätten and martensite upon cooling.

3.5.3.2 Reduction of α phase thickness

The addition of deformation introduced a small but measurable reduction in the overall average size of the α lamellae (Figure 3.5d). There are three possible reasons for this observation. Firstly it could be a consequence of the larger number of grain boundaries. According to Lütjering and Williams (2007, pp. 32–33), in the case of basketweave or Widmanstätten microstructures, α colonies nucleate at the grain boundaries and grow perpendicular to them. When α colonies collide with each other, and therefore cannot grow further, additional colonies start nucleating perpendicular to the side of those which have already developed. In the case of the rolled samples, there were more α phase nucleation sites due to the larger number of prior β grains. Therefore lamellae growth is hindered by their own competition, hence the overall size of the lamellae decreases with the increasing rolling load.

However there is a large difference in the scale of the prior β vs. the α lamellae thickness (100µm vs. $<$ 1µm) so the influence of this may be limited.

An alternative explanation is that deformation influences the transformation of martensitic α to Widmanstätten providing more nucleation sites for the transformation which leads to a finer microstructure.

Finally, recrystallisation occurs at temperatures comparable to those used to achieve a fully equiaxed microstructure, in which case Lütjering (1998) explained that the α phase equilibrium volume fraction is large enough to stimulate the growth of the α phase from the deformed lamellae.

3.6 Summary

In this chapter it has been demonstrated that:

- Due to the recrystallisation that occurred when the previously deformed layer heated during the deposition of a new layer, high-pressure rolling induced:
  - significant prior β grain refinement,
  - a modification of the prior β grain structure from strongly columnar to equiaxed,
  - a reduction in the overall thickness of α phase lamellae,
  - a randomisation of the α phase texture;
- The flat roller, which has significant practical advantages, provided similar reductions in distortion and prior β grain size, and may be the preferred choice for commercial exploitation of the process.

A fundamental study was performed to understand the microstructural changes that occurred during the process. The last layer of an unrolled control sample was rolled after which a new layer was deposited. The size of the recrystallized region was influenced by the load and hence the extent of deformation in the material. In

addition the temperature of the recrystallised region boundary and first microstructural band were 780 °C and 740 °C respectively, well below the β-transus and very close to the α dissolution temperature of 748 °C.

In conclusion, rolling is beneficial from a microstructural point of view as it proves to be a simple but effective way to eliminate columnar prior β grains and produce a uniform equiaxed microstructure in titanium AM structures. This might have significant implications in terms of mechanical properties, which will be investigated in the following chapter.

Acknowledgements

The support of Jack Donoghue for EBSD images shown on pp. 90 and 98 was fundamental and his help, contribution and kindness are acknowledged. Andrew Dyer and Dr. Xianwei Liu's assistance during optical and scanning electron microscopy image analysis was greatly appreciated.

Chapter 4

Effect of rolling on mechanical properties of WAAM parts

This chapter contains material from the following articles:

Martina, F., Williams, S., Colegrove, P.A., 2013. Improved microstructure and increased mechanical properties of additive manufacture produced Ti–6Al–4V by interpass cold rolling, in: 24th International Solid Freeform Fabrication Symposium, Austin, Texas, USA. pp. 490–496.

Martina, F., Colegrove, P.A., Williams, S.W., Meyer, J., 2014b. Tensile strength, elongation and microhardness of as-deposited and interpass rolled Wire + Arc Additive Manufacturing Ti–6Al–4V components. Journal of Materials Processing Tech. (submitted).

Ding, J., Colegrove, P.A., Martina, F., Williams, S.W., Wiktorowicz, R., Palt, M., 2014. Development of a laminar flow local shielding device for Wire + Arc Additive Manufacture. Journal of Materials Processing Tech. (submitted).

4.1 Context

Titanium Wire+Arc Additive Manufacturing (WAAM) deposits are characterised by anisotropic mechanical properties, which are also lower than the wrought alloy. Following observations of the microstructural changes introduced by rolling, discussed in the previous chapter, this chapter evaluates the effect of the refined

microstructure on mechanical properties.

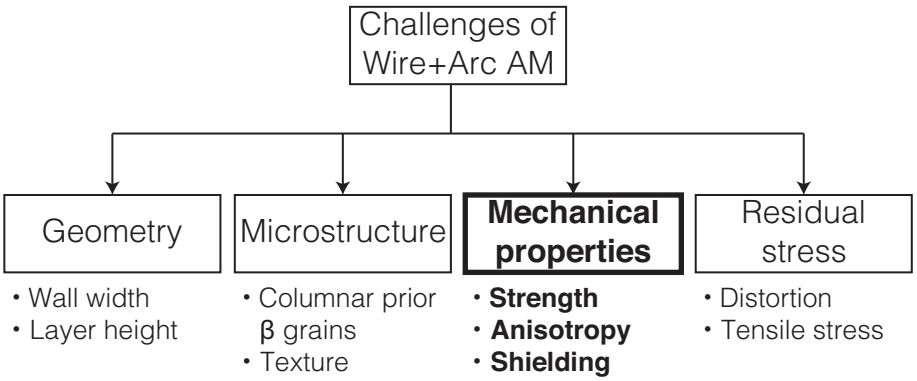

Figure 4.1: Project map. In bold the work package object of the present chapter.

4.2 Introduction

Many authors, including Baufeld et al. (2009), Wang et al. (2013) showed that in Ti–6Al–4V Additive Manufacturing (AM) components prior β grains grow parallel to the thermal gradient and are highly textured, leading to anisotropic mechanical properties. Strength is higher in the horizontal (X) direction, while elongation is better vertically (Y).

In chapter 3, high-pressure interpass rolling was used to produce a much finer, texture-free microstructure. In this chapter, the effect of high-pressure rolling on mechanical properties is assessed, to establish whether rolling produces isotropic and/or improved mechanical properties.

As discussed extensively in chapter 1, section 1.2.5.2 on page 20, preventing oxidation of AM deposits, particularly titanium oxide, is of fundamental importance.

While oxygen is used as an alloying element to increase strength and elastic modulus, too high a concentration can lead to embrittlement. Consequently, most high temperature processing is carried out within a shielded environment, which is achieved either by filling a chamber with argon, or by using a vacuum (which is necessary for Electron Beam Melting (EBM)).

One of the targets for WAAM is to deliver high quality components deposited using local shielding devices only. It is therefore paramount to understand exactly the dynamics of oxygen pickup, by comparing the quantity of oxygen present in a controlled atmosphere during deposition, to that measured in the part once the building process is finished.

Traditionally, colour inspection tools are used to assess the oxidation extent. Talkington et al. (2000) developed a methodology to relate colour to oxygen content as a quality control tool, glossy silver being the best and white or brushed the worse. Li et al. (2005) argued the lack of reliability of the inspection tool, because the colour sequence repeats itself as oxygen content and TiO_2 layer thickness increase. They suggested hardness was a much better proxy; hence this will be used to evaluate whether a correlation between oxygen content in the part, oxygen in the atmosphere, and microstructural changes exists.

4.3 Experimental procedures

4.3.1 Mechanical properties

Parts were built using the equipment and process parameters described in section 3.3 on page 85. A control specimen, unrolled, was built alongside two more parts produced with the profiled roller (Figure 3.2c on page 87) at 50 kN and 75 kN. Test coupons were extracted randomly both horizontally (X direction) and vertically (Z direction) (see Table 4.1). Tensile coupons were coated with graphite spray paint; within their total parallel length of 27 mm, a gauge length of 24 mm was marked with two pieces of reflective tape. The extension of the gauge length was monitored by a laser extensometer; the change in length was used for the calculation of elongation. The cross section of the gauge was 6 mm by 4 mm. Testing was carried out in accordance with BS EN 2002–1:2005 (2005); the speed of the test was 0.1 mm min^{-1}; full details regarding specimen location within the wall, as well as coupon dimensions

are provided in appendix B.

Table 4.1: Number of tensile test specimens extracted.

	Control	50 kN	75 kN
Horizontal	5	3	2
Vertical	4	3	3

Three smaller walls were build for microhardness evaluation (control, rolled at 50 kN, rolled at 50 kN), made of 20 layers each, with a total length of 370 mm and a rolled length of 300 mm. Microhardness was measured for all the samples, along the wall centreline in the Z direction. The measurements started 2.5 mm into the base plate to assess the hardness of the base and heat affected zone and were continued to the top of the wall. The spacing between measurements was 0.5 mm; the load was 500 g and the indentation time was 15 s. It was not possible to execute the same number of indentations for all the samples, due to the difference in the wall height.

4.3.2 Oxygen pickup

Four linear structures were deposited onto a $300\times150\times7$ mm^3 Ti–6Al–4V substrate in a rigid, sealed chamber. Unlike the previous work, Plasma Arc Welding (PAW) WAAM was used; process parameters are shown in Table 4.2.

Table 4.2: Deposition parameters.

Wire feed speed	$2.4\,\mathrm{m\,min^{-1}}$
Travel speed	$4.5\,\mathrm{mm\,s^{-1}}$
Current	160 A
Plasma flow rate	$1\,\mathrm{l\,min^{-1}}$
Gas flow rate	$10\,\mathrm{l\,min^{-1}}$
Torch stand-off	8 mm

Each structure was 250 mm long and made of 20 layers. Argon and oxygen bottles were both connected to a gas mixer, which supplied a constant gas flow to the chamber. The ratio between the gases was changed so as to have different, but consistent, levels of oxygen when manufacturing each wall. These levels were ca.

30 ppm, 1000 ppm, 2000 ppm and 4000 ppm. No trailing shield was used, hence the newly deposited material was exposed to the oxygen contained in the controlled atmosphere as the torch had passed. The wire chemical composition can be found in Table 4.3. Oxygen levels were measured according to ASTM E1409 - 13 (2013).

Table 4.3: Chemical composition of Ti–6Al–4V wire used in the experiments.

Ti	Al	V	Fe	O	C	N	H	TOE	Y	Others
Bal.	6.08	4	0.18	0.16	0.035	0.011	0.0017	<0.2	<0.001	<0.05

Cross sections were extracted from each wall and microhardness was measured along the centreline of the components, starting 2.5 mm from the bottom of the base plate to assess the hardness of the base plate and of the interface between wall and base plate. Measurements were continued to the top of the wall, for a total of 19 points. The spacing between measurements was 1 mm; the load was 500 g and the indentation time was 15 s.

4.4 Experimental results

4.4.1 Tensile properties

Average tensile test results are shown in Figure 4.2. A full set of strain-stress curves is given in appendix B on page 175. In Figure 4.2, the control specimens (zero load) show scattered behaviour in the horizontal direction, especially with regards to the elongation, which ranged from 11% to 18%. The vertical direction was characterised by lower standard deviation and more consistency in both strength and elongation.

For the rolled specimens the increase in proof strength and ultimate tensile strength was demonstrated. The mechanical performance of the rolled specimens was always higher than the unrolled ones, in both horizontal (X) and vertical (Z) directions, except for the elongation which is maximum in the unrolled, vertical case. This agrees with that already observed by Wang et al. (2013). In the specimens

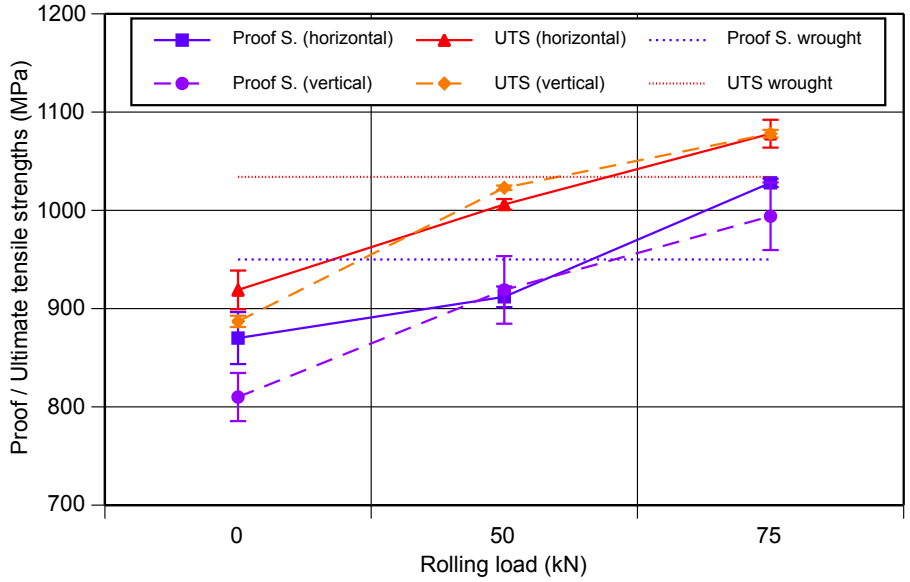

(a) Proof and ultimate tensile strengths

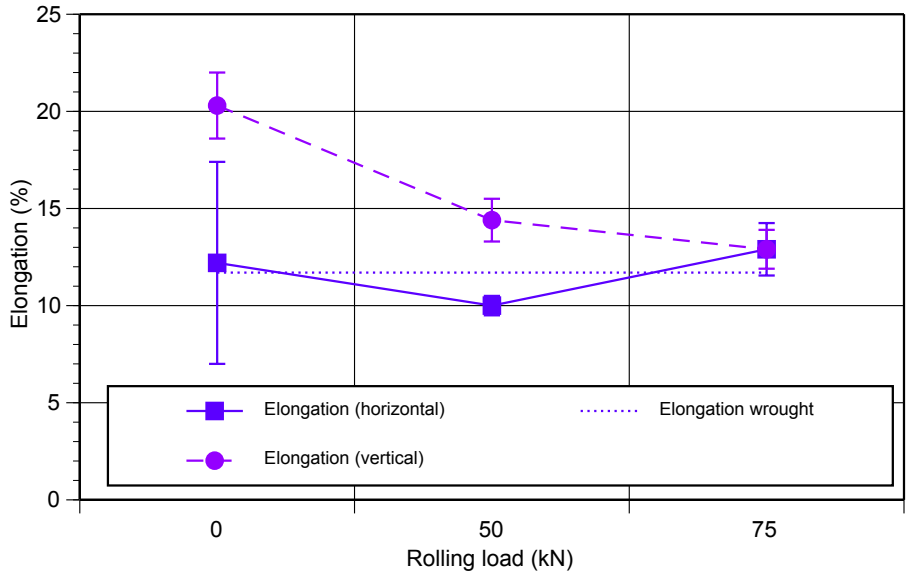

(b) Elongation

Figure 4.2: Tensile test results for control and rolled specimens (error bars indicate standard deviation).

rolled at 75 kN all properties exceeded the wrought Ti–6Al–4V (as tested by Wang et al., 2013), although the latter was characterised by a bi-modal microstructure.

In the case of the unrolled specimen (control) a large difference existed between the two directions, especially with regard to the elongation. The difference in the properties between the two directions was reduced for the specimens rolled at 50 kN, and minimum for the 75 kN one (Figure 4.2b). Hence the sample rolled at 75 kN load can be considered as isotropic. Furthermore, in the unrolled sample the proof strength in the vertical direction was below the minimum specification (ASTM B265 – 09a, 2009). Rolling enabled the component strength to be above that required by the standard, without compromising the elongation.

4.4.2 Hardness

The hardness values are plotted in Figure 4.3. The average hardness values of the specimens rolled at 50 kN and 75 kN were greater than the control specimen and reflect the improvements observed in the tensile properties. The new values fell outside the 95% confidence interval calculated around the average hardness of the control specimen, consequently the differences are significant and are unlikely to be due to statistical variation. The difference between the hardness of the samples rolled with the profiled and flat rollers is not statistically significant.

4.4.3 Oxygen pickup

Please note that, differently from the previous section, whose samples were produced by Tungsten Inert Gas (TIG) WAAM and rolled, the hardness values presented in this section are related to deposits produced with plasma WAAM; therefore a direct comparison cannot be made. The oxygen and hardness for different contamination levels in the enclosure are shown in Figure 4.4. For the hardness measurements the error bars indicate the 95% confidence intervals. There was no statistically significant difference in the hardness for the different contamination levels even though

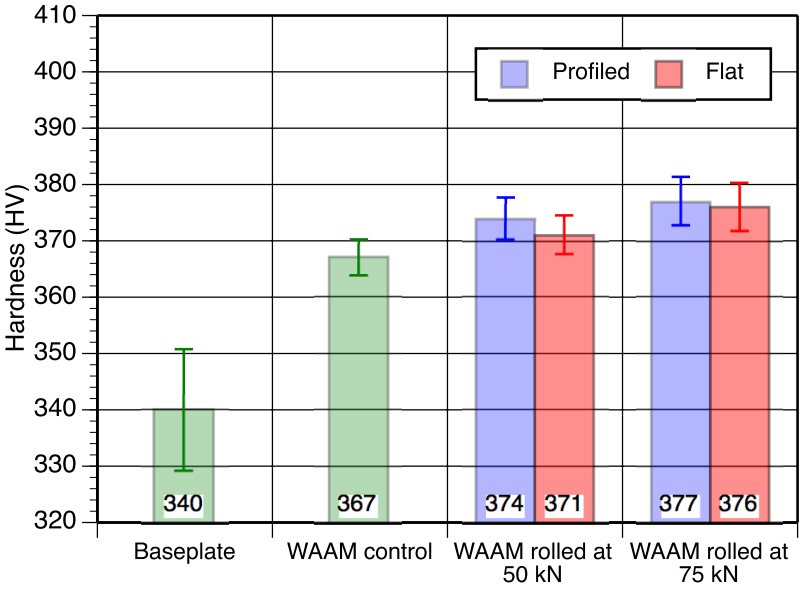

Figure 4.3: Hardness of Ti–6Al–4V produced with TIG WAAM vs. rolling load (error bars indicate 95% confidence interval of the mean).

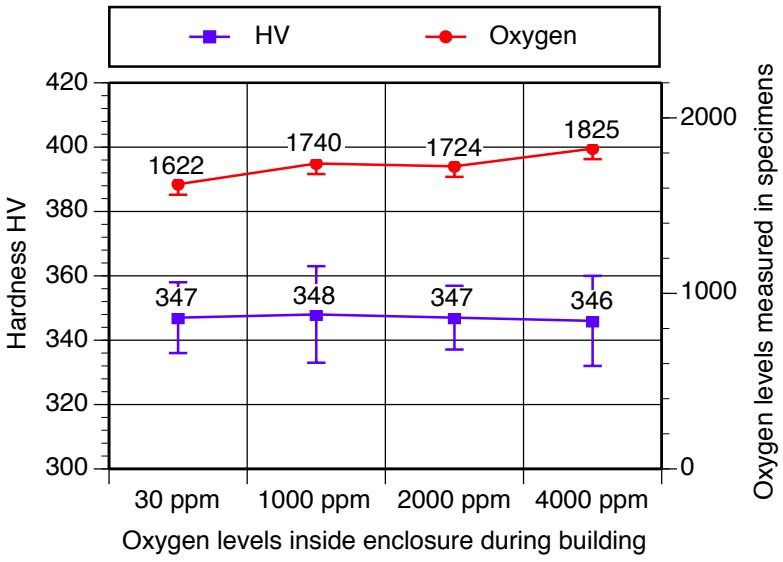

Figure 4.4: Hardness and oxygen content of specimens built in different atmospheric conditions with PAW WAAM.

there was an increased amount of oxygen in the deposit. The average hardness measured on this set of samples was 347 HV, a lower value than the one reported in Martina (2010) for PAW WAAM of 387 HV.

The amount of oxygen detected in each sample ranged from 1622 ppm to 1825 ppm and was marginally affected by the quantity of O_2 present in the atmosphere

during deposition: when building with 4000 ppm in the atmosphere, the increase in part's oxygen was only 200 ppm, compared to when there was negligible O_2 conditions in the surrounding atmosphere. Please note for the O_2 measurements the error bars indicate ±60 ppm.

4.5 Discussion

4.5.1 Hardness and strength

The increase in microhardness and strength due to rolling may be attributed to two causes. The first is the refinement of α lamellae: a reduction in α lamellae size corresponds to an increase in most of the mechanical properties, including hardness (Lütjering, 1998). The second is the work hardening induced by the interpass rolling steps, which introduce a large amount of dislocations in the part. One could argue that the subsequent heat treatment brought by the deposition of a new layer could anneal the hardened material. However, there is a competition between strain introduced by each rolling step, and annealing performed by each layer deposition. Imagine rolling the top of a wall, and then depositing a new layer: rolling introduces strain up to a certain depth, and the deposition of a new layer anneals the material up to a certain depth. This depth will be dependent upon both the rolling load and the temperature distribution in space and time, as shown in the fundamental study (please see p. 95). The peak temperatures are progressively lower for points further from the top of the wall, due to the increased distance from the heat source. If the depth of the strain was larger than the depth of the annealing treatment, it might be that a number of dislocations and other crystallographic defects were left in the material, and accumulated. When attempting a 100 kN rolling load the specimen ruptured after seven layers; this might suggest that in this case the annealing process did not occur fully.

4.5.2 Elongation

With respect to the control sample, one could argue the gauge size was too small to include a sensible number of prior β grains, or, even worse, the gauge was smaller than a prior β grain; without grain boundaries acting as potential sources of failures, the elongation would be artificially large. This is definitely not the case, for the gauge is large enough to include enough prior β grains (see section 4.3). For instance, the gauge cross-section adopted for this research was four times larger than the one reported in Baufeld et al. (2009).

With regards to the scatter seen in the horizontal direction, it could be considered consistent with that already presented in Wang et al. (2013), who suggested that stress perpendicular to the prior β grain boundaries could result in shear and premature failure along the α_{GB}. Furthermore, defects and inhomogeneities could explain why in Wang et al. (2013) a specimen had a very early failure at 3% elongation. However, in the present research no early failure was seen and the presence of defects is excluded. Rather the large scatter is due to the very late failure of CHT5 specimen which broke at 18% elongation (see page 178). If this specimen was not included in the calculations, the standard deviation would be as low as 1.5.

As for the increase in elongation observed in some rolled specimens, three different factors must be considered: the amount of cold work, the reduction in prior β grain size, and the reduction in α colony size. The first two are known to have a detrimental effect on elongation, because of the increase in dislocation density and grain boundaries (that can act as source of failure); on the contrary according to Lütjering (1998) the third, i.e. the reduction in colony size, has a beneficial effect due to the reduction in slip length. In the following paragraphs, the effect and relative magnitude of each of these three factors will be discussed.

Extensive α colonies were not observed in this work, as the microstructure was mostly basket-weave. In this case, the slip length may correlate to the α lamellae thickness, rather than to the size of the α colonies, as each colony is made of very

few or even a single lamella (Figure 3.5c on page 92). In turn, the reduction in α lamellae thickness will produce the same effect as the reduction in α colony size, increasing the ductility according to the principles described in the work of Lütjering (1998). Indeed, the author stated that in fully lamellar microstructures, Ultimate Tensile Strength (UTS) is maximised in the presence of martensite, in which the slip length and the colony size coincide with the width of the single lamella. In his work, ductility showed a similar trend, i.e. it increased with a reduction in slip length, although it dropped dramatically for extremely high cooling rates (when martensite is produced).

In the horizontal direction, elongation decreased when rolling at 50 kN but then increased with a 75 kN load. This suggests that at 50 kN the negative contributions of cold work and the reduction in the prior β grain size were the dominant factors. However, when rolling at 75 kN the improvement in the elongation (compared to the control results) was probably associated with the reduction in the average α lamellae thickness, this being the dominant factor. In fact, α lamellae width is minimised for this load.

In the vertical direction, elongation always decreased with the load. This must be associated with the much greater reduction in prior β grain size observed along this direction. In fact, while the horizontal direction prior β grain size was reduced by one order of magnitude (from ca. 1 mm to ca. 100 µm), in the vertical direction the reduction is by two, some times three orders of magnitude (from ca. 100 mm to ca. 100 µm). Therefore, the contribution of this factor appears to be larger than either cold work or reduction in α thickness, thus leading to the observed decrease in elongation.

Furthermore, it is worth noticing that cold work normally results in an increase in strength at the expense of elongation (Dieter Jr., 1961, p. 148). If there was any cold work left in the system, surely it would be larger in the 75 kN specimen, given the higher strain. The fact that for this load the elongation increases in the horizontal

direction and decreases only marginally in the vertical direction, when compared to the 50 kN specimen, indicates that the cold work was the least important of the three factors, and mechanical properties are mainly driven by microstructural changes (reduction in both prior β grain size and α lamellae thickness).

Finally, it must be noted that while the strength of the control specimen in the present research is very close to that reported by Wang et al. (2013), the elongation they reported was approximately 14% in the vertical and 8% in the horizontal directions, much lower than 20% and 12% respectively, measured in the present research. This might be due to different deposition parameters which could result in slightly different final microstructures.

4.5.3 Oxygen pickup

The value provided by Martina (2010) was the average of four different specimens, which were also produced with different process parameters, and some difference between the two experiments was to be expected. A direct comparison in terms of heat inputs cannot be made. However, a deviation of 40 HV is significant and possibly related to the difference in cooling rates experienced when depositing inside an inert environment. Lower cooling rates result in a much coarser α lamellae structure, and ultimately in lower strength.

The insensitivity to atmospheric oxygen content suggests that the shielding provided by the torch was sufficient to protect the molten pool as well as the newly solidified hot material. Given a shroud diameter of 17 mm, and a travel speed of 4.5 mm, a point was shielded for roughly 4 s, in which 630 ml of argon were blown. Oxygen contamination becomes severe for temperatures above 550 °C; below this temperature the diffusion rates are low (Lütjering and Williams, 2007, p. 51). Without experimental values for the temperature at the surface of the part, it is difficult to infer the diffusivity rates. However, considering the high cooling rates experienced in WAAM; the exponential decrease of oxygen diffusivity with decreasing tempera-

ture (Lütjering and Williams, 2007, p. 46); and that the concentration of O_2 during deposition is much lower than the one in natural atmosphere, it is reasoned that the diffusivity rates were not sufficient to enable a significant O_2 pickup.

One could argue that the measurements were relative to the bulk of the material and ignored the surface of the sample. Provided that each layer was identical to the previous one (in terms of temperature, cooling rates, and consequently O_2 pickup behaviour) it should be considered that every time a layer was deposited the possibly oxidised surface of the previous layer became part of the bulk of the material, and was therefore included in the measurements, which were effectively average ones.

Please note that O_2 was present in the wire as an alloying element (the O_2 content of the wire is 1400 ppm, see Table 4.3) and therefore most of the O_2 in the final part comes from this source.

This finding may result in less stringent constraints on O_2 content inside chambers or tents, when building large parts. In such large volumes, reducing the O_2 content from 4000 ppm to near zero can be extremely time consuming, and these results indicate there are no clear benefits. Given that the requirements in the aerospace sector are very conservative, knowing that deposition may be carried out safely up to 4000 ppm of O_2 a limit of 2000 ppm could be imposed; this would give a safety margin of 100%. There would be repercussions also on local shielding devices, which could be designed with lower constraints in terms of size, flow efficiency, and depth of action.

4.6 Summary

In this chapter it has been demonstrated that high-pressure rolling:

- improves the mechanical properties, in terms of hardness, yield strength, ultimate tensile strength and elongation, due to the fine prior β grains structure, and reduced α phase thickness;

- has a limited work hardening effect, as the elongation decreases marginally;
- produces isotropic mechanical properties, which will facilitate design of WAAM parts;
- results in mechanical properties that are better than the wrought alloy.

Furthermore,

- WAAM of Ti–6Al–4V was insensitive to atmospheric concentrations of O_2 up until 4000 ppm and no significant pickup existed;
- hardness was not affected by the atmospheric concentrations of O_2 up to 4000 ppm.

Hence a limit of 2000 ppm would permit a safety margin of 100% and would be a suitable level for control of the process.

Acknowledgements

The content of oxygen in the deposited parts was measured by Dr. Matthew Thomas, R&D Engineer at Timet®. His contribution and that of his team are acknowledged.

Chapter 5

Effect of rolling on residual stress of WAAM parts

This chapter contains material from the following articles:

Colegrove, P.A., Coules, H.E., Fairman, J., Martina, F., Kashoob, T., Mamash, H., Cozzolino, L.D., 2013. Microstructure and residual stress improvement in wire and arc additively manufactured parts through high-pressure rolling. Journal of Materials Processing Tech. 213, 1782–1791.

Colegrove, P.A., Martina, F., Roy, M.J., Szost, B., Terzi, S., Williams, S.W., Withers, P.J., Jarvis, D., 2014. High pressure interpass rolling of Wire + Arc Additively Manufactured titanium components. Advanced Materials Research 996, 694–700.

Martina, F., Roy, M.J., Colegrove, P.A,, Williams, S.W., 2014. Residual stress reduction in high pressure interpass rolled Wire+Arc Additive Manufacture Ti-6Al-4V components, in: 25th International Solid Freeform Fabrication Symposium, Austin, Texas, USA. pp. 89–94.

Martina, F., Roy, M.J., Colegrove, P.A., Williams, S.W., Withers, P.J., Meyer, J., 2014c. Residual stress of as-deposited and interpass rolled Wire + Arc Additive Manufacturing Ti–6Al–4V components. Journal of Materials Processing Tech. (submitted).

5.1 Context

Residual stresses, which are manifested in component distortion, are a major drawback of Wire+Arc Additive Manufacturing (WAAM). High pressure rolling is investigated as a method to eradicate them. Because of the related plastic deformation, rolling changes the geometry of the deposit. These effects are captured in this chapter.

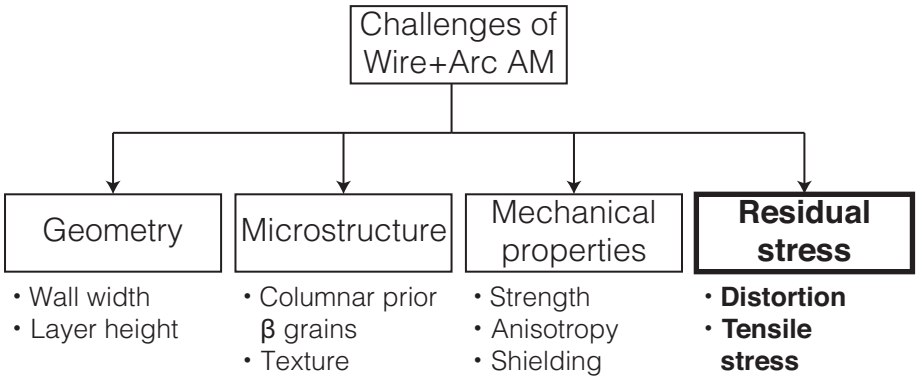

Figure 5.1: Project map. In bold the work package object of the present chapter.

5.2 Introduction

Ding et al. (2011) showed how WAAM components are affected by residual stress and distortion. These two issues are undermining the adoption of Additive Manufacturing (AM) in industry, and a range of research projects are underway targeting their mitigation. In welding, some of the investigated techniques include peening and rolling. According to Withers (2007) the former introduces a small plastic deformation which relieves tensile residual stresses, and forms compressive ones by a positive deformation in the in-plane directions. However, peening is characterised by a limited depth of influence, which is around 1 mm to 2 mm for carbon steels (Cheng et al., 2003). High-pressure rolling proved to have a much larger depth of action, and was successfully tried on steel WAAM structures by Colegrove et al. (2013). In this chapter, its effects on titanium WAAM deposits are evaluated; measurement

techniques include Neutron Diffraction (ND) and the Contour Method (CM) (Prime, 2001).

5.3 Experimental procedures

The experimental apparatus was as used for the investigations described in chapter 3 and chapter 4.

5.3.1 Evaluation of geometry and distortion

Baseplates were 405 mm long, 60 mm wide and 6 mm thick, and were clamped by countersunk bolts along each side of the plate. Six 20-layers walls were built: a "control" left in the as-deposited condition; three samples that used the profiled roller with loads of 50 kN, 75 kN, and 100 kN; and two that used the flat roller and loads of 50 kN and 75 kN.

Deposition started 20 mm from the end of the baseplate and stopped 15 mm from the other end giving a total wall length of 370 mm. The direction of deposition was always the same. Rolling began and ended 35 mm from the ends of the deposit.

During manufacture, the Layer Height (LH) from the baseplate was measured with a digital vernier at three points labelled M1, M2 and M3 (lh_{i,M_1}, lh_{i,M_2} and lh_{i,M_3}, respectively) which are indicated in Figure 3.2b on page 87, before and after rolling. The height of each layer (LH_i), overall Layer Height (LH) and standard deviation (σ) were calculated from:

$$LH_i = \overline{x_i} - \overline{x_{i-1}} = \left(\frac{1}{3}\sum_{j=1}^{3} lh_{i,M_j}\right) - \left(\frac{1}{3}\sum_{j=1}^{3} lh_{i-1,M_j}\right) \tag{5.1a}$$

$$LH = \mu = \frac{1}{16}\sum_{i=4}^{20} LH_i \tag{5.1b}$$

$$\sigma = \sqrt{\frac{1}{16}\sum_{i=4}^{20} (LH_i - LH)^2} \tag{5.1c}$$

The first four layers were excluded from the calculation of LH and σ because of the thermal effect of the baseplate which reduced the deposit Wall Width (WW) and increased the LH (Martina, 2010).

Average engineering strains were calculated from $\epsilon = {}^{(L_f - L_0)}/_{L_0}$, where L_0 is the initial length and L_f the final one. For the transverse (Y) direction, average WWs were used; for the normal (Z) direction, average LHs.

Strains on a layer-by-layer basis were calculated only for the LH (normal direction) by comparing the LH_i of the rolled specimens with the LH_i of the control one.

After completing each sample, maximum out-of-plane distortion was assessed by resting the parts on a flat surface, and measuring the distance between the bottom of the baseplate (at its short edge) and the flat surface.

Three sections were taken at the same points M1, M2 and M3 (Figure 3.2b); mounted into resin, ground, polished and etched with a solution of hydrofluoric acid for optical microscopy imaging. Adobe Photoshop CS4® (2008) was used to measure the WWs from these images.

5.3.2 Characterisation of residual stress

Titanium deposits were manufactured onto $250 \times 60 \times 6\,\mathrm{mm}^3$ Ti–6Al–4V substrates. Each linear deposit began and ended right on the edges of the substrate, and was made of 40 layers. Direction of deposition was alternated, i.e. a subsequent layer began where the previous one had finished. To avoid rotation of the torch, the wire was fed 90° to the direction of the travel, from the same side. The roller was profiled (Figure 3.2c), and three samples were built: unrolled, rolled at 50 kN and rolled at 75 kN.

5.3.2.1 Contour method

Residual stresses were measured with the CM at the University of Manchester. The specimen was cut via Electrical Discharge Machining (EDM), starting from the top of the deposit and moving towards the baseplate parallel to part's Y axis (Figure 5.2b).

(a) EDM machine (b) Clamping setup

Figure 5.2: Electrical discharge machining (EDM) setup at The University of Manchester.

The two separate resulting cut faces were measured using a µScan nanofocus laser profilometer with a resolution of 30 µm by 30 µm. Two unregistered point clouds were generated. These two point clouds were aligned and averaged, to produce a single profile consisting of a series of fitted splines which could be interpolated. Fitting error average was 15.58 µm with a standard deviation of 1.23 µm, which is within the error of the laser profilometer. A two-dimensional quadrilateral mesh (with 83000 nodes and 19000, 20-node, reduced integration quadrilateral elements) was then fitted. The mesh had the following boundary conditions:

- all movement in the 2nd degree of freedom for the Z direction were restricted on one corner of the baseplate (Figure 5.4a);
- all movement in 1st and 2nd degree of freedom for the Y and Z directions were restricted (Figure 5.4b);

- displacement boundary conditions were also applied on surface nodes matching the previously fitted surface.

The two-dimensional mesh was extended to a depth of 110 mm in the X direction; this matched the length of the shortest cut piece; 20 nodes (one every 0.75 mm) were distributed along this length. Elastic properties for Ti–6Al–4V were assigned to the material. Finally an implicit Finite Element Analysis (FEA) via Abaqus Standard® (2014) solved the stress state.

The analysis procedure can produce FEA data interpolated to the spline-based surface shown in Figure 5.5a, or to provide FEA results directly as shown in Figure 5.5b and Figure 5.5c.

5.3.2.2 Neutron diffraction method

An additional measurement of the residual stress in the control sample was performed by Neutron Diffraction (ND) at the Heinz Maier-Leibnitz Zentrum in Munich, Germany, using a wavelength of $\lambda = 1.83\,\text{Å}$ and a detector angle of $\sin(2\theta) = 85.25°$ to identify the α–Ti(103) reflection. The scans were done on half the original specimen length of 250 mm. Scans started 2 mm into the baseplate, from its bottom, and finished at the top of the wall, with a spacing of 2 mm between each point, along the centreline of the wall. Diffraction peak positions in the transverse and normal directions were observed within the same setup (Fig 5.6a and Fig 5.6b), while two setups were used for the longitudinal values: diffraction peak positions of the points within the wall were measured with the part placed horizontally (Fig 5.6c), while for the interface wall-baseplate, and for the baseplate itself, a 45° rotation of the part around its X axis was necessary (Fig 5.6d). This positioning avoided the beam passing through the whole width of the baseplate.

For transverse and normal directions, a gauge volume of $2\times20\times2$ mm^3 was used; for the longitudinal direction it was $3\times3\times2$ mm^3. For each point, the scan time was at least 15 min. Direction specific lattice spacings (d_i) were calculated using Bragg's

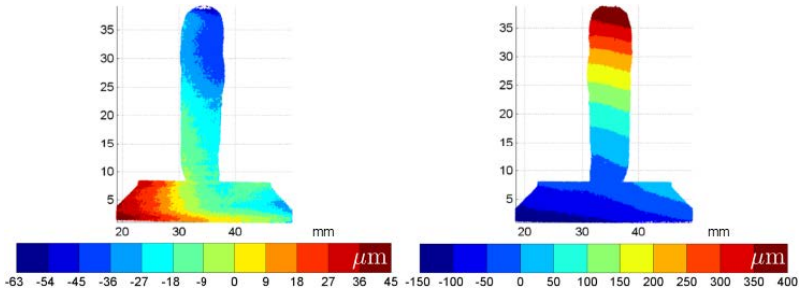

(a) Unregistered profile data collected by the μScan profilometer

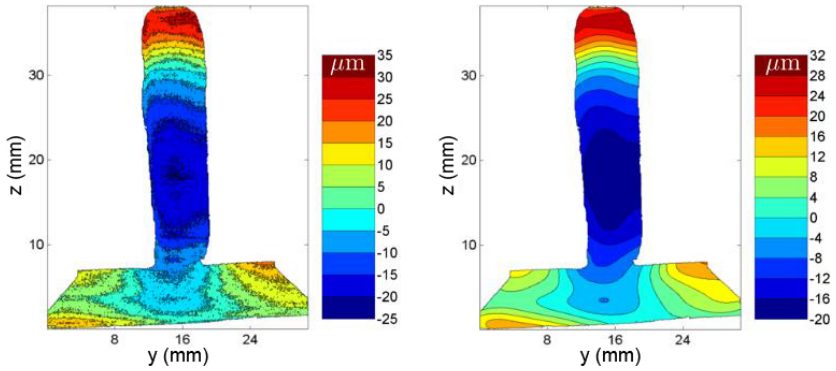

(b) Averaged surface (c) Result of spline fitting

Figure 5.3: Contour raw data processing.

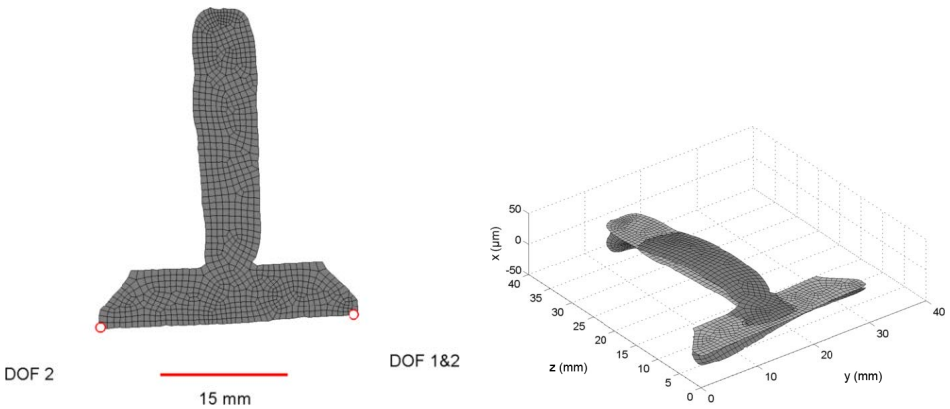

(a) Boundary conditions on the 2nd degree of freedom on one corner of the baseplate

(b) Boundary conditions on the 1nd and 2nd degrees of freedom on all movements

Figure 5.4: Boundary conditions.

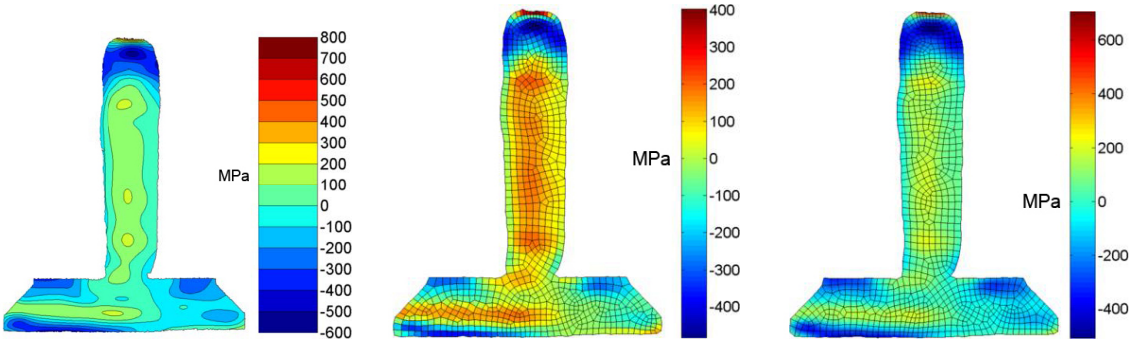

(a) Stress at integration points closest to the splined surface

(b) Average stress over each element

(c) Average integration point value at surface nodes

Figure 5.5: Finite element analysis results.

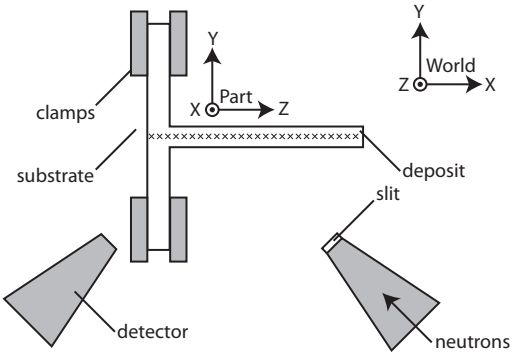

(a) Setup for transverse (Y) direction

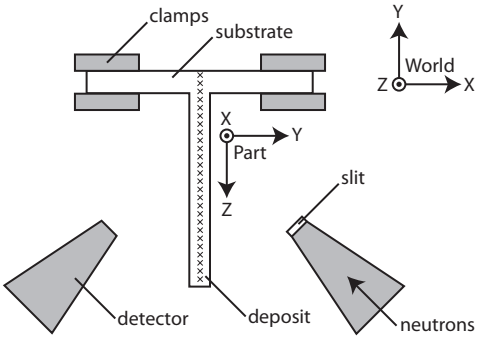

(b) Setup for normal (Z) direction

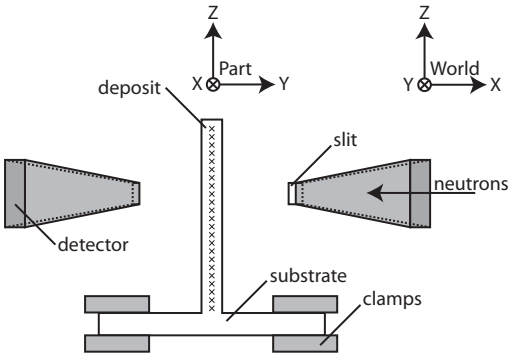

(c) Setup for longitudinal (X) direction for points within the deposit

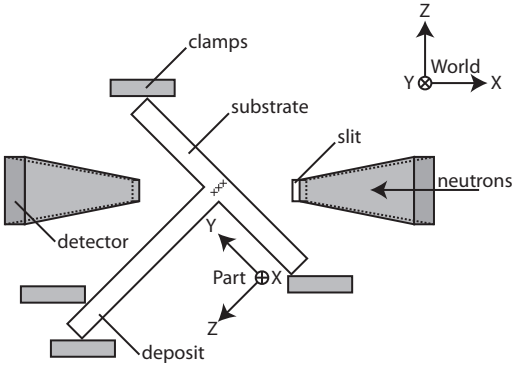

(d) Setup for longitudinal (X) direction for points within the substrate

Figure 5.6: Setups for neutron diffraction measurements.

law:

$$d_i = \frac{\lambda}{2\sin\theta_i} \tag{5.2}$$

Given that the thickness of the deposit was approximately 6 mm, plane stress in the XZ plane was imposed; the validity of this assumption will be discussed in section 5.4.3. Under the $\sigma_{yy} = 0$ condition, the triaxial formula becomes (Albertini et al., 1997):

$$\sigma_{yy,i} = \frac{(1-\nu)\,E}{(1+\nu)\,(1-2\nu)}\varepsilon_{yy,i} + \frac{\nu E}{(1+\nu)\,(1-2\nu)}\left(\varepsilon_{xx,i} + \varepsilon_{zz,i}\right) \tag{5.3}$$

where $\nu = 0.342$ is Poisson's ratio of Ti–6Al–4V and E=105.5 GPa is the elasticity modulus for the α–Ti(103) plane. This condition enables the calculation of the stress-free lattice spacings ($d^{0,i}$) parameters:

$$d_{0,i} = \frac{1-\nu}{1+\nu}\,d_i^y + \frac{\nu}{1+\nu}\left(d_i^x + d_i^z\right) \tag{5.4}$$

Principal strains (ε) were calculated as:

$$\varepsilon_{xx,i} = \frac{d_i^x - d_{0,i}}{d_{0,i}} \tag{5.5}$$

and finally principal stresses (σ) were calculated using the triaxial form of Hooke's Law:

$$\sigma_{xx,i} = \frac{E}{(1+\nu)\,(1-2\nu)}\left[(1-\nu)\,\varepsilon_{xx,i} + \nu\left(\varepsilon_{yy,i} + \varepsilon_{zz,i}\right)\right] \tag{5.6}$$

5.4 Results and discussion

5.4.1 Distortion and geometry

The distortion results are shown in Figure 5.7a and demonstrate that distortion reduced with increased rolling load.

Rolling significantly affected the WW and LH, as shown in Figure 5.7b. As the rolling load increased, there was a substantial increase in WW, which was accompanied by a reduction in the LH. The standard deviation of WW and LH reduced after rolling, from 0.18 to 0.14 and from 0.19 to 0.09 respectively for the profiled roller, and was as low as 0.03 for the flat roller, as shown by the error bars in this figure.

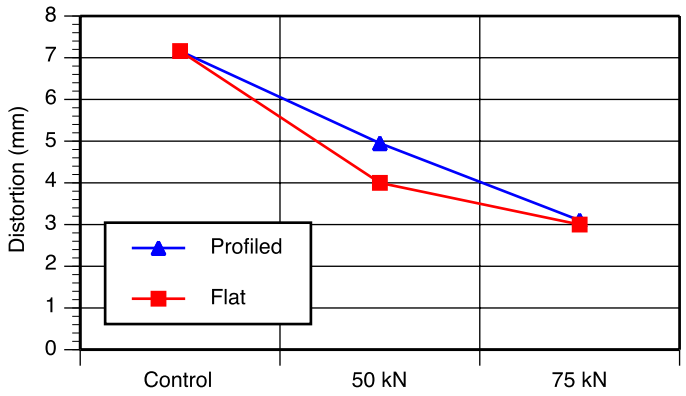

(a) Distortion

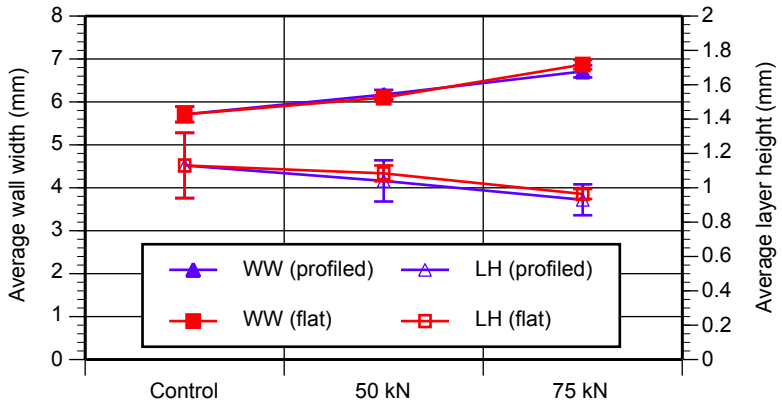

(b) Wall width and layer height

Figure 5.7: (a) distortion, and (b) average WW and LH vs. rolling load. Note the error bars in (b) represent the standard deviation of the three measurements.

The reduction in the standard deviation following rolling for both WW and LH values shown in Figure 5.7b, particularly the reduction in variation of the wall height, will simplify the automation of the deposition process. Variation in the LH, unless compensated by the control system, results in differences in the torch stand-off, which leads to a change in the heat input and ultimately to the geometric characteristics of the deposit. Operating the equipment with position rather than load control could possibly eliminate or significantly reduce height variation between passes even further.

Average engineering strains are shown in Table 5.1. The strains for the two directions were very similar for the samples rolled with the profiled roller, however the strain was greater in the transverse (Y) direction for the sample rolled with the flat roller. As discussed in chapter 3, the flat roller modified the shape of the deposit which is the reason for the large discrepancy in the strains.

Table 5.1: Average engineering strains (%).

	Profiled roller		Flat roller	
	Z direction	Y direction	Z direction	Y direction
50 kN	7.9	−8.1	4.4	−6.8
75 kN	18.2	−17.5	15.0	−20.3

Figure 5.8 shows a plot of the strain measured after rolling each layer. Please note this strain is only related to the measurements taken in the Z direction. Two main differences can be seen: the first one is related to the magnitude of the strain induced by the two rolling loads which was significantly greater with the greater load. The second is the much larger strain produced with the flat roller for a load of 75 kN during the deposition of the first few layers. However after the fifth layer, the strain induced by the profiled roller was slightly higher than the flat roller one. For a rolling load of 50 kN, the difference is minimal.

The difference in strain for the first few layers when rolling at 75 kN (Figure 5.8) can be attributed to the lack of lateral restraint of the flat roller. In the first few

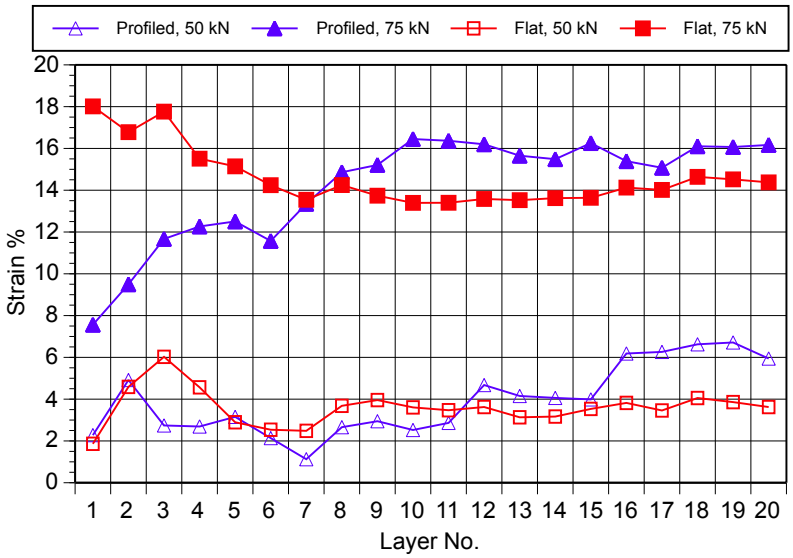

Figure 5.8: Plot of layer height (Z direction) strain vs layer number.

layer, the profiled roller was in contact with the baseplate too, because the depth of the machined groove was larger than the height which was being rolled. The flat roller was not constrained by the baseplate which resulted in higher strain. Further from the baseplate, the flat roller resulted in a lower strain.

The reduction in distortion as a consequence of rolling is likely to be linked to the modification in residual stress, discussed in the following section.

5.4.2 Residual stress

Figure 5.9 shows a comparison of the residual stress in the longitudinal (X) direction measured along the centreline of control and rolled specimens. Figure 5.10 shows a maps of the stresses for the same direction, in which the residual stress is the largest. The control specimen showed a substantial amount of tensile stress (500 MPa) concentrated just above the interface between the part and the baseplate. The magnitude of the stress steadily decreased towards the top of the wall, where it became compressive, peaking at around 250 MPa. These measurements are consistent with that reported previously in the work of Colegrove et al. (2013) and Ding et al. (2011) on steel WAAM structures, and of Hoye et al. (2014) on Ti–

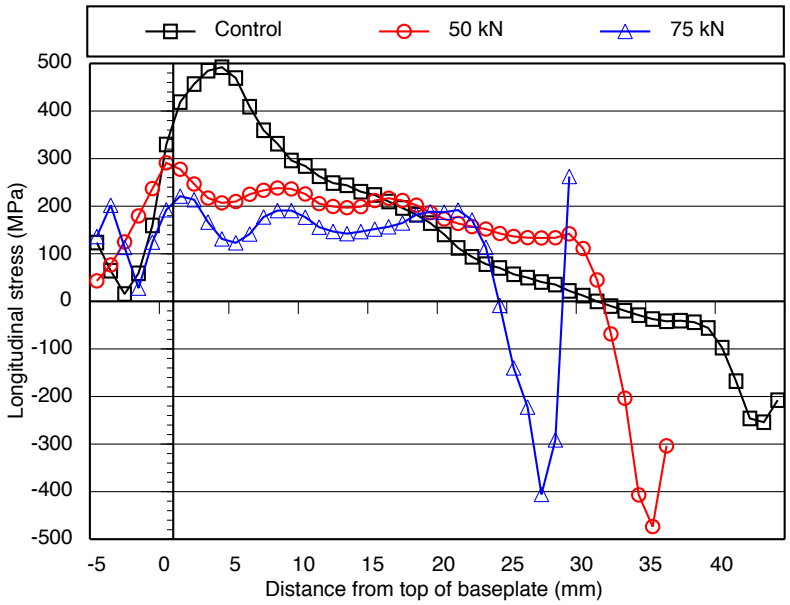

Figure 5.9: Longitudinal residual stress measured along the centreline by contour method.

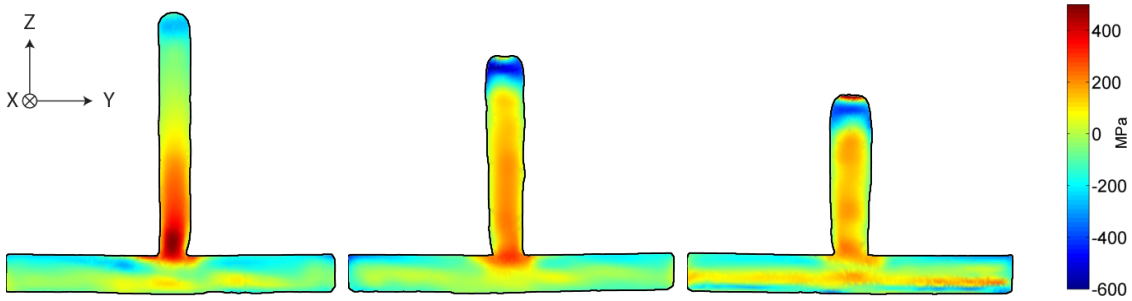

(a) Control (b) Rolled at 50 kN (c) Rolled at 75 kN

Figure 5.10: Contour maps of residual stress.

6Al–4V. Tensile stress were generated throughout the deposition due to shrinkage of the material solidifying behind the molten pool; this has been discussed thoroughly in Coules et al. (2012a). During deposition, the clamps applied a bending moment which kept the baseplate flat; the baseplate also contained the balancing compressive stress. Despite the differences in geometry in WAAM specimens, the mechanisms were the same. Upon releasing from the clamps, the baseplate bent upwards turning the tensile stress at the top of the wall into compressive ones, which resulted in the tensile peak observed at the baseplate-part interface.

The 75 kN specimen showed lower stress. In particular, at the interface between

the part and the baseplate the reduction compared to the control specimen was evident: the 75 kN specimen showed a tensile stress of 200 MPa, roughly 300 MPa less than the control specimen. In addition, the rolled specimen exhibited a much flatter tensile status (oscillating between 100 MPa and 200 MPa) and then a sudden change to highly compressive stress in the last few layers. These compressive stresses are 150 MPa to 250 MPa larger than in the control specimens; they were possibly produced by the last rolling step, which was not followed by any deposition.

During part building there was a competition between the production of residual stress by each layer deposition (*welding stress*), and the compressive ones introduced by each subsequent rolling pass. This was also evident in the work of Coules (2012) and Cozzolino (2013), who also showed the welding stress is normally higher than the one induced by rolling, suggesting the plastic zone associated with welding is generally greater than the one related to rolling.

Differently to that seen in the work of Coules et al. (2012b), rolling did not change the tensile stress into compressive ones fully. This would have been particularly desirable for both elimination of distortion, and better damage tolerance properties. The reason is that in welding during rolling the baseplate acts as main constraint in the transverse (Y) direction, and most of the deformation happens in the longitudinal one (X). In AM structures, in which case rolling is performed much further from the substrate, there is not any constraint in the transverse (Y) direction which with the normal (Z) one accommodates most of the plastic deformation. Please note in these two directions the stress is relatively low compared to the longitudinal (X) direction, as seen in Colegrove et al. (2013) and Hoye et al. (2014). Without meaningful strain in the longitudinal (X) direction, the tensile stress cannot be eliminated.

The CM enabled the measurement of stress much closer to the surface than diffraction methods. Consequently it was possible to identify and measure the tensile stress at the top of the wall, which follows the sudden compressive drop (Figure

5.10). This tensile stress was due to the friction existing between the roller and the material which produces more deformation under the surface than at the surface (Bijak-Zochowski and Marek, 1997). The tensile residual stress at the very top is not desirable from a mechanical property viewpoint, however this is not an issue as in real components the top of the deposit will be machined off.

5.4.3 Neutron diffraction vs. contour methods

There are differences between the results obtained with the contour method and those produced by neutron diffraction (Figure 5.11). Within the baseplate, the contour method showed low tensile stress, while the one measured by neutron diffraction was considerably high (250 MPa to 350 MPa). From the interface up to a wall height of 20 mm, the initial offset of roughly 150 MPa becomes progressively smaller; from an height of 20 mm to the top of the wall, the two curves are in good agreement.

Three reasons could be identified for the observed differences. Firstly, if the contour cut is performed with wrong parameters plasticity can happen ahead of the EDM wire. Secondly, the assumption of plane stress is valid when the hydrostatic stress is negligible, i.e. not close to the substrate. This could explain the lack of agreement in the baseplate between ND and CM results. Thirdly, the determination of the strain in ND measurements relies on the fit of a gaussian distribution, whose error decreases as the number of sampled grains increases (Wimpory et al., 2010). Hence having a large enough number of grains included in the gauge volume is fundamental; unfortunately, due to size of specimens and prior β grains, poor sampling statistics affected the present measurements.

5.5 Conclusions

High-pressure interpass rolling was attempted to eliminate distortion and residual stress in WAAM Ti–6Al–4V components. It was found that:

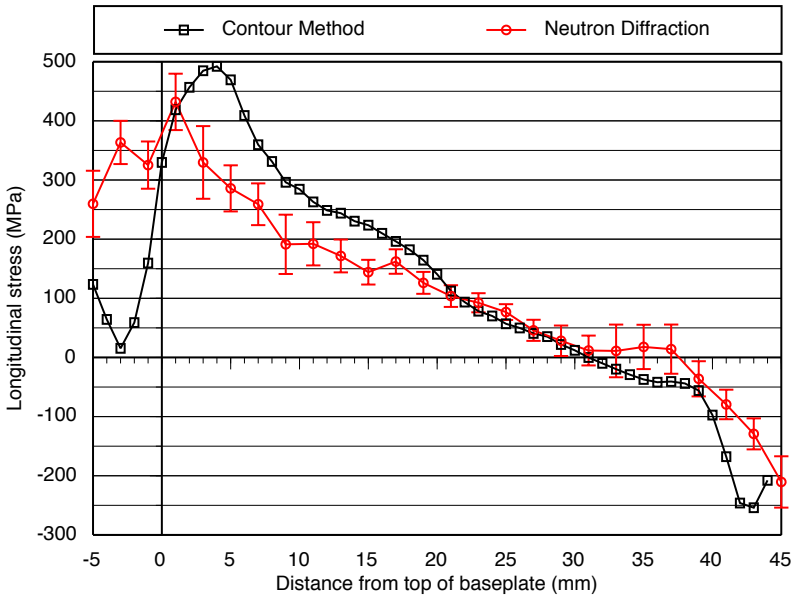

Figure 5.11: Comparison of residual stress in the longitudinal direction, measured by neutron diffraction and contour methods for the control specimen.

- unrolled specimens were characterised by a strong tensile residual stress peak at the interface between the substrate and the linear deposit, which turns into a compressive stress in the top of the wall;

- interpass rolling was successful in reducing the longitudinal residual stress, particularly at the aforementioned interface;

- rolling resulted in higher compressive stresses near the top of the wall.

Furthermore, rolling resulted in a modification of the part geometry, specifically in an increase in the wall widths and reduction in layer heights, due to plastic deformation. The standard deviation of layer height was substantially reduced, which could result in easier automation of the WAAM process and increased confidence in terms of its repeatability. This result is particularly significant from an industrial point of view.

Unfortunately, rolling did not eliminate distortion; in fact, even after rolling parts retained tensile residual stress. In conclusion, high-pressure interpass rolling is an excellent way to produce a refined equiaxed microstructure and isotropic me-

chanical properties in Ti–6Al–4V deposits, but other solutions must be investigated for distortion control.

Further work is required in order to understand:

- how residual stress affects the performance of WAAM parts, particularly fatigue;
- the reasons for the discrepancy between the contour and neutron diffraction measurements;
- how the plastic zone created by the deposition process (producing tensile stress) compares with that generated by rolling (producing compressive stress).

Acknowledgments

Dr. Matthew Roy performed cuts, contour scans and analysis at The University of Manchester. His support as well as Prof. Philip Withers' were fundamental for the analysis reported in this chapter, and their contribution is greatly acknowledged.

Dr. Blanka Szost and Dr. Sofiane Terzi participated in the neutron diffraction measurements, under the supervision of Dr. Michael Hoffman. Their support is also acknowledged.

Chapter 6

Summary and conclusions

Within the broad aim of addressing WAAM current challenges towards control of geometry, microstructure, mechanical properties and residual stress, the objectives of the present research work cover the development of an experimental process model for the deposition of titanium by Tungsten Inert Gas (TIG) WAAM; the study of the effect of high pressure rolling on the same titanium deposits; and the investigation of the relationship between O_2 contamination in the part and O_2 atmospheric levels during deposition. The key findings of the research work are summarised below.

6.1 Results summary

6.1.1 Process model of titanium TIG WAAM

In chapter 2 the feasibility of TIG deposition for AM purposes was demonstrated. A working envelope which ensures process feasibility was developed; its capability was analysed and compared with those of competing or complementary processes; and the behaviour was modelled empirically by a systematic adoption of Design Of Experiment (DOE), and validated. The DOE findings were confirmed by a subsequent analysis which established a relationship between WW and process heat input; and between LH and both heat input and $^{WFS}/_{TS}$ ratio.

TIG WAAM was capable of producing walls ranging from 5 mm to 14 mm (mostly dependent on the current), with layer thicknes between 0.6 mm to 2.1 mm (dependent on wire feed speed), reliably and automatically. The maximum deposition rate achieved was $1.2\,\mathrm{kg\,h^{-1}}$, however this was limited by wire feeder capability. Most likely much higher deposition rates can be achieved, however this would introduce other problems such as heat management and even worse distortion, as well as process instabilities related to molten pool dynamics.

6.1.2 High pressure rolling of titanium additively manufactured components

High pressure rolling was successful in improving the quality of test specimens from mechanical property anisotropy, residual stress and distortion points of view, which are of great concerns with regards to the additive manufacturing of titanium.

Microstructure In chapter 3 the beneficial effect of high-pressure rolling in terms of microstructural refinement was demonstrated. As-deposited specimens are characterised by an extremely textured microstructure, with the α phase strongly orientated towards the build direction (Z), and columnar prior β grains growing epitaxially from the bottom of the structure and often traversing its whole height. This has significant implications from a mechanical point of view. The strain introduced by each rolling pass, coupled with the heat provided when depositing a new layer, resulted in recrystallisation and ultimately in the production of equiaxed and randomly orientated prior β grains. Also the α phase observed in the rolled specimens was characterised by a smaller thickness compared to the unrolled ones.

Both the profiled and the flat roller resulted in a refined, texture-free microstructure; however due to the lack of side restraint, the flat rolled produced slightly bigger prior β grains closer to the side surfaces of the linear deposits, which could be removed by a subsequent machining operation.

Mechanical properties In chapter 4, the beneficial effects of high pressure rolling on microstructure were related to changes in mechanical properties. Unfortunately, as-deposited Ti–6Al–4V components are characterised by a degree of anisotropy which, although modest, is still undesirable. The strength is higher in the horizontal direction, while the elongation is much better in the vertical one. However, the microstructural changes induced by rolling resulted in superior and isotropic mechanical properties: for a 50 kN rolling load, the mechanical performance in the two directions are already very similar; for a load of 75 kN the properties are effectively isotropic, with elongation equal to 13%, yield strength to 1000 MPa, and ultimate tensile strength just shy of 1100 MPa. Please note these values are much better than the wrought material and much higher than the specification minima prescribed by ASTM B265 – 09a (2009).

Furthermore, the process proved to be relatively insensitive to the oxygen content in the atmosphere during deposition, at least for concentration values up to 4000 ppm. In fact, regardless of the oxygen concentration in the atmosphere, that measured in the final components was between 200 ppm and 400 ppm higher than the alloying quantity already present in the wire (1400 ppm). Consequently the hardness measured in all samples was the same.

Distortion In chapter 5 the beneficial effect of high-pressure rolling in terms of distortion reduction was demonstrated. As-deposited WAAM components are always characterised by distortion, unless more complex deposition strategies are taken into account. Both a profiled and a flat roller enabled a substantial reduction of the distortion: an approximately 50% reduction was achieved when comparing specimens rolled at 75 kN to as-deposited ones.

Residual stress In chapter 5, the relationship between rolling and residual stress was studied. While rolling reduced residual stress, it was not successful in reverting the status from tensile to fully compressive, a much more desirable condition from

a mechanical point of view. Consequently, high pressure rolling is possibly an excellent way to introduce a substantial refinement in the prior β grains structure and improve the mechanical properties; however, in terms of residual stress, other routes should be investigated, including different clamping methods, Global Mechanical Tensioning (GMT) and stress-relieving heat treatments. Therefore the rolling load should be selected based on the requirements for microstructural refinement rather than residual stress reduction.

6.2 Conclusions

The research questions identified at the start of the present research work have been addressed successfully. In particular the research objectives have been achieved:

- process modelling of titanium deposition is suitable for controlling the geometry of the layers. The empirical process equations may be used for automation of TIG WAAM;
- rolling in combination with the subsequent heat from deposition resulted in recrystallisation of the prior β grains and refined the microstructure, therefore;
- rolling improved the tested mechanical properties, which were isotropic; their variability was also reduced;
- rolling reduced dimensional variability of the layer height; this in turns increased the reliability of the process and will facilitate its automation;
- rolling reduced residual stress and part distortion, because of the plastic deformation it introduced; however distortion was not completely eliminated which requires the investigation of alternative approaches to address this issue.
- the shielding provided by the torch during deposition was sufficient to prevent O_2 contamination in the part up to O_2 atmospheric levels of 4000 ppm.

6.3 Future work

Future work could include:

- implementation of process algorithms in Computer aided manufacturing software;
- extend process algorithms to other deposition conditions:
  - oscillated and parallel walls;
  - out of position deposition;
- reliability and equipment sensitivity for the process algorithms;
- further investigation and optimisation of rolling:
  - study of relationship between rolling load, width and recrystallisation;
  - extension to 2.5-dimension rolling using e.g. a pinch roller;
  - adaptive rolling, e.g. changing load with layer number;
  - study of risk of buckling due to rolling, for tall structures;
  - development of rolling strategies for enclosed structures;
  - rolling efficiency optimisation:
    - range of wall widths;
    - equipment size;
    - how often to roll;
  - fatigue and damage tolerance study of rolled components;
  - investigation of the benefits of inter pass rolling for other materials, e.g. aluminium;
- investigation of alternative means on introducing interpass cold work, e.g.:
  - laser shock peening;
  - ultrasonic peening;
  - pneumatic hammering;
- development of WAAM-specific local shielding devices.

6.4 Final remarks

AM has still a long way to go before it sees full implementation in real-world industries. Issues such as residual stress and distortion are still of great concern for companies, and so are problems related to structural integrity such as ensuring mechanical property consistency, lack of defects, and repeatability.

With regards to WAAM, despite the results provided in the first part of the present research work, the lack of full automation such as that seen in beam-based processes needs to be addressed, before the process is commercialised.

However, the engagement of both industry and research institutions is evident, and fully justified! The advantages of this technology are proven and extremely valuable. The media are increasingly covering and discussing AM related facts and findings, but they often forget where the real benefits are. Looking just at metal AM:

- The freedom of designs achievable with beam-based processes is tickling the fancy of all the designers around the world. More and more complicated topological optimisation algorithms are generating wacky shapes which we would have never even imagined before, that promise the maximisation of certain mechanical properties while minimising the weight;
- The reduction in lead time enabled by WAAM has made building components that would have taken six months possible in just one day;
- The cost associated with the WAAM of large aerospace components is a minimal fraction of that currently incurred by companies when building the same parts traditionally.

These key features make AM a sustainable process family, as it reduces firstly the impact of manufacturing (less raw material, less energy needed), and secondly the carbon emissions components are responsible for during their life cycle, due to

their reduced weight[1] resulting in better fuel economy. AM is already responsible for a revolution in the manufacturing sector as we know it today, with greatly reduced time-to-market, increased customisation possibilities and faster implementation of design improvements.

While at the moment most of the industries involved belong to the aerospace and defence sectors, the hope is that developments will be accessible by a much larger group of users, and that this manufacturing revolution will have an impact on the daily life of everyone. Perhaps, media should stop talking about (or cover a bit less) *3D printed guns* and highlight where the real benefits are. All technologies can be used for less noble purposes but this should not mean their development should be obstructed. If anything, we are in a time in which we still have the chance to educate people and explain how (and for what) to make the most out of this technology.

[1] In particular for topologically optimised components

Bibliography

3Dprint.com, Sep. 2014. Huge 3d metal printers coming soon with 304 sq foot build volume from sciaky inc. http://3dprint.com/wp-content/uploads/2014/07/sciaky1.jpg.

Abaqus Standard®, 2014. http://www.3ds.com/products-services/simulia/portfolio/abaqus/overview/.

Abe, F., Osakada, K., Shiomi, M., Uematsu, K., Matsumoto, M., 2001. The manufacturing of hard tools from metallic powders by selective laser melting. Journal of Material Processing Technology 111 (1-3), 210–213.

Acheson, R., Aug. 1990. Automatic welding apparatus for weld build-up and method of achieving weld build-up. US Patent 4,952,769.

Additivemanufacturing.com, Sep. 2014. An amazing exclusive Q& A session with Kenn Lachenberg, application engineering manager, Sciaky Inc. http://additivemanufacturing.com/wp-content/uploads/2014/05/AM_Sciaky_DM_AM_Process_2_step.jpg.

Adobe Photoshop CS4®, 2008. http://www.adobe.com/products/photoshopfamily.html.

Ahmed, T., Rack, H., 1998. Phase transformations during cooling in $\alpha + \beta$ titanium alloys. Materials Science and Engineering A 243 (1-2), 206–211.

Airbus, 2008. Internal report.

Akman, E., Demir, A., Canel, T., Sinmazçelik, T., 2009. Laser welding of Ti6Al4V titanium alloys. Journal of Material Processing Technology 209 (8), 3705–3713.

Akula, S., Karunakaran, K., 2006. Hybrid adaptive layer manufacturing: An Intelligent art of direct metal rapid tooling process. Robotics And Computer-Integrated Manufacturing 22 (2), 113–123.

Al-Bermani, S., 2012. An Investigation into Microstructure and Microstructural Control of Additive Layer Manufactured Ti-6Al-4V by Electron Beam Melting. PhD dissertation, The University of Sheffield.

Al-Bermani, S., Blackmore, M., Zhang, W., Todd, I., 2010. The Origin of Microstructural Diversity, Texture, and Mechanical Properties in Electron Beam Melted Ti-6Al-4V. Metallurgical and Materials Transactions A 41 (12), 3422–3434.

Albertini, G., Bruno, G., Dunn, B. D., Fiori, F., Reimers, W., Wright, J. S., 1997. Comparative neutron and X-ray residual stress measurements on Al-2219 welded plate. Materials Science and Engineering A 224 (1-2), 157–165.

Allen, J., 2006. An investigation into the comparative costs of additive manufacturing vs. machine from solid for aero engine parts. In: Cost Effective Manufacturing via Net-Shape Processing, meeting proceedings RTO-MP-AVT-139. Neuilly-sur-Seine, France, pp. 17–1–17–10.

Almeida, P. S., Williams, S., 2010. Innovative process model of Ti-6Al-4V additive layer manufacturing using Cold Metal Transfer (CMT). In: 21st International Solid Freeform Fabrication Symposium. Austin, Texas, USA, pp. 25–36.

Altenkirch, J., Steuwer, A., Withers, P. J., Williams, S. W., Poad, M., Wen, S. W., 2009. Residual stress engineering in friction stir welds by roller tensioning. Science and Technology of Welding & Joining 14 (2), 185–192.

Anca, A., Fachinotti, V., Escobar-Palafox, G., Cardona, A., 2010. Computational modelling of shaped metal deposition. International Journal for Numerical Methods in Engineering 85 (1), 84–106.

Antonysamy, A. A., 2012. Microstructure, texture and mechanical property evolution during additive manufacturing of Ti6Al4V alloy for aerospace applications. PhD dissertation, University of Manchester, School of Materials.

Arcam AB®, Mar. 2014. Warm process. http://www.arcam.com/technology/electron-beam-melting/.

Arcella, F., Froes, F., 2002. Producing titanium aerospace components from powder using laser forming. Journal of Metals 52 (5), 28–30.

ASTM B265 – 09a, 2009. Standard Specification for Titanium and Titanium Alloy Strip, Sheet, and Plate.

ASTM E112 – 96, 2004. Standard Test Methods for Determining Average Grain Size.

ASTM E1382 – 1997, 1997. Standard Test Methods for Determining Average Grain Size Using Semiautomatic and Automatic Image Analysis.

ASTM E1409 - 13, 2013. Standard Test Method for Determination of Oxygen and Nitrogen in Titanium and Titanium Alloys by Inert Gas Fusion.

baesystems.com, Sep. 2014. Growing knowledge, growing parts: innovative 3D printing process reveals potential for aerospace industry. http://www.baesystems.com/article/BAES_163742/growing-knowledge-growing-parts.

Baufeld, B., Brandl, E., Van der Biest, O., 2011. Wire based additive layer manufacturing: Comparison of microstructure and mechanical properties of Ti-6Al-4V components fabricated by laser-beam deposition and shaped metal deposition. Journal of Material Processing Technology 211 (6), 1146–1158.

Baufeld, B., Van der Biest, O., Gault, R., 2009. Additive manufacturing of Ti–6Al–4V components by shaped metal deposition: microstructure and mechanical properties. Materials & Design SUPPL. 1, S106–S111.

Bijak-Zochowski, M., Marek, P., 1997. Residual stress in some elasto-plastic problems of rolling contact with friction. International Journal of Mechanical Sciences 39 (1), 15–&.

Boyer, R., 1996. An overview on the use of titanium in the aerospace industry. Materials Science and Engineering A 213 (1-2), 103–114.

BS EN 2002–1:2005, 2005. Metallic materials – Test methods – Part 1: Tensile testing at ambient temperature.

Buijs, K., July 2011. Lasercusing: will it make removing metal by machine and casting a thing of the past? www.vanleeuwen.com/media/45511/techart4.1.pdf.

Cao, X., Jahazi, M., 2009. Effect of welding speed on butt joint quality of Ti–6Al–4V alloy welded using a high-power NdYAG laser. Optics and Lasers in Engineering 47 (11), 1231–1241.

Casalino, G., Curcio, F., Minutolo, F., 2005. Investigation on Ti6Al4V laser welding using statistical and Taguchi approaches. Journal Of Materials Processing Technology 167 (2-3), 422–428.

Černy, I., 2012. An Effect of Shot Peening on Retardation and Growth of Short Fatigue Cracks in an Aircraft Al-Alloy. In: Key Engineering Materials. pp. 480–483.

Charles, C., Järvstråt, N., 2009. Modelling Ti-6Al-4V microstructure by evolution laws implemented as finite element subroutines: Application to TIG metal deposition. ASM Proceedings of the International Conference: Trends in Welding Research, 477–485.

Chen, G. Z., Fray, D. J., Farthing, T. W., 2000. Direct electrochemical reduction of titanium dioxide to titanium in molten calcium chloride. Nature 407 (6802), 361–364.

Cheng, X., Fisher, J. W., Prask, H. J., Gnäupel-Herold, T., Yen, B. T., Roy, S., 2003. Residual stress modification by post-weld treatment and its beneficial effect on fatigue strength of welded structures. International Journal of Fatigue 25 (9-11), 1259–1269.

Colegrove, P. A., Coules, H. E., Fairman, J., Martina, F., Kashoob, T., Mamash, H., Cozzolino, L. D., 2013. Microstructure and residual stress improvement in wire and arc additively manufactured parts through high-pressure rolling. Journal of Materials Processing Tech. 213 (10), 1782–1791.

Concordebattery.com, May 2014. Lockheed Martin SR-71 Blackbird. http://www.concordebattery.com/.

Contieri, R., Zanotello, M., Caram, R., 2010. Recrystallization and grain growth in highly cold worked cp–Titanium. Materials Science and Engineering A 527 (16–17), 3994–4000.

Cotteleer, M., Joyce, J., 2014. 3DOpportunity additive manufacturing paths to performance, innovation, and growth. Deloitte Review 14.

Cotterill, P., Mould, P., 1976. Recrystallization and Grain Growth in Metals, 1st Edition. Surrey University Press.

Coules, H. E., 2012. Characterising the effects of high-pressure rolling on residual stress in structural steel welds. PhD dissertation, Cranfield University.

Coules, H. E., 2013. Contemporary approaches to reducing weld induced residual stress. Materials Science And Technology 29 (1), 4–18.

Coules, H. E., Colegrove, P., Cozzolino, L. D., Wen, S. W., 2012a. Experimental measurement of biaxial thermal stress fields caused by arc welding. Journal of Materials Processing Tech. 212 (4), 962–968.

Coules, H. E., Colegrove, P., Cozzolino, L. D., Wen, S. W., Ganguly, S., Pirling, T., 2012b. Effect of high pressure rolling on weld-induced residual stresses. Science and Technology of Welding & Joining 17 (5), 394–401.

Coykendall, J., Cotteleer, M., Holdowsky, J., Mahto, M., 2014. 3D opportunity in aerospace and defense: Additive manufacturing takes flight. A Deloitte series on additive manufacturing.

Cozzolino, L. D., 2013. Finite element analysis of localised rolling to reduce residual stress and distortion. PhD dissertation, Cranfield University.

CRP Technology, Jul. 2011. Component made by electron beam melting. http://www.crptechnology.com/sito/images/stories/ElementiFissiHome/ebm-slm/ebm-impeller-arcam.jpg.

CRP-Technology, Jul. 2011. Component made by selective laser melting. http://www.crptechnology.com/sito/images/stories/ElementiFissiHome/ebm-slm/slm.jpg.

Cuellar, S. D., Hill, M. R., DeWald, A. T., Rankin, J. E., 2012. Residual stress and fatigue life in laser shock peened open hole samples. International Journal of Fatigue 44 (C), 8–13.

Dalaei, K., Karlsson, B., Svensson, L. E., 2011. Stability of shot peening induced residual stresses and their influence on fatigue lifetime. Materials Science and Engineering A 528 (3), 1008–1015.

Davies, P., 2009. An Investigation of Microstructure and Texture Evolution in

the Near-α Titanium Alloy Timetal® 834. PhD dissertation, The University of Sheffield.

Davies, P., Wynne, B., Rainforth, W., Thomas, M., Threadgill, P., 2011. Development of Microstructure and Crystallographic Texture during Stationary Shoulder Friction Stir Welding of Ti-6Al-4V. Metallurgical and Materials Transactions A 42 (8), 2278–2289.

Dehghan-Manshadi, A., Reid, M., Dippenaar, R., 2010. Effect of microstructural morphology on the mechanical properties of titanium alloys. In: 15th International Conference on the Strength of Materials (ICSMA-15). Vol. 240. pp. 1–4.

Denney, P., Shinn, B., Fallara, P., 2005. Laser plus GMAW hybrid welding of titanium. In: Proceedings of the International Offshore and Polar Engineering Conference. Vol. 2005. pp. 106–111, cited By (since 1996) 0.

Derringer, G., Suich, R., 1980. Simultaneous optimization of several response variables. Journal of Quality Technology 12 (4), 214–219.

Dieter Jr., G., 1961. Mechanical metallurgy, 1st Edition. McGraw–Hill.

Ding, J., Colegrove, P., Mehnen, J., Ganguly, S., Sequeira Almeida, P. M., Wang, F., Williams, S. W., 2011. Thermo-mechanical analysis of Wire and Arc Additive Layer Manufacturing process on large multi-layer parts. Computational Materials Science 50 (12), 3315–3322.

Ebel, T., Ferri, O., Limberg, W., Oehring, M., Pyczak, F., Schimansky, F.-P., 2012. Metal injection moulding of titanium and titanium-aluminides. Key Engineering Materials 520, 153–160.

Ehrgott, M., 2005. Multicriteria Optimization, 2nd Edition. Springer.

Ellis, M., Gittos, M., 1995. Tungsten inert gas welding of titanium and its alloys. Welding and Metal Fabrication 63 (1).

Elmer, J. W., Palmer, T. A., Babu, S. S., Zhang, W., DebRoy, T., 2004. Phase transformation dynamics during welding of Ti–6Al–4V. Journal of Applied Physics 95 (12), 8327–8339.

Elmer, J. W., Palmer, T. A., Wong, J., 2003. In situ observations of phase transitions in Ti–6Al–4V alloy welds using spatially resolved x-ray diffraction. Journal of Applied Physics 93 (4), 1941–1947.

Eze, E., 2009. VBC welding system parameter effect on the shape and microstructure of additively manufactured Ti6Al4V titanium alloy. Master's thesis, Cranfield University.

Filip, R., Kubiak, K., Ziaja, W., Sieniawski, J., 2003. The effect of microstructure on the mechanical properties of two-phase titanium alloys. Journal of Material Processing Technology 133 (1-2), 84–89.

Ganesh, P., Sundar, R., Kumar, H., Kaul, R., Ranganathan, K., Hedaoo, P., Raghavendra, G., Kumar, S. A., Tiwari, P., Nagpure, D. C., Bindra, K. S., Kukreja, L. M., Oak, S. M., 2014. Studies on fatigue life enhancement of pre-fatigued spring steel specimens using laser shock peening. Journal of Materials & Design 54 (C), 734–741.

Gao, H., Dutta, R. K., Huizenga, R. M., Amirthalingam, M., Hermans, M. J. M., Buslaps, T., Richardson, I. M., Aug. 2014. Stress relaxation due to ultrasonic impact treatment on multi-pass welds. Science and Technology of Welding & Joining 19 (6), 505–513.

Gil, F., Ginebra, M., Manero, J., Planell, J., 2001. Formation of α-Widmanstätten structure: Effects of grain size and cooling rate on the Widmanstätten morphologies and on the mechanical properties in Ti6Al4V alloy. Journal of Alloys and Compounds 329 (1-2), 142–152.

Grubbs, F. E., 1969. Procedures for detecting outlying observations in samples. Technometrics 11 (1), 1–21.

Heralić, A., Christiansson, A.-K., Ottosson, M., Lennartson, B., 2010. Increased stability in laser metal wire deposition through feedback from optical measurements. Optics and Lasers in Engineering 48 (4), 478–485.

Heralić, A., Ottosson, M., Hurtig, K., Christiansson, A.-K., 2008. Visual feedback for operator - Interaction in robotized laser metal deposition. In: Surface Modification Technologies XXII. Trollhattan, Sweden, pp. 297–304.

Hoye, N., Li, H., Cuiuri, D., Paradowska, A. M., 2014. Measurement of Residual Stresses in Titanium Aerospace Components Formed via Additive Manufacturing. In: Materials Science Forum. pp. 124–129.

Hu, Y., Grandhi, R. V., 2012. Efficient numerical prediction of residual stress and deformation for large-scale laser shock processing using the eigenstrain methodology. Surface & Coatings Technology 206 (15), 3374–3385.

Huang, J., 2011. The characterisation and modelling of porosity formation in electron beam welded titanium alloys. PhD dissertation, University of Birmingham, School Metallurgy and Materials.

Humbert, M., Moustahfid, H., Wagner, F., Philippe, M., 1994. Evaluation of the high temperature texture of the β phase of a TA6V sample from the individual orientations of grains of the low temperature α phase. Scripta Metallurgica et Materialia 30 (3), 377–382.

Humphreys, F., Hatherly, M., 2004. Recrystallization and Related Annealing Phenomena, 2nd Edition. Elsevier Ltd.

ImageJ, 2012. http://rsbweb.nih.gov/ij/index.html.

Kahveci, A., Welsch, G., 1986. Effect of oxygen on the hardness and alpha/beta phase ratio of Ti6Al4V alloy. Scripta Metallurgica 20 (9), 1287–1290.

Kahveci, A., Welsch, G., 1991. Hardness versus strength correlation for oxygen-strengthened Ti-6Al-4V alloy. Scripta Metallurgica et Materialia 25 (8), 1957–1962.

Katzarov, I., Malinov, S., Sha, W., 2002. Finite Element Modeling of the Morphology of b to a Phase Transformation in Ti-6Al-4V Alloy. Metallurgical and Materials Transactions A 33A, 1027–1039.

Kelly, S., Kampe, S., 2004a. Microstructural evolution in laser-deposited multilayer Ti-6AI-4V builds: Part II. Thermal modeling. Metallurgical And Materials Transactions A-Physical Metallurgy And Materials Science 35A (6), 1869–1879.

Kelly, S., Kampe, S., 2004b. Microstructural evolution in laser-deposited multilayer Ti-6Al-4V builds: Part I. Microstructural characterization. Metallurgical And Materials Transactions A-Physical Metallurgy And Materials Science 35A (6), 1861–1867.

Kruth, J. P., Levy, G., Klocke, F., Childs, T. H. C., 2007. Consolidation phenomena in laser and powder-bed based layered manufacturing. CIRP Annals - Manufacturing Technology 56 (2), 730–759.

Kurkin, S., Anufriev, V., 1984. Preventing distortion of welded thin-walled members of AMg6 and 1201 aluminum alloys by rolling the weld with a roller behind the welding arc. Welding Production 31 (10), 32–34.

Lee, E., 2004. Microstructure evolution and microstructure/mechanical properties relationships in $\alpha+\beta$ titanium alloys. PhD dissertation, The Ohio State University.

Levy, G., Schindel, R., Kruth, J., 2003. Rapid manufacturing and rapid tooling with

layer manufacturing (LM) technologies, state of the art and future perspectives. CIRP Annals - Manufacturing Technology 52 (2), 589–609.

Li, C., Muneharua, K., Takao, S., Kouji, H., 2009. Fiber laser-GMA hybrid welding of commercially pure titanium. Materials and Design 30 (1), 109–114, cited By (since 1996) 16.

Li, X., Xie, J., Zhou, Y., 2005. Effects of oxygen contamination in the argon shielding gas in laser welding of commercially pure titanium thin sheet. Journal Of Materials Science 40 (13), 3437–3443.

Liu, Z., Curioni, M., Jamshidi, P., Walker, A., Prangnell, P., Thompson, G. E., Skeldon, P., Sep. 2014. Applied Surface Science. Applied Surface Science 314, 233–240.

Lütjering, G., 1998. Influence of processing on microstructure and mechanical properties of $(\alpha + \beta)$ titanium alloys. Materials Science and Engineering A 243 (1-2), 32–45.

Lütjering, G., Albrecht, J., Sauer, C., Krull, T., 2007. The influence of soft, precipitate-free zones at grain boundaries in Ti and Al alloys on their fatigue and fracture behavior. Materials Science and Engineering A 468-470 (SPEC. ISS.), 201–209.

Lütjering, G., Williams, J., 2007. Titanium, 2nd Edition. Springer.

Majdic, M., Ziegler, G., 1973. Effect of the metastable beta - phase transformations in the ti-6al-4v alloy. Zeitschrift fuer Metallkunde/Materials Research and Advanced Techniques 64 (11), 751–758.

Martina, F., 2010. Study of the benefits of plasma deposition of Ti–6Al–4V structures made by additive layer manufacture. Master's thesis, Cranfield University.

Martina, F., Mehnen, J., Williams, S. W., Colegrove, P., Wang, F., 2012. Investigation of the benefits of plasma deposition for the additive layer manufacture of Ti–6Al–4V. Journal of Materials Processing Tech. 212 (6), 1377–1386.

Measure Roi PA, 2012. http://www.optinav.com/Measure-Roi.htm.

Milewski, J., Dickerson, P., Nemec, R., Lewis, G., Fonseca, J., 1999. Application of a manufacturing model for the optimization of additive processing of Inconel alloy 690. Journal Of Materials Processing Technology 91 (1-3), 18–28.

Miura, H., Itoh, Y., Ueamtsu, T., Sato, K., 2010. The influence of density and oxygen content on the mechanical properties of injection molded Ti–6Al–4V alloys. Advances in Powder Metallurgy and Particulate Materials - 2010, Proceedings of the 2010 International Conference on Powder Metallurgy and Particulate Materials, PowderMet 2010, 446–453.

Mohandas, T., Banerjee, D., Rao, V. K., 1999. Fusion zone microstructure and porosity in electron beam welds of an $\alpha + \beta$ titanium alloy. Metallurgical and Materials Transactions A: Physical Metallurgy and Materials Science 30 (3), 789–798.

Montgomery, D., 2006. Design and Analysis of Experiments, 5th Edition. John Wiley & Sons.

Morri, A., 2008. Heat treatments of two-phase titanium alloys, correlations between microstructure and mechanical properties — trattamenti termici delle leghe di titanio $\alpha + \beta$, correlazioni fra microstruttura e comportamento meccanico. Metallurgia Italiana 100 (10).

Mueller, S., Stiles, E., Dienemann, R., 2006. Study of porosity formation during laser welding of Ti6Al4V. ICALEO 2006 - 25th International Congress on Applications of Laser and Electro-Optics, Congress Proceedings, 133–138.

Murr, L., Esquivel, E., Quinones, S., Gaytan, S., Lopez, M., Martinez, E., Medina, F., Hernandez, D., Martinez, E., Martinez, J., Stafford, S., Brown, D., Hoppe, T., Meyers, W., Lindhe, U., Wicker, R., 2009. Microstructures and mechanical properties of electron beam-rapid manufactured Ti–6Al–4V biomedical prototypes compared to wrought Ti–6Al–4V. Materials Characterization 60 (2), 96–105.

Murr, L., Gaytan, S., Ceylan, A., Martinez, E., Martinez, J., Hernandez, D., Machado, B., Ramirez, D., F.Medina, S.Collins, Wicker, R., 2010a. Characterization of titanium aluminide alloy components fabricated by additive manufacturing using electron beam melting. Acta Materialia 58 (5), 1887–1894.

Murr, L., Gaytan, S., Medina, F., Martinez, E., Martinez, J., Hernandez, D., Machado, B., Ramirez, D., Wicker, R., 2010b. Characterization of Ti-6Al-4V open cellular foams fabricated by additive manufacturing using electron beam melting. Materials Science & Engineering A 527 (7-8), 1861–1868.

Patnaik, A., Poondla, N., Bathini, U., Srivatsan, T., 2011. On the use of gas metal arc welding for manufacturing beams of commercially pure titanium and a titanium alloy. Materials and Manufacturing Processes 26 (2), 311–318.

Price, D. A., Williams, S. W., Wescott, A., Harrison, C. J. C., Rezai, A., Steuwer, A., Peel, M., Staron, P., Koçak, M., 2007. Distortion control in welding by mechanical tensioning. Science and Technology of Welding & Joining 12 (7), 620–633.

Prime, M. B., 2001. Cross-Sectional Mapping of Residual Stresses by Measuring the Surface Contour After a Cut. Journal of Engineering Materials and Technology 123 (2), 162.

Qazi, J., Senkov, O., Rahim, J., Froes, F., 2003. Kinetics of martensite decomposition in Ti–6Al–4V–xH alloys. Materials Science and Engineering A 359 (1-2), 137–149.

Qiu, C., Ravi, G., Dance, C., Ranson, A., Dilworth, S., Attallah, M., 2015. Fabrication of large Ti–6Al–4V structures by direct laser deposition. Journal of Alloys and Compounds 629, 351–361.

Rangaswamy, P., Griffith, M., Prime, M., Holden, T., Rogge, R., Edwards, J., Sebring, R., 2005. Residual stresses in LENS®components using neutron diffraction and contour method. Materials Science and Engineering A 399 (1-2), 72–83.

Richards, D., Prangnell, P., Williams, S., Withers, P., 2008. Global mechanical tensioning for the management of residual stresses in welds. Materials Science and Engineering A 489 (1-2), 351–362.

Roggensack, M., Walter, M., Boning, K., 1993. Studies on laser-welded and plasma-welded titanium. Dental Materials 9 (2), 104–107.

Sauer, C., Lütjering, G., 2001. Influence of α layers at β grain boundaries on mechanical properties of Ti–alloys. Materials Science and Engineering A 319-321, 393–397.

Sciaky, Sep. 2014a. Sciaky – Additive Manufacturing. http://www.sciaky.com/additive_manufacturing.html.

Sciaky, Sep. 2014b. Sciaky's metal additive manufacturing – 3d printing brochure. http://www.sciaky.com/documents/Sciaky_Direct_Manufacturing.pdf.

Sciaky, Sep. 2014c. Vx-110 advanced manufacturing system. http://www.sciaky.com/vx-110_additive_manufacturing-system.html.

Seshacharyulu, T., Medeiros, S., Frazier, W., Prasad, Y., 2000. Hot working of commercial Ti–6Al–4V with an equiaxed $\alpha--\beta$ microstructure: Materials modeling considerations. Materials Science and Engineering A 284 (1–2), 184–194.

Shin, H.-S., Hur, J.-M., Jeong, S. M., Jung, K. Y., 2012. Direct electrochemical

reduction of titanium dioxide in molten lithium chloride. Journal of Industrial and Engineering Chemistry 18 (1), 438–442.

Shinn, B. W., Farson, D. F., Denney, P. E., 2005. Laser stabilisation of arc cathode spots in titanium welding. Science and Technology of Welding & Joining 10 (4), 475–481.

Skagen, Jan. 2012. Watch information. http://www.skagen.com/en-US/service/watchInfo.fx.

Song, Y., Park, S., 2006. Experimental investigations into rapid prototyping of composites by novel hybrid deposition process. Journal Of Materials Processing Technology 171 (1), 35–40.

Stat-Ease Design-Expert 7.1®, 2008. http://www.statease.com/dx71descr.html.

Talkington, J., Harwig, D., Castner, H., Mitchell, G., 2000. Development of titanium weld color inspection tools. Welding Journal 79 (3), 35–38.

Tiley, J., Searles, T., Lee, E., Kar, S., Banerjee, R., Russ, J. C., Fraser, H. L., 2004. Quantification of microstructural features in α/β titanium alloys. Materials Science and Engineering A 372 (1-2), 191–198.

Tolochko, N., Mozzharov, S., Yadroitsev, I., Laoui, T., Froyen, L., Titov, V., Ignatiev, M., 2004. Selective laser sintering and cladding of single-component metal powders. Rapid Prototyping Journal 10 (2), 88–97.

Trautmann, H., Mehnen, J., 2009. Preference-based Pareto optimization in certain and noisy environments. Engineering Optimization 41 (1), 23–38.

Tsay, L., Shan, Y.-P., Chao, Y.-H., Shu, W., 2006. The influence of porosity on the fatigue crack growth behavior of Ti–6Al–4V laser welds. Journal of Material Science 41 (22), 7498–7505.

Van-Nicholas, January 2012. Why Ti? http://vannicholas.com/10/2/why%20ti/content.aspx.

Various, 1991. ASM Handbook: Heat Treating, 1st Edition. ASM International.

Wang, F., Mei, J., Jiang, H., Wu, X., 2007a. Laser fabrication of Ti6Al4V/TiC composites using simultaneous powder and wire feed. Materials Science and Engineering A 445-446, 461–466.

Wang, F., Mei, J., Wu, X., 2007b. Compositionally graded Ti6Al4V+TiC made by direct laser fabrication using powder and wire. Materials & Design 28 (7), 2040–2046.

Wang, F., Mei, J., Wu, X., 2008. Direct laser fabrication of Ti6Al4V/TiB. Journal of Material Processing Technology 195 (1-3), 321–326.

Wang, F., Williams, S., Colegrove, P., Antonysamy, A. A., 2013. Microstructure and Mechanical Properties of Wire and Arc Additive Manufactured Ti-6Al-4V. Metallurgical and Materials Transactions A 44 (2), 968–977.

Wang, F., Williams, S., Rush, M., 2011. Morphology investigation on direct current pulsed gas tungsten arc welded additive layer manufactured Ti6Al4V alloy. International Journal of Advanced Manufacturing Technology 57 (5–8), 597–603.

Wen, S. W., Colegrove, P. A., Williams, S. W., Morgan, S. A., Wescott, A., Poad, M., Aug. 2010. Rolling to control residual stress and distortion in friction stir welds. Science and Technology of Welding & Joining 15 (6), 440–447.

Wen, S. W., Williams, S. W., Morgan, S. A., Wescott, A., Poad, M., Moore, G., 2009. Rolling of friction stir welds for residual stress and distortion control. In: 9th International Seminar Numerical Analysis of Weldability. pp. 1–32.

Wimpory, R., Wasmuth, U., Rebelo-Kornmeier, J., Hofmann, M., 2010. The effect

of grain size on strain determination using a neutron diffractometer. In: Materials Science Forum. Vol. 638–642. pp. 2405–2410.

Withers, P., Bhadeshia, H., 2001a. Overview - Residual stress part 1 - Measurement techniques. Materials Science And Technology 17 (4), 355–365.

Withers, P., Bhadeshia, H., 2001b. Overview - Residual stress part 2 - Nature and origins. Materials Science And Technology 17 (4), 366–375.

Withers, P. J., 2007. Residual stress and its role in failure. Reports on Progress in Physics 70 (12), 2211–2264.

Withers, P. J., 2013. Strategies for the Minimization of Residual Stresses in Welds. In: 9th International Conference on Trends in Welding Research. Chicago, Illinois, USA, pp. 139–147.

Xue, C., Hu, J., Chen, G., Zhou, W., Zhang, J., 2012. Recovery and recrystallization behavior of Ti6Al4V alloys after cold deformation. Xiyou Jinshu Cailiao Yu Gongcheng/Rare Metal Materials and Engineering 41 (3), 472–476.

Yan, Y., Li, S., Zhang, R., Lin, F., Wu, R., Lu, Q., Xiong, Z., Wang, X., Jul. 2009. Rapid Prototyping and Manufacturing Technology: Principle, Representative Technics, Applications, and Development Trends. Tsinghua Science and Technology 14 (S1), 1–12.

Zäh, M., Branner, G., 2010. Investigations on residual stresses and deformations in selective laser melting. Production Engineering - Research and Development 4 (1), 35–45.

Zäh, M., Lutzmann, S., 2010. Modelling and simulation of electron beam melting. Production Engineering - Research and Development 4 (1), 15–23.

Zhang, H., Xu, J., Wang, G., 2003. Fundamental study on plasma deposition manufacturing. Surface and Coatings Technology 171 (1-3), 112–118.

Zhang, K., Zhang, J., 2011. Temperature gradient and heat conduction of titanium alloy during laser welding. Advanced Materials Research 154-155, 42–45.

Zhou, J. Z., Huang, S., Zuo, L. D., Meng, X. K., Sheng, J., Tian, Q., Han, Y. H., Zhu, W. L., 2014. Effects of laser peening on residual stresses and fatigue crack growth properties of Ti—6Al—4V titanium alloy. Optics and Lasers in Engineering 52 (C), 189–194.

Appendix A

Effects of shielding conditions and temperature upon geometry and microstructure

A.1 Introduction

Developing a geometric, empirical model for some AM metric is a time-consuming task, in which the largest proportion of the time is consumed in taking measurements and letting the part cool down to room temperature. It was however interesting to assess the effect of temperature on bead geometry. In fact, if temperature had no effect, it would be possible to carry out the experiments without worrying about waiting between the deposition of two layers, thus ultimately reducing the total time for task completion.

Moreover, as discussed previously, oxidation represents a major issue. It is known that oxygen affects surface tension, and consequently bead geometry. An assessment of shielding conditions (and ultimately of oxygen content) effect upon geometry, particularly if no effect was observed, could ease the geometrical modelling, as this task could be completed without worrying about achieving optimal shielding conditions.

A.2 Methodology

WAAM deposition setup consisted of a TIG torch, a 100 mm long trailing shield, and a Migatronic power source. The torch was mounted on a 6-axes Fanuc Robot. Pureshield Argon Gas was used for shielding as well as for the torch. Torch standoff was 3.5 mm. Wire was always forward-fed. For a schematic representation of the setup please refer to Figure 2.2 on page 54.

Four specimens were built. Wire Feed Speed (WFS), Travel Speed (TS) and Current were all kept constant at $1\,\mathrm{m\,min^{-1}}$, $3\,\mathrm{mm\,s^{-1}}$ and 130 A, respectively. The effect of shielding conditions was assessed by changing the trailing shield gas flow rate from $20\,\mathrm{l\,min^{-1}}$ to $10\,\mathrm{l\,min^{-1}}$ and $0\,\mathrm{l\,min^{-1}}$ (Table A.1). In this way, the formation of a thin oxide layer was induced, and this layer was eventually included in the specimen while depositing a new layer. The effect of temperature was evaluated by waiting until the part cooled down to room temperature, or by depositing another layer immediately after the necessary measurements were taken.

Table A.1: Experimental design for assessment of shielding conditions and temperature effects upon bead geometry.

Specimen	Trailing shield gas flow rate ($\mathrm{l\,min^{-1}}$)	Temperature (°C)
a	10	Room
b	0	Room
c	20	74
d	20	Room

Selected metrics for the comparison were LH and WW. The first was measured every layer at three different points, while the latter was measured by using Adobe Photoshop CS4® (2008) with optical micrography image of ground, polished and etched cross-sections (one section per sample was analysed). The first four layers were excluded from the comparison, and the layer height average values were considered.

From a microstructrural point of view, heat affected zone, base, middle and top

layers were analysed. In particular, microstructure morphology, as well as α phase precipitation size and characteristics were assessed qualitatively.

A.3 Results

A.3.1 Geometry

Confidence intervals on the difference in the mean (with unknown but assumed equal variances) were calculated to determine whether the temperature and shielding conditions led to a change in the process or not, under the reasonable assumption that data were normally distributed. Student's t distribution was used. Mean and standard deviation values were calculated considering the 16 layers of each sample, i.e. considering the measures of layer heights from the 4th to the 20th layer. For the LH, as can be seen from the error bars of Figure A.1, at this level of confidence it cannot be stated that a difference in the means exists. Therefore, neither shielding condition nor part temperature had an effect on LH. Because only one cross-section was taken from each specimen, an appropriate statistical analysis cannot be performed on WW. However, considered the small variability observed, and that for the conservation of volume if the LH does not change so should do the WW, it can be concluded that WW is not affected by shielding conditions and temperature.

A.3.2 Microstructure

Little differences were observed in the microstructure of the different specimens. The heat affected zone was characterised by the same features, i.e. a mixed structure of α colonies and Widmanstätten (Figure A.2, images (a) to (d)). In the base layers Widmanstätten prevailed and a visual comparison of lamellae size did not show any significative difference (Figure A.3, images (a) to (d)), except for the specimen c (the one in which layers were deposited when the part was still hot) where some

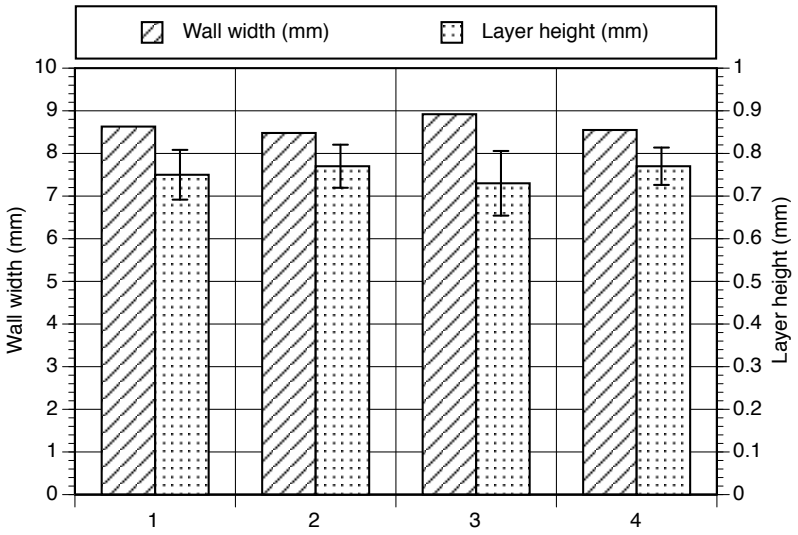

Figure A.1: Comparison of specimens wall widths and layer heights under different experimental conditions. Please note error bars are 95% confidence intervals.

large α precipitations (α_M) can be identified (Figure A.3c). Also in the middle layers microstructure are comparable, and characterised mostly by Widmanstätten (Figure A.4). In the top layers there is a strong increase in the quantity of α_M at expenses of the Widmanstätten (Figure A.5). Lamellae appear long and needle-like, an evidence of martensite presence. At the grain boundaries, in all cases α precipitations were observed.

A.4 Discussion

A.4.1 Geometry

From the results it is clear that shielding conditions and part temperature (at least below 74 °C) do not affect the bead geometry. Oxygen levels, even when the part was covered with a dull layer of oxide, do not reduce the droplet surface tension appreciably. The same applies for the temperature. A relationship between substrate temperature and geometrical features exists; indeed, it was shown in previous researches (Martina, 2010) that the first four to five layers are narrower than the rest, due to the efficient heat extraction given by the baseplate. When moving further

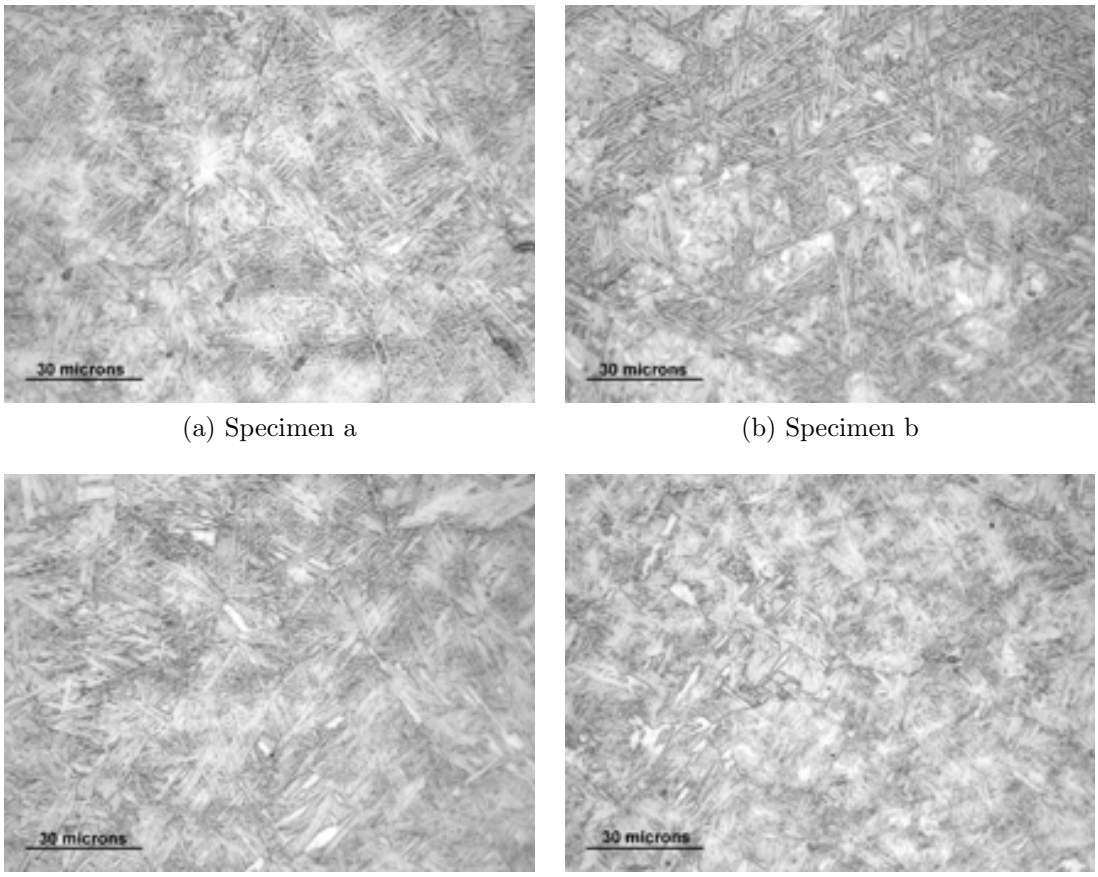

(a) Specimen a

(b) Specimen b

(c) Specimen c

(d) Specimen d

Figure A.2: Comparison of microstructure, heat affected zone.

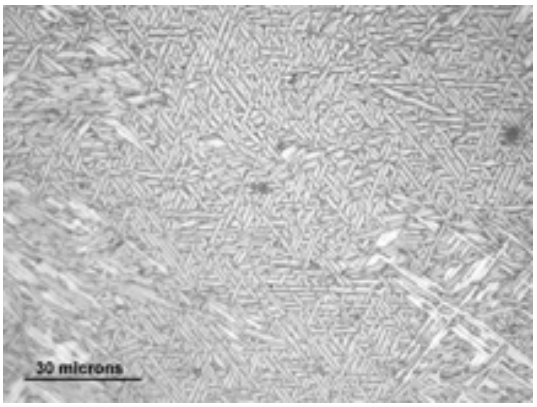

(a) Specimen a

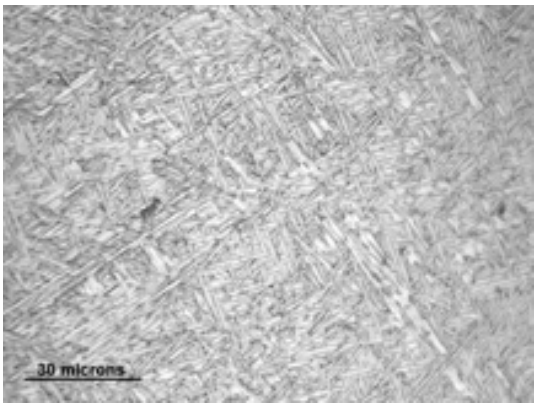

(b) Specimen b

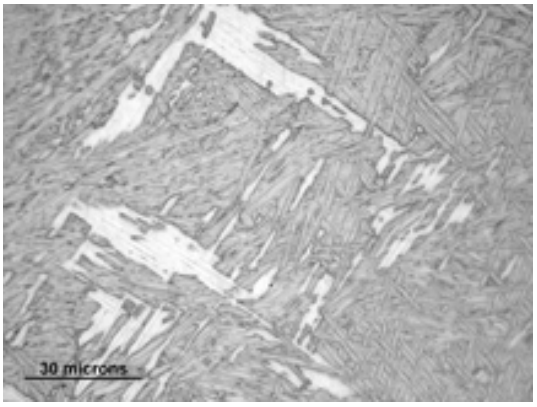

(c) Specimen c

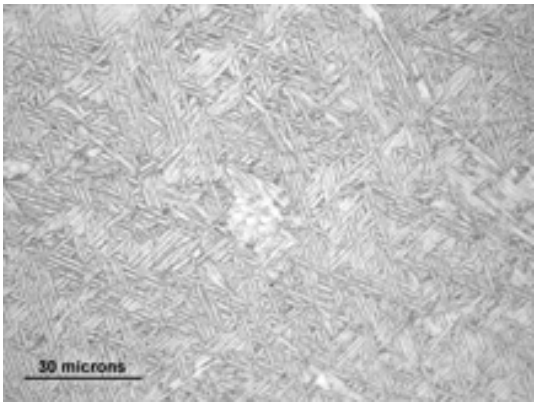

(d) Specimen d

Figure A.3: Comparison of microstructure, base layers.

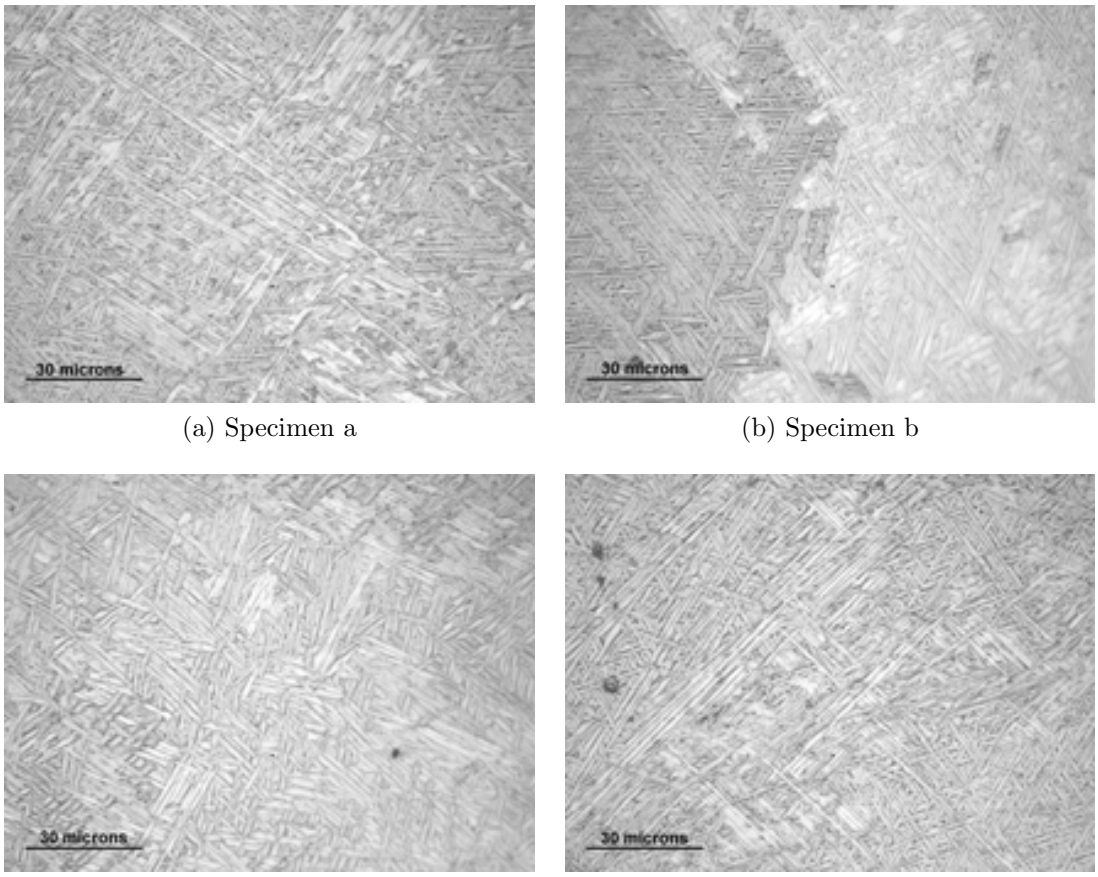

(a) Specimen a

(b) Specimen b

(c) Specimen c

(d) Specimen d

Figure A.4: Comparison of microstructure, middle layers.

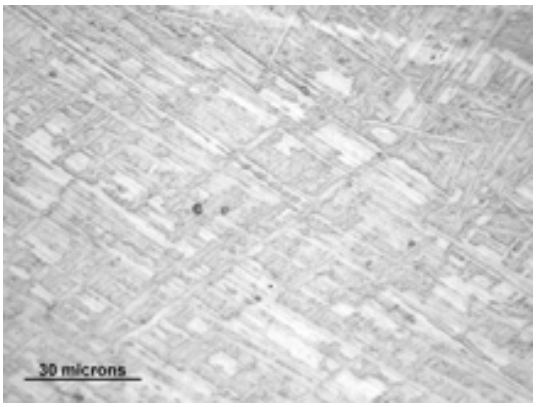

(a) Specimen a

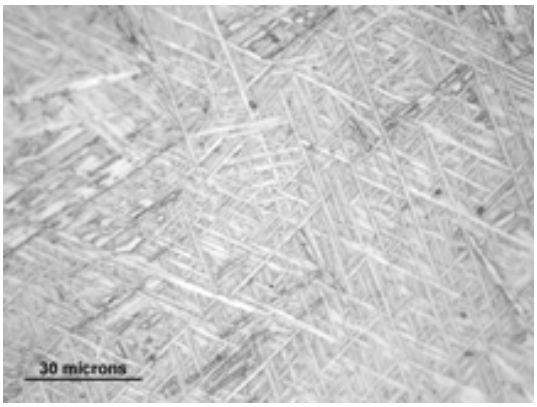

(b) Specimen b

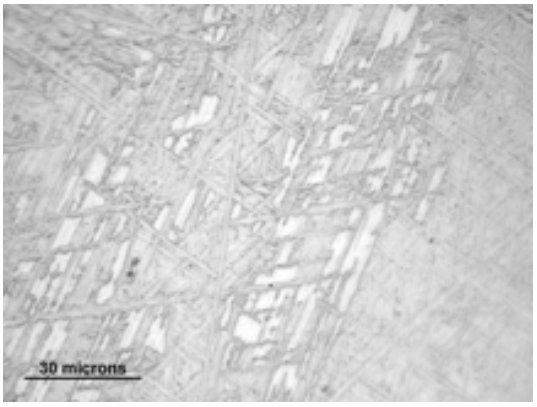

(c) Specimen c

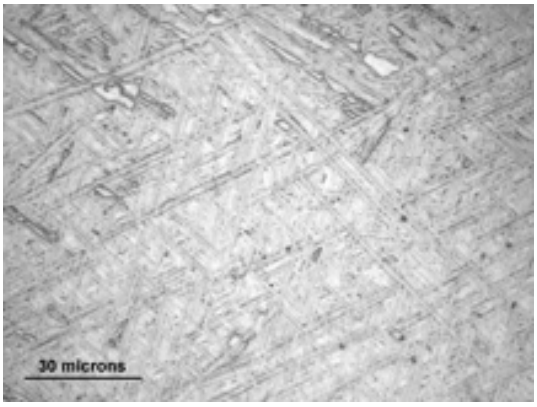

(d) Specimen d

Figure A.5: Comparison of microstructure, top layers.

from the baseplate, the process enters a steady state which was not disturbed by the increase in part temperature. It stands to reason that higher cooling rates are achieved close to the baseplate, which acts as a heat sink, while further from it, due to the change in the medium the heat flows through (from a flat, wide baseplate to a narrow, tall wall) lower cooling rates existed. Even more importantly, when the process is steady, they do not change depending on the layer, giving a consistent bead geometry. The difference between room temperature and 74 °C is not large enough to induce changes in the cooling rate, and bead geometry is not altered.

A.4.2 Microstructure

Micrographs are in agreement with what is already available in the literature, and no differences were seen between the control case and the specimens produced under different experimental circumstances. Therefore neither shielding conditions nor temperature affected specimen microstructure within these boundary conditions, apart from some large α_M in the base layers of specimen c (Figure A.3c). The microstructure being related to both oxygen content and cooling rate, and specimen c being optimally shielded, it is reasoned that the observed α_M is due to the difference in cooling rate experienced because of the higher part temperature. This deviation was not large enough to induce changes in the geometry, but clearly sufficient to trigger the formation of α_M. The similarity of the microstructure between the base case and oxidised sample suggests that:

- oxidation levels are not high enough to stabilise α and increase the formation of larger α colonies or lamellae; or
- the oxide was expelled due to its lower weight when the layer was molten during the deposition of a new layer.

A.5 Summary

In this appendix the effect of shielding conditions and part temperature on part geometry and microstructure was investigated. It can be concluded that they had no effect on bead geometry, and a very marginal one on the microstructure. Therefore, the empirical modelling work could be carried out without excessive attention to shielding conditions and, more importantly, saving time by not waiting until the part cooled down to room temperature.

Appendix B

Mechanical testing

In this appendix further information with regards to the mechanical testing presented in chapter 4 on page 107 is provided.

Figure B.1 shows the dimensions of the tensile test coupons extracted from the linear deposits. Figure B.2 shows the location of the tensile test coupons extracted from the control (unrolled) deposit. Figure B.3 shows the location of the tensile test coupons extracted from the deposit rolled at 50 kN. Figure B.4 shows the location of the tensile test coupons extracted from the deposit rolled at 75 kN. Figure B.5 shows the strain–stress curves for all tensile tests performed in-house at Cranfield University. Please note the tensile strength in the horizontal orientation for the deposit rolled at 50 kN was tested in an external laboratory and the related strain–stress curves are not available.

The coding was the following:

- rolling load:
  - "C" for control (unrolled)
  - "50" for 50 kN
  - "75" for 75 kN
- specimen orientation:
  - "V" for vertical

  - "H" for horizontal

- type of test:
  - "T" for tensile test
  - "F" for fatigue test (eventually not performed)
- specimen counter within the same subset of coupons

Example: C V T 2 identifies the second specimen for tensile testing, extracted from the unrolled deposit in the vertical direction. Please note that although coupons for fatigue testing were produced, for reasons beyond the author's control the test could not be carried out.

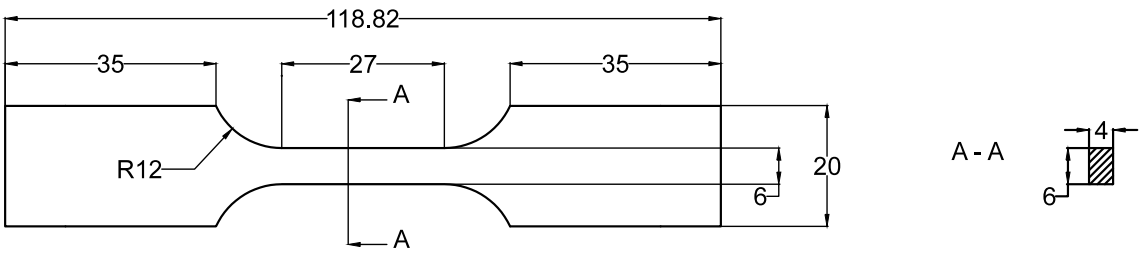

Figure B.1: Tensile test coupons (all values in mm).

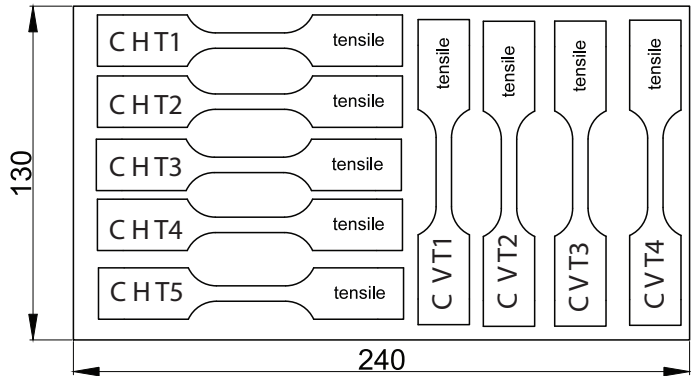

Figure B.2: Coupon locations for tensile testing of control specimen (all values in mm).

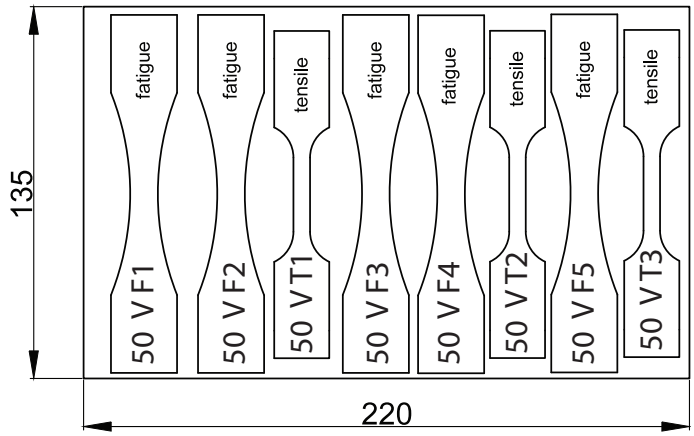

Figure B.3: Coupon locations for tensile testing of specimen rolled at 50 kN (all values in mm).

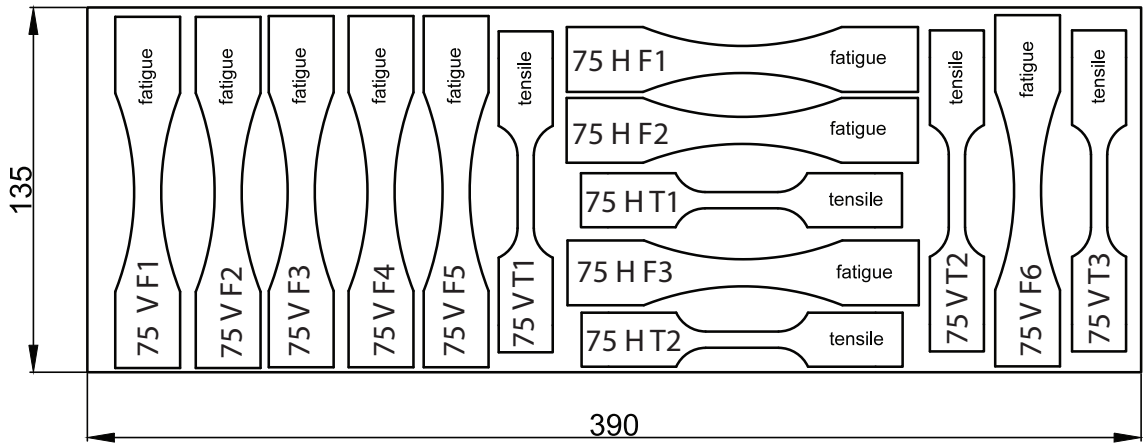

Figure B.4: Coupon locations for tensile testing of specimen rolled at 75 kN (all values in mm).

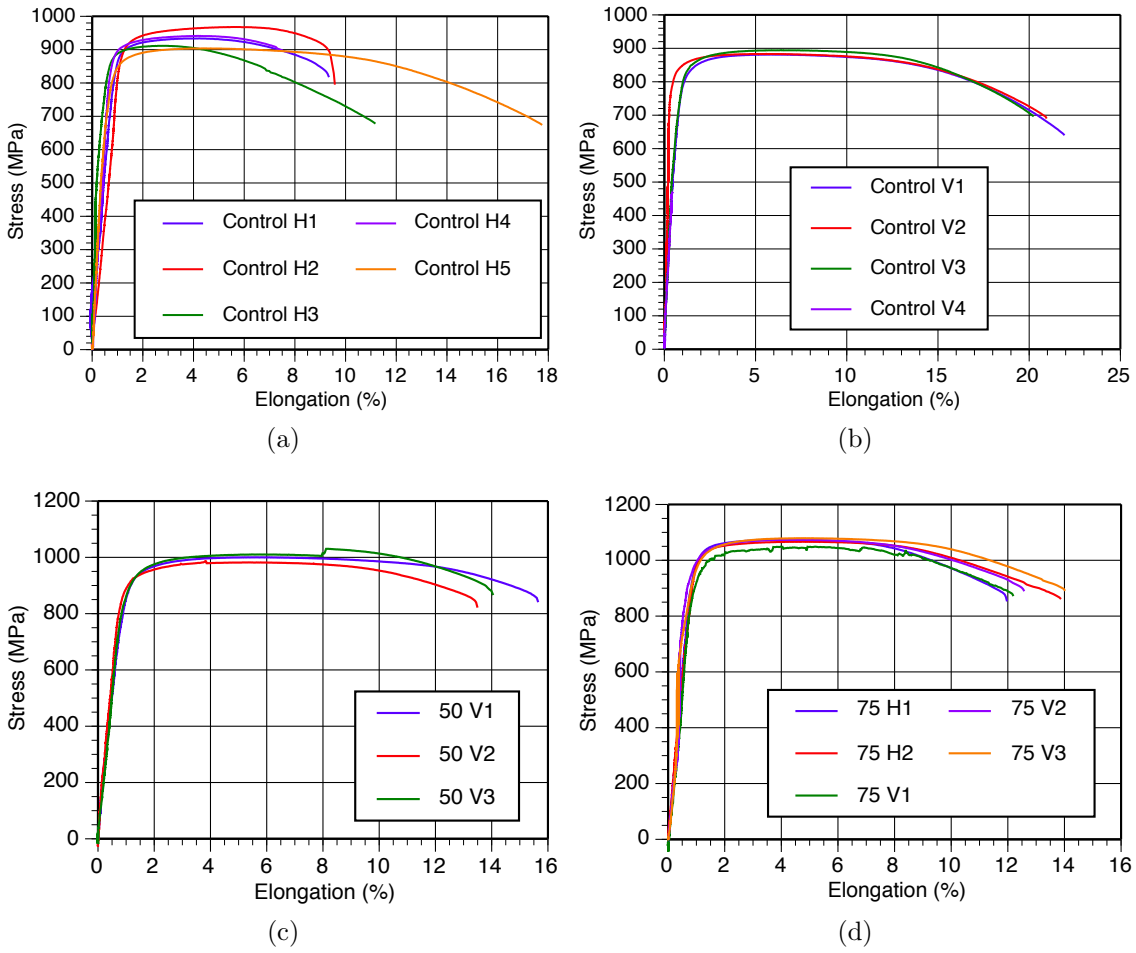

Figure B.5: Strain-stress curves from tensile tests of (a) control specimen in the horizontal direction, (b) control specimen in the vertical direction, (c) specimen rolled at 50 kN and (d) specimen rolled at 75 kN.